2020•2021
Faculteit Industriële Ingenieurswetenschappen
master in de industriële wetenschappen: elektronica-ICT

Masterthesis

Development of laser subsystem for OSCAR-QUBE sensor: testing and characterization of performance in pulsed and continuous-wave operation

PROMOTOR :
Prof. dr. ir. Ronald THOELEN

COPROMOTOR :
Prof. dr. Milos NESLADEK

BEGELEIDER :
De heer Jaroslav HRUBY

Jeffrey Gorissen

Scriptie ingediend tot het behalen van de graad van master in de industriële wetenschappen: elektronica-ICT

Gezamenlijke opleiding UHasselt en KU Leuven

2020•2021

Faculteit Industriële Ingenieurswetenschappen

master in de industriële wetenschappen: elektronica-ICT

Masterthesis

Development of laser subsystem for OSCAR-QUBE sensor: testing and characterization of performance in pulsed and continuous-wave operation

PROMOTOR :

Prof. dr. ir. Ronald THOELEN

COPROMOTOR :

Prof. dr. Milos NESLADEK

BEGELEIDER :

De heer Jaroslav HRUBY

Jeffrey Gorissen

Scriptie ingediend tot het behalen van de graad van master in de industriële wetenschappen: elektronica-ICT

UHASSELT KU LEUVEN

Acknowledgements

This master's thesis is the turning point that signals the end of my master's in Engineering Technology Electronics-ICT at the University of Hasselt and the KULeuven. This educational program has been a journey that brought me much knowledge, insights, and pleasure. While it was not always easy, this made it exciting and challenging. To be able to finish it off with an internship in the field of quantum mechanics and the space industry by participation in ESA's 'Orbit Your Thesis program!' is a true honor.

OSCAR-QUBE provided me with the chance to gain experience, expertise, and entrepreneurship that I will carry with me for the rest of my life. This holds true for both my professional and personal life. Completing this all on my own would not have been possible. Therefore, I will use this moment to acknowledge the most significant people that helped me get to this milestone.

First and foremost, I would like to thank my promotors Prof. dr. Milos NESLADEK and Prof. dr. ir. Ronald THOELEN. This is to thank them for their help, enthusiasm, and problem-solving abilities. Their feedback enabled me to improve on my work substantially. I could not have wished for better promotors. I would also like to express my sincere gratitude to my work supervisor at OSCAR, ir. Jaroslav HRUBY, for guiding me through the facilities and the equipment in the laboratory, his explanations, and supporting me during the project. His belief and support allowed me to push through.

Furthermore, I would like to thank my fellow OSCAR-QUBE team members for our cooperation within this unique project. Without this multidisciplinary team of students, we could not have completed our work. Thank you for the conversations, friendship, jokes, tips, tricks, and all the nudges in the right direction.

To finish off, I would like to thank my mother, Caroline Mulders, and my girlfriend, Laura Kuipers. My mother for always having faith in me and encouraging me to work hard and never give up. My girlfriend for providing me with unfailing support and continuous encouragement throughout my years of study and through the process of researching and writing my master's thesis. It was not always easy during the worldwide pandemic while living in different countries, yet we prevailed.

To all people not mentioned by name, ESA personnel, Space Application Services, Professors, technical staff,... Thank you very much. This would not have been possible without you!

Jeffrey Gorissen

Diepenbeek, June 7^{th}, 2021.

Contents

Acknowledgements **1**

List of tables **5**

List of Figures **7**

List of Abbreviations **11**

Abstract **13**

Abstract in Dutch **15**

1 Introduction **17**
1.1 Scope of the problem . . . 18
1.2 Aim of the project . . . 19
1.2.1 Development of a quantum magnetic field sensor . . . 19
1.2.2 Measurements of the magnetic fields on LEO . . . 19
1.3 Outline of the thesis . . . 19

2 Theoretical background **21**
2.1 Related work . . . 21
2.1.1 OSCAR-BEXUS . . . 21
2.1.2 OSCAR-QLITE . . . 21
2.2 Diamond NV center based magnetometry . . . 22
2.2.1 ODMR . . . 23
2.2.2 PDMR . . . 25
2.3 NV center readout techniques . . . 26
2.3.1 Continuous wave measurements . . . 26
2.3.2 Pulsed measurements . . . 26
2.4 Working principles for lasers . . . 29
2.4.1 Laser types . . . 29
2.4.2 Continuous wave and pulsed operation . . . 30
2.4.3 Laser driver . . . 32
2.5 PCB Design rules . . . 34
2.5.1 EMC/EMI . . . 34
2.6 Heat transfer in micro-gravity . . . 35

3 Materials and methods **37**
3.1 Hardware . . . 37
3.2 Software . . . 43
3.3 Model philosophy . . . 44
3.3.1 Test-Bench Model . . . 44
3.3.2 Proto-flight model . . . 44
3.3.3 Ground and Flight Model . . . 45

4 Experimental **47**
4.1 System overview . . . 47
4.2 Board stack . . . 48
4.3 Laser Subsystem overview . . . 49
4.4 Subsystem testing . . . 52
4.4.1 Laser driver evaluation kit . . . 52
4.4.2 Digital potentiometer . . . 53
4.4.3 PCB . . . 54
4.4.4 Driver and diode . . . 55
4.5 System testing . . . 56
4.5.1 Power consumption . . . 56
4.5.2 Laser pulsing . . . 56
4.5.3 Vacuum testing . . . 58
4.5.4 Final performance testing . . . 61

5 Results and discussion **63**
5.1 Subsystem test results . . . 63
5.1.1 Laser driver evaluation kit . . . 63
5.1.2 Digital potentiometer . . . 64
5.1.3 PCB . . . 64
5.1.4 Driver and diode . . . 66
5.2 System test results . . . 73
5.2.1 Power consumption . . . 73
5.2.2 Pulse performance . . . 74
5.2.3 Vacuum testing . . . 76
5.2.4 Final performance testing . . . 83
5.3 Issues . . . 86

6 Conclusion **87**

References **92**

A Appendix - Large Tables **93**

B Appendix - ODMR Quality **97**

C Appendix - CW and pulsed ODMR Averaging **103**

D Appendix - The OSCAR-QUBE **109**

List of Tables

3.1 SPI pin description MAX5483. 40

4.1 Main components and power consumption of the Laser Board 50

5.1 Potentiometer settings with corresponding laser output values. 68
5.2 Potentiometer settings with corresponding laser output values and the temperatures in ambient and vacuum operation. 79
5.3 ODMR Delta in mV for the corresponding potentiometer settings. 83
5.4 Notes taken during a debug session to find the cause of the irregular power output. 86

A.1 Potentiometer settings with corresponding laser output values. 94
A.2 Potentiometer settings with corresponding laser output values and the temperatures in ambient and vacuum operation. 95

List of Figures

2.1 Schematic of an NV^0 center, seen in (a) and an NV^- center in a diamond lattice representation (b). . . . 22
2.2 ODMR energy level schematic. . . . 23
2.3 NV center based magnetometry principle using PDMR. . . . 25
2.4 CW operation for ODMR. . . . 26
2.5 Pulse sequences to produce a Rabi oscillation curve. . . . 27
2.6 Ramsey magnetometry schematic with representation of free induction decay. . . . 27
2.7 Hahn-echo spin control sequence. . . . 28
2.8 Schematic representation of a laser. . . . 29
2.9 Schematic representation of three laser diode types with photodiode. . . . 30
2.10 Types of Q switching 31
2.11 Cavity dumping 31
2.12 iC-Haus iC-NZN N-type laser diode driver block diagram. . . . 32
2.13 Graphs showing the difference between ACC and APC. . . . 33
2.14 Via stitching on the left, via shielding on the right. . . . 34
2.15 Heat transfer representation. . . . 35
2.16 The effect of gravity on the boiling of water. . . . 35

3.1 NZN1D evaluation board. . . . 37
3.2 Schematic representation of a laser driver. . . . 38
3.3 Schematic representation of a laser driver. . . . 38
3.4 Thorlabs L520P50 laser diode. . . . 39
3.5 Thorlabs PM100D Power Meter & S121C Power Head 39
3.6 OSCAR-QUBE in the vacuum bell under atmospheric pressure. . . . 41
3.7 Trivac vacuum pump. . . . 41
3.8 The Analog Discovery 2 and its pinout diagram. . . . 42
3.9 Project method process 44
3.10 PFM1 or GM on the left, PFM2 or FM on the right 45

4.1 High-level subsystem overview for OSCAR-QUBE 47
4.2 The internal stack layout of the OSCAR-QUBE 48
4.3 Electronics schematics of laser subsystem 50
4.4 3D view of the PCB: Top view 51
4.5 3D view of the PCB: Bottom view 51
4.6 Preparations for testing on the iC-Haus evaluation kit. . . . 52

4.7 Preparations for testing on the MAX5483 using a 14-Pin SOIC to DIP Adapter on breadboard setup, seen on the left. . . . 53
4.8 Board to board connector as seen in Altium Designer. . . . 54
4.9 Testpoints on the laser subsystem PCB. . . . 54
4.10 Optical laser output test setup. . . . 55
4.11 5V power consumption on the OSCAR-QUBE. . . . 56
4.12 UHB showing the pulsed ODMR response. . . . 57
4.13 Wireless test setup. . . . 58
4.14 Wireshark I/O graph showing the incoming and outgoing packets. . . . 59
4.15 OSCAR-QUBE in open setup. . . . 59
4.16 OSCAR-QUBE User Home Base control dashboard. . . . 60
4.17 OSCAR-QUBE User Home Base monitor dashboard. . . . 60
4.18 Glass acting like a mirror for infrared radiation. . . . 61

5.1 Testing of the laser driver evaluation kit using an LED. . . . 63
5.2 Resistance in function of potentiometer setting 64
5.3 Laser subsystem (within red highlight) on top of Power Board 65
5.4 Voltages measured on the Laser Board 65
5.5 Screenshot verifying the communication using the analog discovery and packet sender 66
5.6 On the left laser is off, on the right laser is on. Bottom higher power setting. . . . 66
5.7 Optical laser output power in relation to the potentiometer setting. . . . 67
5.8 Temperature in relation to the potentiometer setting. . . . 67
5.9 The Analog Discovery shows a laser pulse length of 400 ns. . . . 68
5.10 Laser output power and temperature over time at R0060 69
5.11 Testing the laser output power stability at potentiometer setting R0310. . . . 70
5.12 Testing the temperature stability at potentiometer setting R0310. . . . 70
5.13 Testing the laser output power stability at potentiometer setting R0180. . . . 71
5.14 Testing the temperature stability at potentiometer setting R0180. . . . 71
5.15 Testing the laser output power stability at potentiometer setting R0060. . . . 72
5.16 Testing the temperature stability at potentiometer setting R0060. . . . 72
5.17 12 V current draw for Laser diode and System in CW operation. . . . 73
5.18 12 V power draw for Laser diode and System in CW operation. . . . 73
5.19 Oscilloscope showing the 5 μs pulse. . . . 74
5.20 Oscilloscope showing the 100 ns pulse. . . . 75
5.21 Oscilloscope showing the averaged 100 ns pulse. . . . 75
5.22 FLIR image before testing the OSCAR-QUBE in vacuum. . . . 76
5.23 OSCAR-QUBE under 68 Pa (medium) vacuum. . . . 77
5.24 Graph showing the laser temperature over a number of samples. . . . 77
5.25 Graph showing the board temperature over a number of samples. . . . 78
5.26 Thermal images of the inside captured by FLIR thermal camera. . . . 79
5.27 Thermal images of the outside captured by FLIR thermal camera. . . . 79
5.28 Thermals after 10 minutes of not being powered. . . . 80
5.29 Mean ODMR voltage in function of the laser temperature. . . . 81
5.30 5 V output and the corresponding current usage. . . . 82
5.31 12 V output and the corresponding current usage. . . . 82

5.32 Comparison of ODMR quality for potentiometer settings ranging from R0000 to R0310. . . . 83
5.33 Comparison of ODMR quality for potentiometer settings ranging from R0000 to R0200. . . . 84
5.34 Comparison of CW ODMR signals using different levels of averaging. . . . 84
5.35 Comparison of 5 μs pulsed ODMR signals using different levels of averaging. . . . 85
5.36 Comparison of 1 μs pulsed ODMR signals using different levels of averaging. . . . 85
5.37 PDMR measurement taken on the test-bench model using diamond sample #353. 86

B.1 ODMR Quality at R0310 . . . 97
B.2 ODMR Quality at R0270 . . . 98
B.3 ODMR Quality at R0200 . . . 98
B.4 ODMR Quality at R0100 . . . 99
B.5 ODMR Quality at R0075 . . . 99
B.6 ODMR Quality at R0050 . . . 100
B.7 ODMR Quality at R0025 . . . 100
B.8 ODMR Quality at R0000 . . . 101

C.1 ODMR signal without averaging at full power. . . . 103
C.2 ODMR signal with averaging of 10 sweeps at full power. . . . 104
C.3 ODMR signal with averaging of 100 sweeps at full power. . . . 104
C.4 5 μs pulse ODMR signal with no averaging at full power. . . . 105
C.5 5 μs pulse ODMR signal with averaging of 10 at full power. . . . 105
C.6 5 μs pulse ODMR signal with averaging of 100 at full power. . . . 106
C.7 5 μs pulse ODMR signal with averaging of 400 at full power. . . . 106
C.8 1 μs pulse ODMR signal with averaging of 10 at full power. . . . 107
C.9 1 μs pulse ODMR signal with averaging of 100 at full power. . . . 107
C.10 1 μs pulse ODMR signal with averaging of 400 at full power. . . . 108

D.1 OSCAR-QUBE GM and FM in the lab at IMO-IMOMEC with dimmed lighting. . 109
D.2 OSCAR-QUBE in the lab at IMO-IMOMEC after winning design was lasered onto the side panel. . . . 110
D.3 OSCAR-QUBE Art design close-up. . . . 110
D.4 OSCAR-QUBE at Space Application Services in the ICE CUBE Facility with tray opened. . . . 111
D.5 OSCAR-QUBE at Space Application Services in the ICE CUBE Facility with tray closed. . . . 111
D.6 Close-up of the powered OSCAR-QUBE GM at Space Application Services in the ICE CUBE Facility. . . . 112
D.7 OSCAR-QUBE GM and FM at Space Application Services in the ICE CUBE Facility. . . . 112

List of Abbreviations

AC	Alternating Current
ACC	Automatic Current Control
ADC	Analog Digital Converter
APC	Automatic Power Control
BEXUS	Balloon Experiments for University Students
COD	Critical Optical Destruction
COTS	Commercial Off The Shelf
CW	Continuous Wave
DC	Direct Current
DLR	German research center for Aeronautics and Space
EEPROM	Electrically Erasable Programmable Read-Only Memory
EMC	Electromagnetic Compatibility
EMI	Electromagnetic Interference
ESA	European Space Agency
FM	Flight Model
FPGA	Field Programmable Gate Array
GM	Ground Model
GPIO	General Purpose Input Output
ISS	International Space Station
LASER	Light Amplification by Stimulated Emission of Radiation
LD	Laser Diode
LEO	Low Earth Orbit
MCU	Micro-controller Unit
MW	Microwave
NV	Nitrogen-Vacancy
ODMR	Optical Detection of Magnetic Resonance
OSCAR	Optical Sensors based on CARbon materials
PCB	Printed Circuit Board
PD	Photo Diode
PDMR	Photoelectrical Detection of Magnetic Resonance
PFM	Proto-Flight Model
QLITE	Quantum Lightweight ITEration
REXUS	Rocket Experiments for University Students
RF	Radio Frequency
SNSA	Swedish National Space Agency
SPI	Serial Peripheral Interface
STEM	Science, Technology, Engineering and Mathematics
TBM	Test-Bench Model
TCP	Trans-mission Control Protocol
UDP	User Datagram Protocol
USB	Universal Serial Bus

Abstract

Since the early 20^{th} century, physicists have been interested in the real-world applications of quantum technologies such as quantum sensing. The Nitrogen-Vacancy (NV) centers in diamond are promising opto-magnetic probes acting as solid-state qubits while operating at room temperatures. Green Laser light excites the NV centers, leading to the release of photons that enable the electron spin-state readout. Magnetic fields can alter the spin-state resulting in changes in photoluminescent intensity. This thesis focuses on designing, developing, testing, and characterizing the laser subsystem for an NV diamond-based magnetometer.

The approach is to design a PCB integrated laser subsystem that enables both the Optical and Photoelectric Detection of Magnetic Resonance (ODMR/PDMR) readout methods. Output power stability and thermal stability are crucial to use these techniques for measurements in both continuous wave and pulsed operation modes. The 520 nm laser offers a power output ranging from 0 to 50 mW, pulse widths down to 10 ns, and 1.5 ns rise and fall times. The standard deviation on the output power is less than 0.5%, implying the system is stable. Operational temperatures at maximum power do not exceed 43 °C and 66 °C for ambient and vacuum environments, respectively.

This work is part of the student project OSCAR-QUBE, within the framework of the "Orbit Your Thesis!" program organized by the European Space Agency and will fly onboard the international space station in 2021-2022.

Abstract in Dutch

Vanaf de 20^{ste} eeuw zijn fysici geïnteresseerd in de toepassingen van kwantum technologieën zoals kwantumdetectie. De Nitrogen-Vacancy (NV) centra in diamanten zijn veelbelovende opto-magnetische sondes die zich gedragen als op kamertemperatuur werkende solid-state qubits. Groen laser licht kan de NV centra exciteren, dit leidt tot het vrijkomen van fotonen die het mogelijk maken om de elektron spin-state te lezen. Magnetische velden kunnen de spin-state wijzigen met intensiteitvariaties van de fotoluminescentie tot gevolg. Deze thesis focust zich op het ontwerpen, ontwikkelen, testen, en karakteriseren van het laser subsysteem voor een NV diamantgebaseerde magnetometer.

De aanpak is om een PCB-geïntegreerd lasersubsysteem te creëren dat zowel de Optische als de Foto-elektrische Detectie van Magnetische Resonantie (ODMR/PDMR) uitleesmethoden faciliteert. De stabiliteit van het uitgangsvermogen en de temperatuur zijn cruciaal om deze technieken te gebruiken voor de continu en pulserende modus. De 520 nm laser biedt een vermogen van 0 tot 50 mW, kleinste puls breedte van 10 ns, 1.5 ns stijg- en zaktijden. De standaard afwijking op het uitgangsvermogen bedraagt minder dan 0.5%, duidend op een stabiel systeem. Operationele temperaturen blijven onder 43 °C en 66 °C, voor kamertemperaturen en vacuüm respectievelijk.

Dit werk is deel van het studentenproject OSCAR-QUBE binnen het “Orbit Your Thesis!” programma van de Europese Ruimtevaartorganisatie en zal meevliegen op het Internationaal Ruimtestation in 2021-2022.

Chapter 1

Introduction

Finding magnetometry applications is easy. Geophysical studies, avionics, archaeology, healthcare, scientific research, and mineral and oil exploration all use magnetometry. Magnetometers themselves have been around for ages. The compass, for example, is a magnetometer that measures and displays the direction of the strongest magnetic field in the vicinity. Most often, the strongest field present is the magnetic field of the Earth. The OSCAR-QUBE sensor is a quantum magnetometer based on diamond. Much like a compass, the OSCAR-QUBE is a sensor that can detect magnetic fields. Additionally, this quantum magnetometer can detect the direction, strength, and changes of that magnetic field in high resolution and high dynamic range.

The developmental basis of the device lies with the experience gained during the OSCAR and OSCAR-QLITE projects. These editions have been tested onboard stratospheric balloon flights in the REXUS/BEXUS (Rocket / Balloon Experiments for University Students) program framework. In the first iteration of the OSCAR project, development started on the first portable diamond magnetometer working on the ODMR principle, fulfilling the aim of testing the viability of the diamond technology in near-space conditions. This, together with new fundamental discoveries, paved the way towards a second iteration.

The OSCAR-QLITE project aimed to develop the first miniaturized and fully integrated Photoelectric Detection of Magnetic Resonance (PDMR) based prototype, which operates outside laboratory conditions. The project fulfilled its technical goals. However, due to the complexity of the task, the team ran out of time and could not fully characterize the device's performance from a scientific point of view.

This is where the OSCAR-QUBE project comes in. In March 2020, the OSCAR-QUBE team emerged victorious from the 'Orbit Your Thesis!' selection procedure. This brought the opportunity to bring the OSCAR-QUBE aboard the ISS. With the thoroughly tested OSCAR-QUBE, the theoretical limits of NV magnetometry, tuned and tested for operation in the International Space Station (ISS) and the ICE Cubes facility environment, can be explored.

A laser is needed to excite the NV centers in order to measure the magnetic fields by detecting the changes in photoluminescent intensity. The photoluminescent intensity depends on the amount of energy the laser provides to the NV centers. This makes the output power stability inherently important to obtain accurate measurements. For this the laser subsystem was designed, developed, and tested.

1.1 Scope of the problem

The field of quantum sensing is a novel emerging field, which brings improved performance and function compared to classical sensing methods. The OSCAR-QUBE project focuses on the development of next-generation quantum magnetic field sensors based on diamonds. The resulting device will be flown aboard the ISS for ten months to measure the magnetic field in Low Earth Orbit (LEO). The European Space Agency (ESA) tasked a committee to select a team of students within the 'Orbit Your Thesis!' program. They selected team OSCAR-QUBE, and the launch of the OSCAR-QUBE to orbit will be in August 2021. The project generates a stimulating and challenging environment for students to experience quantum sensor development and space sector requirements. Engineering and physics students from the University of Hasselt participate in the team to work in an interdisciplinary environment that inspires personal growth in technical skills and soft skills.

This thesis aims to develop the laser subsystem for excitation of nitrogen-vacancy (NV) centers in diamond for the OSCAR-QUBE sensor. The stable green laser beam focused in between the electrodes is essential for the diamond quantum sensor operation. The laser will have two operation modes, continuous wave (CW) and pulsed operation. The CW method serves as a baseline operation, whereas the pulsed method unlocks the true quantum potential of the device. Such as selective AC (Alternating Current) or DC (Direct current) magnetic field detection or locking on the magnetic field of a specific frequency. Development and testing of the system first happened stand-alone on a dedicated test bench. The second step, integration into the OSCAR-QUBE sensor flight model, happened after verification, optimization, and testing.

Within this scope, success is achieving multiple milestones to fulfill the project's entire scope. A list of key milestones is listed below:

- To deepen the understanding of laser operation, laser driving and requirements of pulsed and CW operation
- To design, assemble and test the 'test bench' model laser subsystem
- Verification of the functional and performance requirements on diamond sample in a 'test bench' conditions
- Preparations of the laser subsystem for integration into the flight model
- Verification of all the laser subsystem requirements and operation modes after integration

Additionally there are some benefits linked to the participation on this specific project:

- Interdisciplinary thesis within quantum research and the space sector
- Challenging topic with enough time dedication
- The timeline of the thesis is in perfect sync with the OSCAR-QUBE project deliverables
- Interaction with ESA experts and participation at reviews and workshops
- First UHasselt experiment to be onboard ISS
- Project is focused on STEM with strong outreach potential for the university
- Create a representative portfolio

1.2 Aim of the project

- Selection and testing of components required for the laser subsystem.
- Designing the electronic schematics and PCB and the assembly of the laser subsystem.
- Verification of the functionality and performance of the laser subsystem.
- Functional and performance testing of the laser subsystem in function of the entire system.

1.2.1 Development of a quantum magnetic field sensor

In the previous projects, OSCAR has successfully developed portable magnetometers that were flying on the OSCAR-BEXUS (2015) and the OSCAR-QLITE (2018) missions. This next step aims to fully characterize the device performance and the device stability in long-term space missions. For this purpose, the ISS and ICE Cube facility are an excellent choice since they provide exposure to the actual space environment and the proper conditions to detect elements of interest while taking out the risks and complexity of a dedicated CubeSat mission. OSCAR-QLITE developed a miniaturized state-of-the-art diamond quantum sensor.

Based on the existing designs and chosen components, further development will occur. The main focus will be on reaching the performance and demonstrating the promised theoretical limits of sensitivity, bandwidth, dynamic range, linearity, noise floor, power consumption, volume and mass, temperature independence, and stability over time. By achieving this objective, it will kickstart a new era of space magnetometry. It will facilitate magnetometry to overcome limitations set by conventional measuring technologies such as fluxgates and search coils. The OSCAR project can become the steppingstone for quantum sensing technologies on future space exploration missions.

1.2.2 Measurements of the magnetic fields on LEO

By performing magnetic field measurements using NV-based magnetometry on Low Earth Orbit (LEO), satellites, and beyond, new doors to better understand the processes causing the effects in Earth's magnetosphere are opened. This will be possible thanks to the extreme sensitivity and wide bandwidth of the OSCAR-QUBE and its fast response time, and the inherently vectorial nature of the defect. The net magnetic field that can be measured is a complex superposition of components from different sources set apart by different spatial and temporal scales. Various near-Earth space magnetometry concepts have been developed in the past decade to overcome this limitation and improve our ability to recover the field of internal origin.

1.3 Outline of the thesis

A chapter on the Theoretical Background follows this introductory chapter. The related work and science behind the inner working are condensed to serve as a foundation for the thesis. Then the Materials and Methods chapter outlines the hardware, software, and model philosophy. The Experimental chapter puts the focus on the actual work done in function of this thesis. After this, the outcome can be seen in the Results and discussion, followed by the Conclusion.

Chapter 2

Theoretical background

OSCAR-QUBE is an interdisciplinary team of students based at Hasselt University and IMO-IMOMEC. The project is composed of students from different faculties with a mission to bring quantum sensing technology out of the lab and into orbit. The theory backing this thesis starts with Nitrogen-Vacancy-centers (NV center). Therefore, diamond-based magnetometry and the corresponding measurement techniques are of paramount importance for this thesis. It is vital to know the elemental working principles around the system mentioned in Section 1.1, in order to start working on a system that is based upon this

2.1 Related work

2.1.1 OSCAR-BEXUS

The first OSCAR experiment aimed to explore using a novel generation of carbon-based optical sensors/solar cells for aerospace applications. This was done through onsite testing during a stratospheric balloon flight (BEXUS 23) and by complementary offsite testing before and after the flight to observe and understand the impact of the coarse environment. The project proposal was submitted in the context of the REXUS/BEXUS (Rocket / Balloon Experiments for University Students) program, organized by the Swedish National Space Agency (SNSA), the German research center for aeronautics and space (DLR), and ESA. By using carbon-based solar cells with a low mass, a very high power-to-mass ratio was achieved. This made these devices excellent candidates for aerospace applications. The objectives for this first OSCAR project included the development of a method to study the characteristics of the solar cells and the testing of the optical magnetometer prototype in the harsh stratospheric conditions [1].

2.1.2 OSCAR-QLITE

In the second half of 2017, the project proposal for OSCAR-QLITE (Quantum Lightweight ITEration) was submitted. Like OSCAR, OSCAR-QLITE got selected to participate in the BEXUS section of the REXUS/BEXUS program. This time the objective was to test a new electrical detection method for magnetometry. During the OSCAR BEXUS 25 flight, OSCAR-QLITE the miniaturized magnetic field sensor testing and found to be suitable for use in the aerospace industry. With this, OSCAR-QLITE provided the stepping stone for continued deployment of this diamond-based technology for long-term application in space [2].

2.2 Diamond NV center based magnetometry

NV centers are the core mechanics that enable diamond-based magnetometry. The isolated electronic spin found in the NV centers leads to new opportunities to detect magnetic fields. These NV centers are defects in the diamond crystal lattice structure. The defects are made up of a nitrogen atom (N) coupled to a vacancy (V). These defects can be found along with all four directions of the crystalline lattice structure found in diamonds. This enables measurements to be taken in three dimensions.

To this date, two unique versions of this diamond crystal lattice structure irregularity have been described. A neutral state NV center (NV^0) and a negatively charged state NV center (NV^-). The properties of these two versions differ from each other significantly. For magnetometry purposes, the NV^0 does not aid in the detection of a magnetic field. Thanks to its specific spin properties, the NV^- allows for the initialization and readout of the spin state [3].

In order to fabricate the NV centers, type 1b diamonds [4] are needed. These diamonds are first irradiated, after which they are annealed. These nitrogen impurities found within these types of diamond reach levels up to 0.3%. The NV centers are fabricated by irradiating the diamond with electrons. The next step is to perform the annealing. This is done at temperatures ranging from 800°C to 2000°C, while pressures range from vacuum to 8 GPa. These extreme environments are needed in order to facilitate the arrangement of nitrogen impurities together with vacancies. According to [5], NV centers have the habit to attract and bond with an electron. This can be seen in Figure 2.1. The result is the creation of an NV^- center [5, 6, 7].

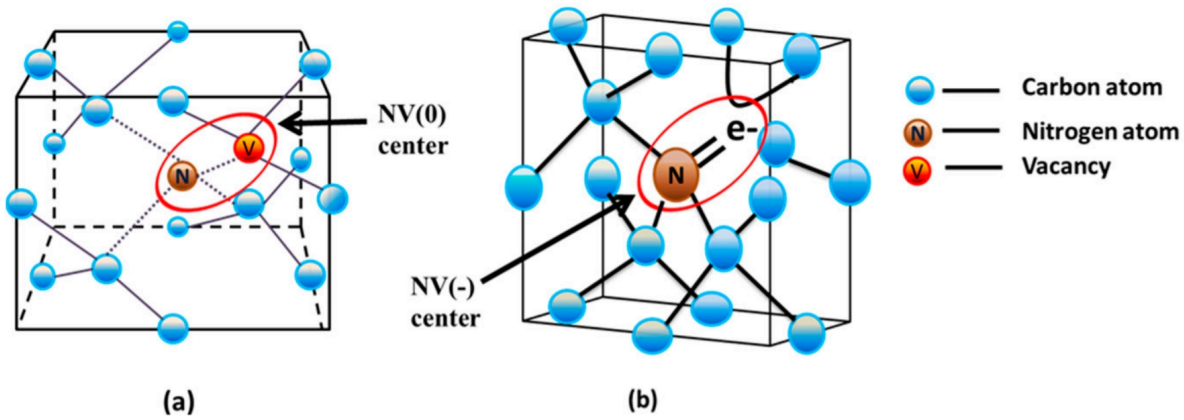

Figure 2.1: Schematic of an NV^0 center, seen in (a) and an NV^- center in a diamond lattice representation (b). Source: [5]

2.2.1 ODMR

The electron of an NV center exists in a spin-triplet ground state. As the naming suggests, it features three magnetic spin states, ±1 and 0. An electron residing in the ground state ($^3A_2$) can be excited to an excitation state (^3E) by a green photon. When the electron degrades back to the ground state, this coincides with the release of a red photon. Under stable conditions, this emission of red photons is constant and without photobleaching. By application of microwave (MW) frequencies that are correlated to the resonance frequency (f_0) of the NV centers, the electron with positive-negative (m_s=±1) spin can perform a dark transition. This dark transition is possible since the MW provides enough energy to let the electron transition through the metastable state (^1A). This process can be seen in Figure 2.2. The frequency in normal conditions is around 2.87 GHz. When this intensity is mapped in function of frequency, an intensity drop can be seen at the resonant frequency [3, 8].

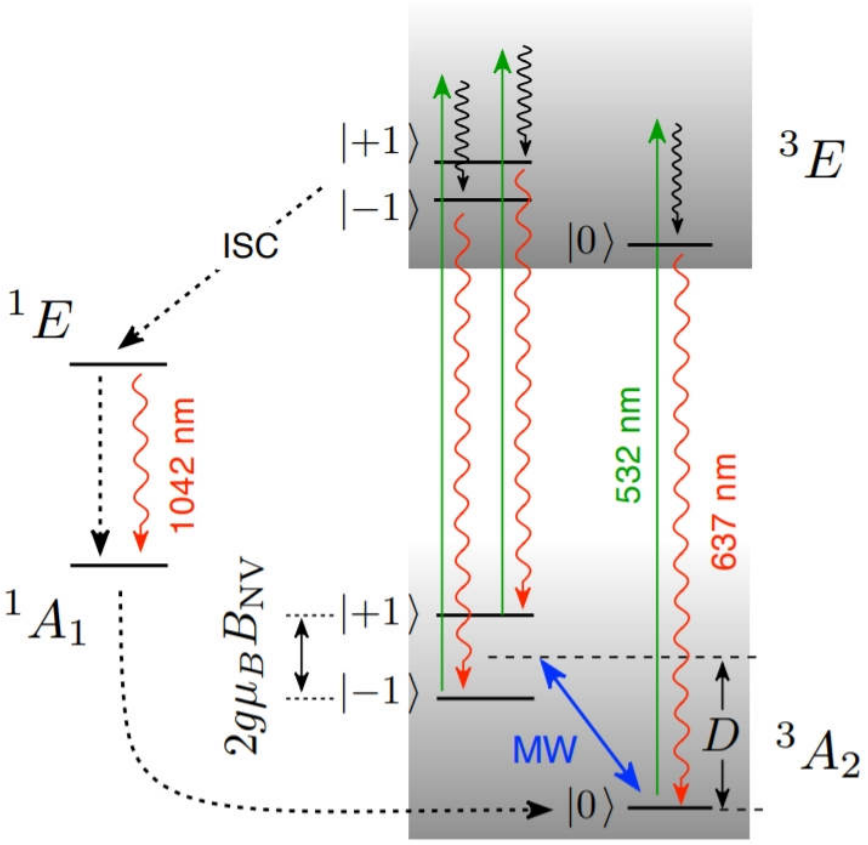

Figure 2.2: ODMR energy level schematic. Source: [3]

These NV centers are, in effect, solid-state quantum phenomena that can function at room temperature. Thanks to their high spin coherence, they facilitate magnetic field sensitivities going down to 100 fT$\sqrt{\text{Hz}}$ [3, 8]. The limit on this has been predicted to be around 1 fT$\sqrt{\text{Hz}}$ according to [8]. The optical readout techniques for NV spin make use of the red photoluminescence light being released from the NV^- during their excitation. A green laser typically performs this excitation. The intensity of the red photon release provides details on the spin states of the electron triplet ground state within the NV^- [9].

The method based on the photoelectrical readout of the emitted photons is called Optical Detection of Magnetic Resonance (ODMR). [3, 8, 10]. When a static external magnetic field (B_{EXT}) is applied, the Zeeman effect can be observed as the m_s=+-1 is split. This quantum effect is reflected in the observed spectrum [11]. The perturbation (H'_Z) due to the magnetic field can be seen as follows in Equation 2.1, where μ_l stands for the magnetic dipole moment associated with orbital motion, and μ_s for the magnetic dipole moment associated with electron spin.

$$H'_Z = -(\mu_l + \mu_s) * B_{EXT} \text{ [11]} \tag{2.1}$$

Zeeman splitting causes the separation of components, and intensity drops can now be seen at two different frequencies. These drops are symmetric along f_0 and Δf corresponding with the applied magnetic field. This effect can also be seen in Figure 2.3. The strength of the magnetic field correlates directly to the distance between the dips as described by Equation 2.2, where g is the Landé g-factor and μ_B is the Bohr magneton [11]. This is refactored by [3] to Equation 2.3 where Δv equals the distance between the dips, h is Planck's constant, and B_{NV} is the magnetic field projection along the NV axis.

$$E^1_Z = \mu_B * g_J * B_{EXT} * m_j \text{ [11]} \tag{2.2}$$

$$\Delta v = 2 * g * \mu_B * B_{NV}/h \text{ [11]} \tag{2.3}$$

Advancements were made in the field of pulsed ODMR techniques since ODMR was first described in 1997 [12]. Rabi, Ramsey, and Hahn-Echo pulse sequences have since been used to increase the contrast obtained from the measurements. This is constrained as the spin detection sensitivity depends on photon collection performance [13]. The photon flux saturation is dependent on the short lifetime of NV^- excited state, with typical observable values of 1% for the efficiency of photon collection [14, 15].

Within the field of Quantum sensing, a distinction needs to be made between DC and AC sensing protocols. DC sensing protocols are focused on static magnetic fields. On the other hand, AC sensing protocols focus on time-varying magnetic fields [16].

2.2.2 PDMR

After ODMR, another method based on photoelectric readout was developed. This Photoelectric Detection of Magnetic Resonance (PDMR) was first described in 2015 [17]. With PDMR, electrons are excited to the conduction band by two (green) photon excitation and detected as a photocurrent. This working principle can be seen in Figure 2.3. Compared to ODMR, the main advantage of the PDMR technique is that the detection is not based on the detection of actual photons that get emitted from the NV centers.

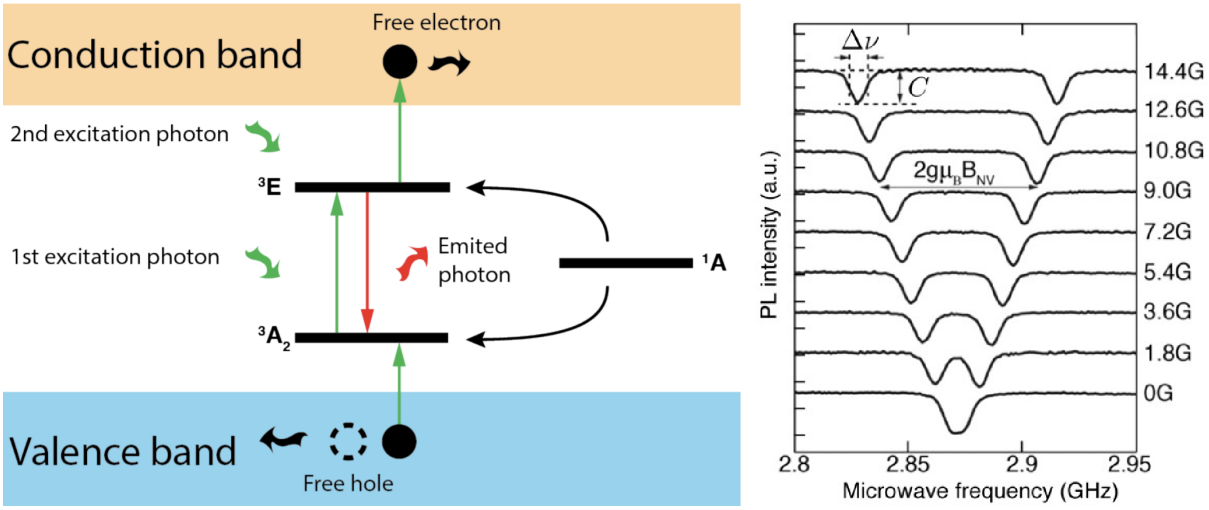

Figure 2.3: NV center based magnetometry principle using PDMR. Source: Adapted from [3].

The main parameters to describe the performance of a PDMR system are the detection rate, PDMR linewidth, and the PDMR contrast. This process of collecting photons is limited in its efficiency due to photons traveling in all directions [15, 17]. However, with PDMR, the saturation is defined by the time it takes for recombination to occur in the charge carrier. Leading to serious enhancements in the detection rates for PDMR based measurement techniques [13]. The improvement of the detection rates adds up to $\approx 2.5x10^2$ times that of ODMR [13]. For the linewidth, PDMR is dependent on the spin coherence properties of the diamond sample itself [18]. Lastly, the contrast, expressed in percentage, can be described as the magnitude reduction of the photoluminescence (ODMR) or photocurrent (PDMR) at f_0 [13, 17].

2.3 NV center readout techniques

Two main methods can be pursued to readout the NV centers: continuous wave (CW) and pulsed techniques. The CW method utilizes a continuous excitation of the NV centers to perform measurements. Here a continuous laser and MW output is used. The pulsed method relies on a range of pulse sequencing techniques to increase the contrast in the measurements [13, 15, 17].

2.3.1 Continuous wave measurements

A laser will produce a constant beam illuminating the diamond sample and the NV centers with this first mode. This can be seen in Figure 2.4. At the same time, a MW sweep is performed, and an ADC (Analog Digital Converter) can read the amplified signal. The configuration of the pulsed operation is be based on the peaks that can be seen in the CW operation [13, 17, 16, 19].

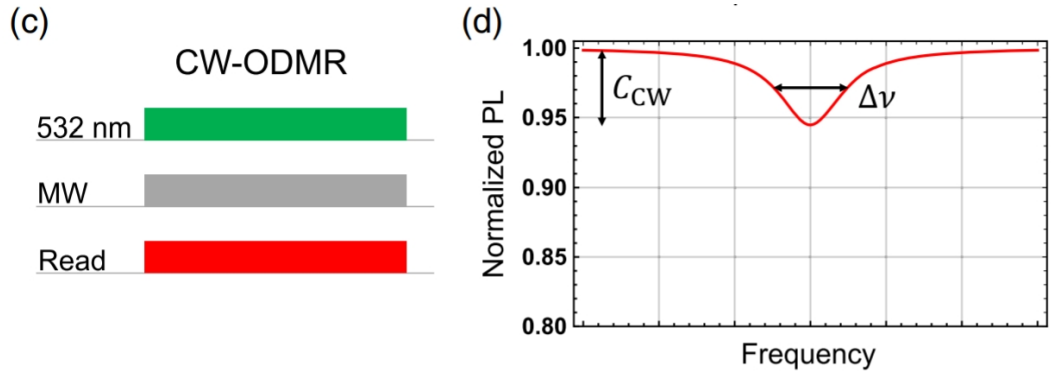

Figure 2.4: CW operation for ODMR. Source: [16]

2.3.2 Pulsed measurements

In this second active measurement mode, both the laser and the MW generator are pulsed in specific pulse sequences. An ADC can then read the amplified signals. The pulse sequences for the laser and MW can range from elementary frequency series to sophisticated pulsing schemes. Two promising schemes are the Ramsey and Hahn echo pulse schemes. The implementation of pulsed measurements brings frequency locking, better sensitivity, and noise decoupling to the table. Having both CW and pulsed operation modes working together enables better performance than either method could achieve on its own [13, 17, 16, 19].

Rabi oscillation curve

The Rabi oscillation curve is needed to determine the time it takes for the spin state to transition from $m_s = 0$ (ground state) to $m_s = \pm 1$ of the NV centers. This duration is called the τ pulse time and is required in all pulse sequences as this defines the pulse durations [13, 17, 20].

To produce a Rabi oscillation curve, one needs to look at the correlation between the photon emissions over time due to variations in the length of the MW pulse. To do this, the NV center spin state is set to zero employing a laser pulse, the initialization pulse. After this, the spin state is excited about a MW pulse with a frequency equal to f_0. The following laser pulse acts as a readout pulse that compares the photon counts that got collected during the integration time with those of the initial pulse. This can be seen in Figure 2.5. The result is the contrast, which can then be used to measure the spin state decay for the distinct MW pulse width [13, 17, 20].

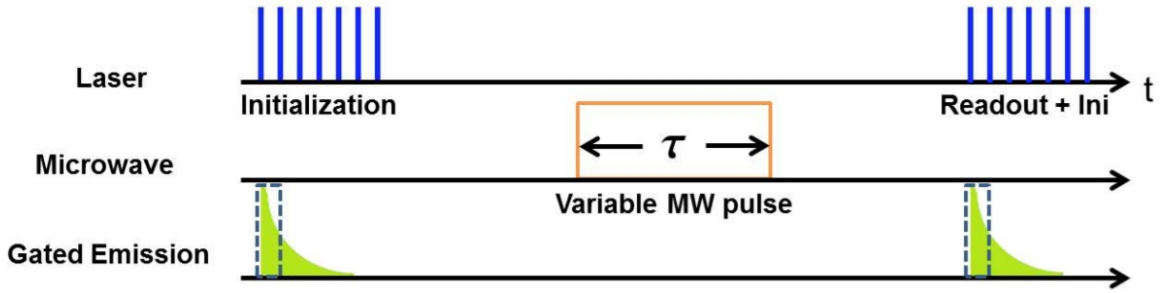

Figure 2.5: Pulse sequences for Rabi oscillation measurements. Source: [20]

Ramsey sequence

Further optimizations can be achieved using the Ramsey sequence. The sequence, seen in Figure 2.6, consists of an initializing green laser pulse, followed by two $\pi/2$ MW pulses with a free precession time τ to divide them. This is finished up with a green readout pulse. During this last readout pulse, the red photon emissions are measured.

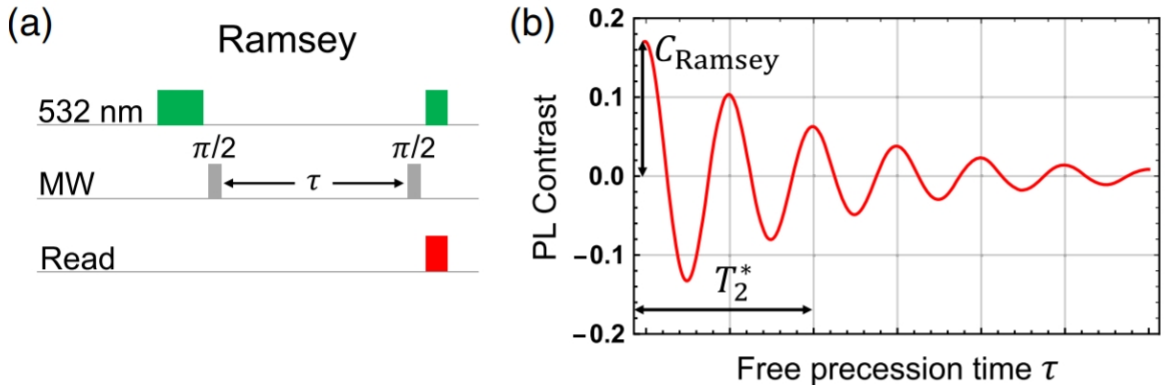

Figure 2.6: Ramsey magnetometry schematic with representation of free induction decay. Source: [16]

Within the Ramsey pulse scheme, the electron spin acquires a phase concerning its initial state |0> [16]. This phase is linearly proportional to the magnetic field and can be used to measure DC fields. The magnetic field can be calculated using Equation 2.4 as described in [16]. Here, ϕ is the acquired phase during the precession time τ, γ_{NV} is the gyromagnetic ratio of the NV center, and B is the magnetic field.

$$\Phi = \gamma_{NV} * B_\tau \text{ [16]} \tag{2.4}$$

Hahn-Echo

The Hahn echo pulse scheme features an extra τ pulse halfway through the free precession time compared to Ramsey. This facilitated the readout of AC magnetic fields. This additional τ pulse, as seen in Figure 2.7 is responsible for what is called a dynamical decoupling of the spin from its surroundings [13, 17, 16, 19].

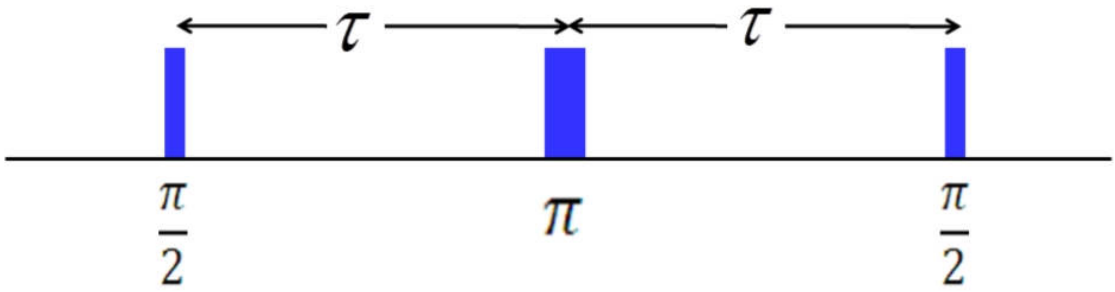

Figure 2.7: Source: [19]

The DC magnetic field sources collect a phase during the first τ precession. The second *tau* counteracts this. As a result, the dephasing occurring due to the random noise emerging from the lattice environment is reduced, and the spin coherence time increased. This leads to increases in the sensitivity of the measurements. By changing the duration of the precession time, phase-sensitive locking-type measurements of AC fields can be performed [13, 17, 16, 19].

The magnitude of the magnetic field at this AC frequency can be determined as it can be with the Ramsey sequence. This allows for another increase in the sensitivity for measuring AC fields. However, it results in a decrease in sensitivity in DC fields. The locking of the frequencies can aid in the differentiation of signals with frequencies akin to each other. This results in the possibility to decouple them [13, 17, 16, 19].

2.4 Working principles for lasers

The laser subsystem contains several key components that need to be comprehended to test and characterize the performance for both continuous and pulsed operation of the system. A laser is a light source capable of producing a narrow coherent beam of light. Therefore, the light from a laser is monochromatic and directional, unlike most other light sources, which emit light in many directions in a broad spectrum of wavelengths and phases. Laser light also always provides a light beam that does not or hardly converges or diverges. The word laser is originally an abbreviation for Light Amplification by Stimulated Emission of Radiation [21].

A schematic representation of a gas-based laser can be seen in Figure 2.8. The electricity from a power source allows for the excitation of atoms in the laser medium (Gas or semiconductor material). The excitation of these atoms allows them to jump to a higher energy level. When the electrons revert back to their ground state, a photon is emitted. This stimulated emission of photons is then allowed to reflect between two mirrors placed in parallel. The rear mirror is 100% reflective, while the output mirror is only partially reflective. This amounts to the amplification of the photons due to them traveling back and forward multiple times. Photons that are unable to reflect correctly due to low angles will eventually hit the atoms again. This leads to two coherent photons being emitted, referred to as stimulated emission. The partial reflectiveness of the output mirror allows photons to pass when the amplification has reached sufficient power levels. This is the effect perceived as the actual laser point being projected by the laser [21].

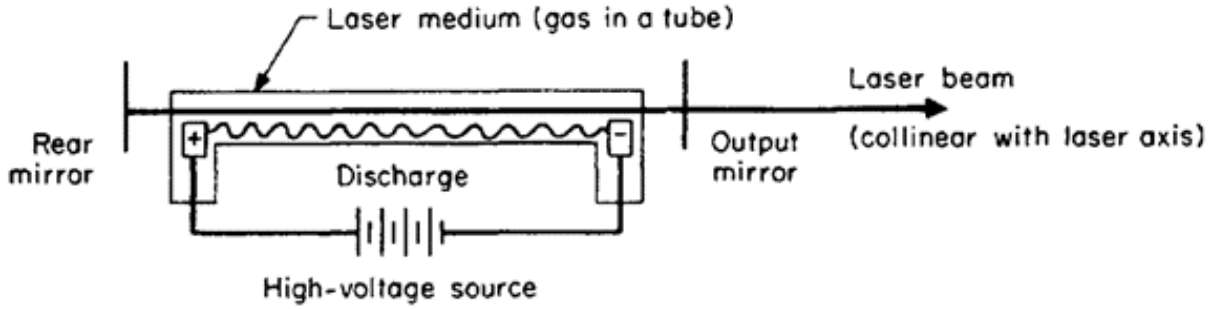

Figure 2.8: Schematic representation of a laser. Source: [21]

2.4.1 Laser types

The goal here is not to describe each and every one of the laser types available on the world. Lasers can be categorized by a multitude of options [21]:

- Medium: Gas, solid state, Dye, Semiconductor, fiber, Photonic crystal,...
- Output: Continous wave or pulsed
- Wavelenght: Infrared, Ultraviolet, visible light,...
- Power: From milliwatts to petawatts [22].
- ...

The focus, in this case, will be on laser diodes. For this purpose, there are four different types of laser diode (LD) configuration—namely, P-type, N-type, M-type, and Z-type. The driver circuit needs to be optimized based upon the chosen LD. For the P-type LD, a positive supply voltage is needed in the driver circuit. The N-type LD require a negative supply voltage to operate. M-type LD are more challenging to facilitate, as they need to have a reference that is generated separately to provide for the internal photodiode's feedback. The P-, N-, and M-type lasers all have a built-in photodiode (PD), as seen in Figure 2.9. Lastly, the Z-type LDs are much more straightforward as they lack an internal PD.

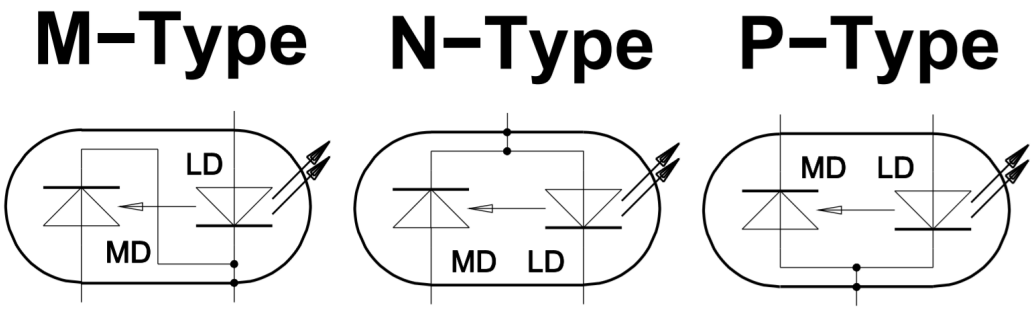

Figure 2.9: Schematic representation of three laser diode types with photodiode. Source: [23].

2.4.2 Continuous wave and pulsed operation

As discussed in Section 2.4.1, lasers can be characterized by their type of output. More specifically, this can be brought down to the duration of the laser emission. This can be either a continuous wave operation or a pulsed operation.

CW laser operation happens when the LD delivers a stable beam power. Depending on the application, and the type of laser, the power level can be adjusted during operations. This is not the case for Helium-Neon lasers. The power these lasers output is fixed in their design [21].

For the pulsed operations, there are a certain amount of distinguishments to be made. There are four techniques commonly used to produce pulsing in lasers. The first three of them, Q switching (Seen in Figure 2.10), cavity dumping, and mode-locking work due to their light interaction within the laser cavity. They build up the energy to produce a short high peak power pulse compared to the regular laser emission [21]. This does lead to efficiency losses. The last option is to switch the beam off and on. This can either be done electrically or by using some shutter. Current LD drivers [24] offer on-chip pulsed operation making the implementation of pulsed operation more straightforward than before.

The basic concept of cavity dumping is dumping the energy out of the laser cavity by a means such as popping an intracavity deflecting mirror into the beam. This can be seen in Figure 2.11. Actual cavity dumpers are more complex systems that rely on acousto-optic deflectors or electro-optic modulators.

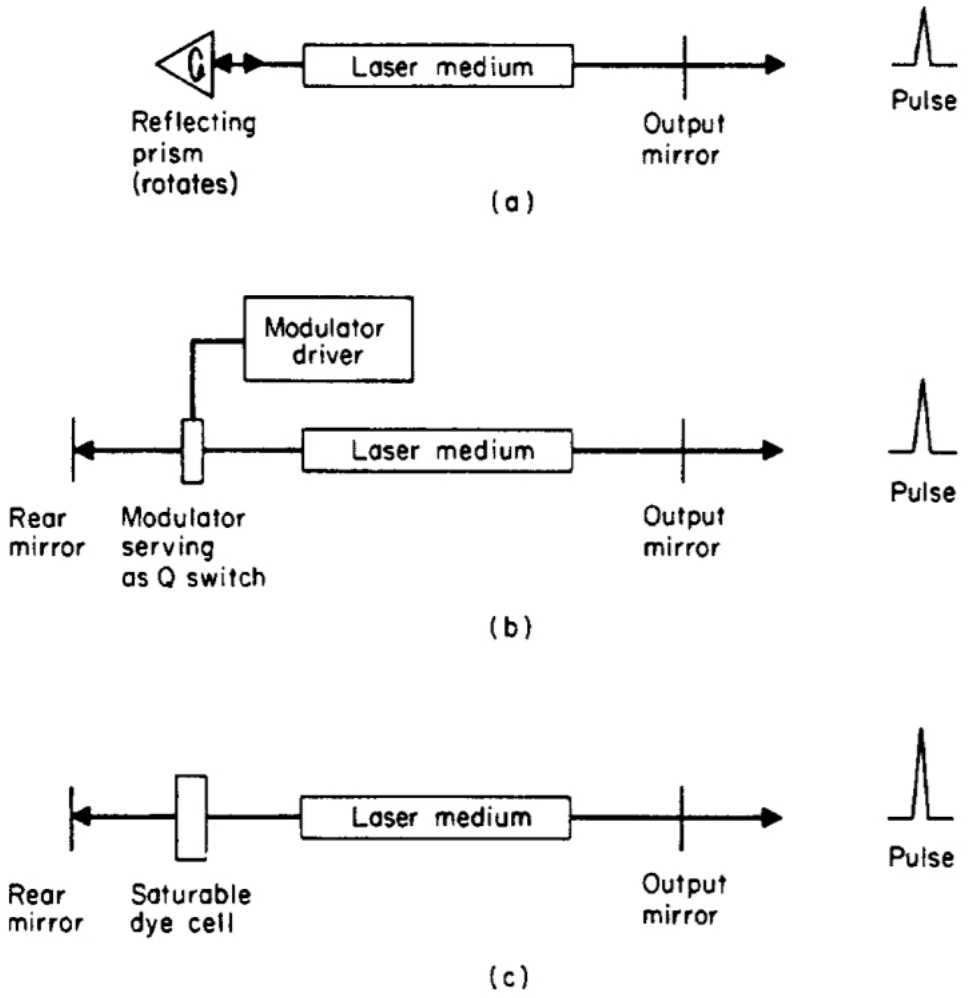

Figure 2.10: Various types of Q switching: (a) uses a rotating mirror or prism, (b) uses of an active modulator, and (c) utilizes the passive properties of a saturable dye cell. Source: [21]

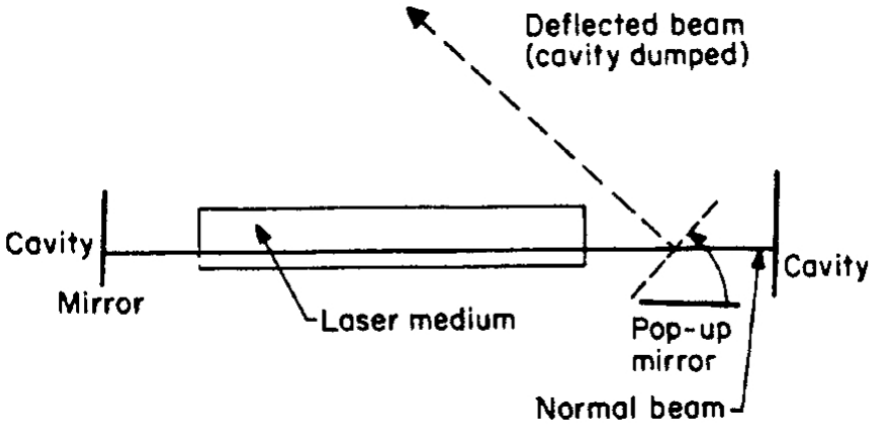

Figure 2.11: cavity dumping. Source: [21]

2.4.3 Laser driver

A laser driver in its most elementary form is a constant current source. Ideally, this current source can accurately provide the LD with a linear current without noise. The current needed to operate depends on the application. Typical laser pointers are limited to a maximum optical power output of 1 mW [25], while scientific, industrial, and military laser applications can reach power levels in the order of magnitudes of petawatts [22]. The laser driver ensures the safe operation of the LD by managing the current [21].

A monitor photodiode (PD) can be integrated into the LD package. This PD produces a current proportional to the optical laser output power. A LD driver, such as seen in Figure 2.12 will allow control based on either LD current or PD current. More about this follows below in **APC vs. ACC**. Current flows through the LD and is regulated by the adjustable current source. I_{MON} and P_{MON} represent the current through the LD and the current through the PD, respectively [21].

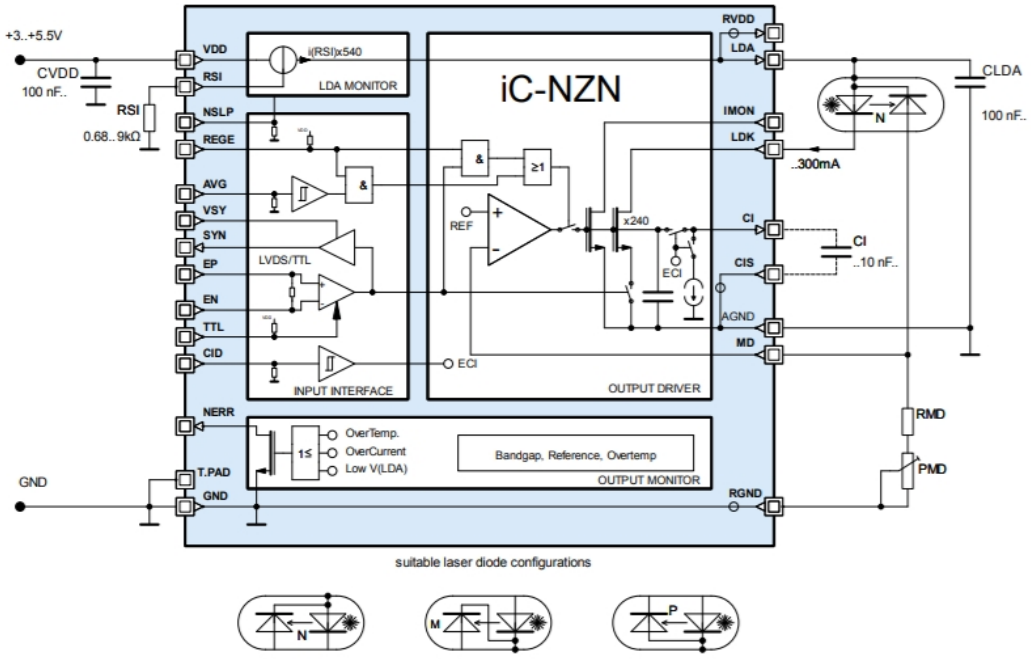

Figure 2.12: iC-Haus iC-NZN N-type laser diode driver block diagram. Source: [24]

The summing amplifiers measure the difference between the setpoint and the actual current or sum the setpoint resistance or potentiometer with an external pulse signal. The error between the user-determined setpoint and actual PD or LD current is modified to make an electronic signal that properly drives the adjustable current source to reduce the error to a minimum [21]. The limit circuit is an essential part of the driver. It protects the LD against overcurrent and overtemperature. Additionally, there are some built-in safety functions in most laser drivers that significantly improve the reliability of the LD. Features that allow this are suppression of transients, brownout prevention, and soft start [21]. An external power supply V_{DD} feeds the control electronics for the laser driver. This is usually a low voltage ranging from – 3.3 V to 5 V DC [24]. Additionally, an external power supply V_S feeds the adjustable current source electronics. This is the DC voltage that is needed to power the LD itself and can be found in the datasheet [21].

APC vs. ACC

There are two options on how to regulate the laser. The first method is to maintain a constant PD current. This is also known as Automatic Power Control (APC). For this configuration, the LD drive circuit is based on the PD's feedback, which monitors the optical laser output power. The control feedback loop then ensures that the diode operates at a constant optical output level. The APC mode prevents an increase in the optical power output as the LD's temperature decreases. The issue here is when that jumps and changes in wavelength are still possible [26]. Additionally, when the heat sink capabilities are not on par with the required cooling, the optical output power will still decrease along with the increase of temperature. To compensate for this and to maintain the same optical power output, the APC laser driver circuit will boost the LD drive current. This can lead to thermal runaway and the deterioration of the LD, or in the worst case, to a defective LD.

The second is to keep the LD current constant. The term used for this is Automatic Current Control (ACC). The ACC LD drive circuit operates the LD without using the PD feedback loop, and the current is held at a constant level. As a result, the optical laser power output fluctuates as a function of the LD temperature. ACC combined with control of the diode's operating temperature is generally the preferred operating method. The constant current mode provides a faster control loop and a precision current reference for accurately monitoring the laser current. Further, in many cases, the LD's internal PD may exhibit drift and have poor noise characteristics. If the performance of the internal PD is inferior, the diode's optical output is likely to be noisy and unstable as well.

Using ACC in environments with fluctuating temperatures is not advised, as the optical power output of a laser will increase when the temperature decreases. However, due to the constant current, there is no danger to encounter an overcurrent on the LD, unlike APC [23]. This can be seen in Figure 2.13, on the left, the ACC mode shows the constant current, while on the right, APC shows the constant power output. In order to achieve a fast, stable, and safe operation with maximum laser lifetime, ACC is needed using a temperature-controlled environment.

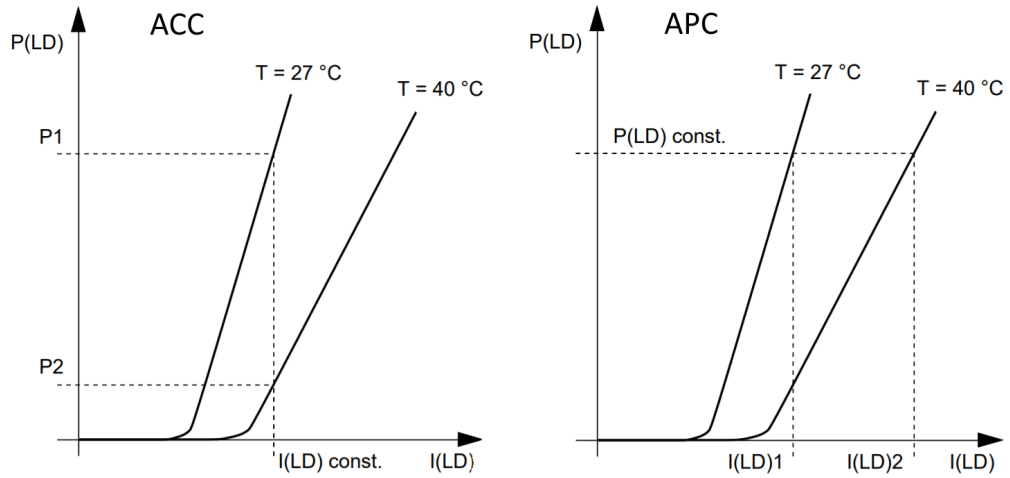

Figure 2.13: Graphs showing the difference between ACC and APC. Source: Adapted from [23]

2.5 PCB Design rules

High performance will only be achievable when the designed circuits adhere to specific PCB (Printed Circuit Board) guidelines. Besides the issues that could manifest for PCB in question, bad design can also cause problems for adjacent electronics. Due to the sensitive nature of PCB traces, this would be detrimental. By applying the knowledge of electronics in devices that manipulate electric currents and/or electromagnetic fields. This allows information to be sent, received and/or manipulated. Furthermore, energy can also be distributed, regulated, and controlled [27]. In order to fabricate PCBs with high quality, it is essential to look out for feedback loops, inductive or capacitive traces, and correctly use decoupling capacitors, etc [28].

2.5.1 EMC/EMI

Bad PCB design can cause trouble within and outside of the PCB. This happens in the form of electromagnetic compatibility (EMC) and electromagnetic interference (EMI) issues. A technique used to counter these effects can be found in via stitching and via shielding. During the finalization of the PCB design, via stitching is used to create low impedance and short return loops. It also joins isolated copper islands to their respected net. Via shielding is better suited to counter crosstalk and EMI on radio frequency (RF) carrying traces. The difference between the two is made clear in Figure 2.14. [29, 30].

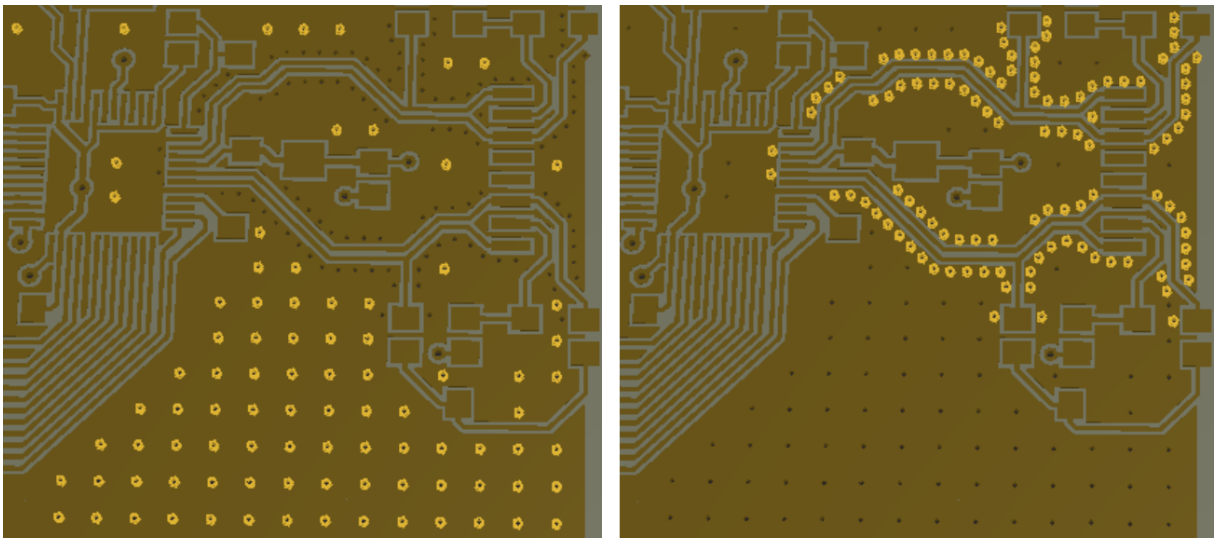

Figure 2.14: Via stitching on the left, via shielding on the right. Source: Adapted from [30]

2.6 Heat transfer in micro-gravity

Heat transfer can occur by three different methods. Conduction, convection, and radiation. It takes place when there is a temperature difference. The time in which the transfer of heat takes place depends on the thermal capacity of the materials at hand and on the absolute difference in temperature itself. Heat transfer always happens from the higher (T_h) to the lower temperature (T_C) and continues until an equilibrium has been reached. This can be seen in Figure 2.15, in the form of a high energy molecule losing its momentum due to a collision with a low energy molecule which gains momentum to the increased energy level. Conduction is when heat is transferred through solid matter by means of physical contact. Convection is referred to as heat transfer by the movement of fluids and gasses. Radiation is the transfer of heat through the emission of electromagnetic radiation, such as infrared radiation, MW, and visible light [31].

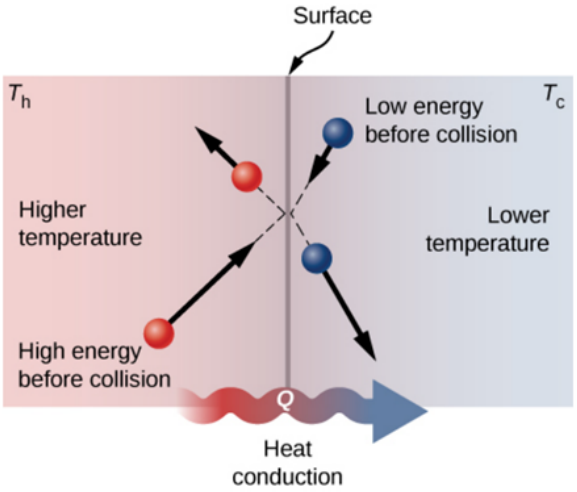

Figure 2.15: Heat transfer representation. Source: [31].

In microgravity environments, the way heat transfer occurs changes. Heat transfer by radiation is the sole unaffected manner of heat transfer in microgravity environments. Heat conduction is reduced for gases as microgravity environments reduce gas density, solids and liquids are not affected. Convectional transfer of heat is affected due to gravity's effect on fluid motion. Evaporation, boiling, condensation, two-phase forced convection, and phase-change heat transfer are dependent on gravity. For the boiling of water, this can be seen in Figure 2.16, in a zero-G environment, the bubbles do not behave like in a one G environment [32].

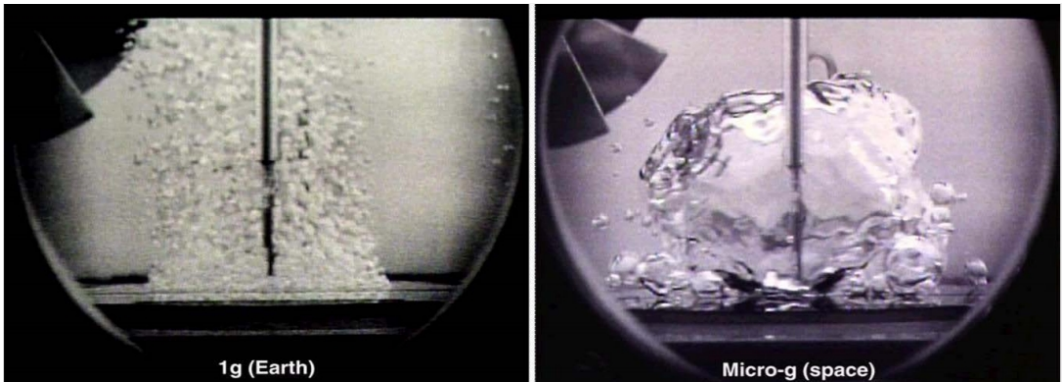

Figure 2.16: The effect of gravity on the boiling of water. Source: [32]

Chapter 3

Materials and methods

In this chapter, the general approach of the project is handled and which steps have been taken. For a start, the hardware and software used within the scope of this thesis are described. As well as in which manner these contributed to the completion of the project.

3.1 Hardware

NZN1D evaluation board

In order to learn about the operation and working of the iC-NZN laser diode driver, the NZN1D evaluation board was used. This board features the necessary circuit and connections, as seen in Figure 3.1, to test every operation mode that the driver features on an N-Type laser (Section 2.4.1). This board allows for CW operation and spike-free switching (pulsing) of laser diodes. For the optical output power of the laser diode, an external resistor is used. As a function as the limit circuit, as described in Section 2.4.3 and shown in Figure 3.3, the maximum current flowing to the laser diode is limited by the use of an external resistor [24, 33].

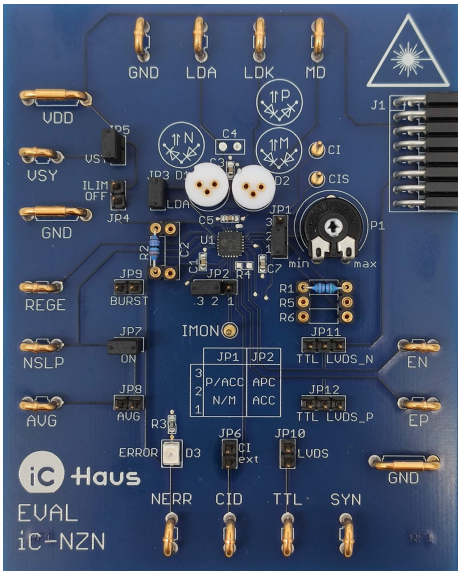

Figure 3.1: NZN1D evaluation board.

iC-NZN Laser Diode Driver

The driving force behind the Thorlabs L520P50 laser diode is the iC-NZN Laser Diode Driver. This driver allows for CW operation and spike-free switching (pulsing) of laser diodes up to 300 mA. It features APC and ACC operating modes and has a safety shutdown feature that kicks in with overtemperature. The iC-NZN Laser Diode Driver also features an error signal output to alert in the case of overtemperature, undervoltage, and overcurrent. By using the NSLP pin, the iC can go into a low energy consumption sleep mode. The consumption in this mode is typically less than 50 µA [24].

Within the datasheet [24] electrical characteristics timings are also included. To go from NSLP to wakeup state takes the driver 300 μs. Both laser current rise (t_r) and fall (t_f) time take 1.5 μs. This is seen in Figure 3.2. The propagation delay amounts to 10 μs.

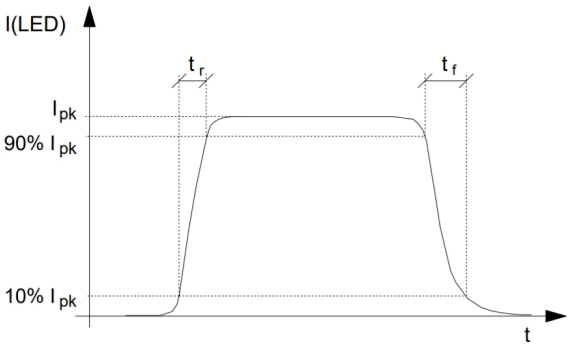

Figure 3.2: Schematic representation of a laser driver. Source: [24]

To give some more context to this description, a fundamental laser diode driver is shown in the block diagram as seen in figure 3.3. This block diagram is a laser drive model meant to inform the reader about the terminology and essential elements. For more information, please refer to Section 2.4.3.

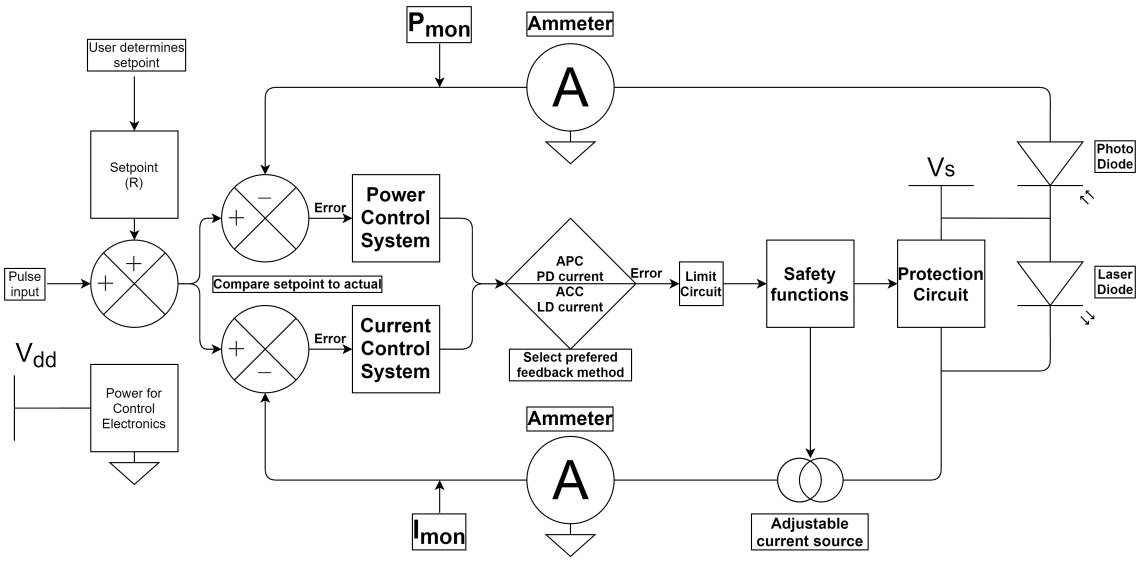

Figure 3.3: Schematic representation of a laser driver.

Thorlabs L520P50 laser diode

Most important in describing a laser, its specific characteristics are the wavelength, output power, and input power. The laser diode used in the OSCAR-QUBE project is the Thorlabs L520P50. This N-type laser diode produces a visible (green) laser beam of 520 nm with a maximum optical output power of 50 mW while rated for a maximum input power of 1.05 W. The laser diode uses a TO package with a 5.6 mm diameter in an A-pin configuration, as can be seen in Figure 3.4. The diode offers a modulation frequency of at least 100 MHz. The datasheet also recommends using a heat sink with a suitable thermal connection to the base of the laser diode [34, 35].

Figure 3.4: Thorlabs L520P50 laser diode.

Thorlabs PM100D Power Meter & S121C Power Head

The Thorlabs PM100D is the handheld optical power meter used within the scope of this thesis to measure the optical power of the laser light. The sensor used in conjunction with this power meter is the S121C power head, as can be seen in Figure 3.5. Aside from monitoring power output on-screen and saving it to the SD-card, connecting the PM100D to a computer also enables the use of Thorlabs software to monitor and capture the results on the computer [36, 37].

The sensor used in conjunction with the Thorlabs PM100D is the Thorlabs S121C power head. The design of this sensor made it easy to measure the optical laser output power within the tight constraints of the OSCAR-QUBE. The sensor has a measuring range for laser output powers from 500 nW up to 500 mW for wavelengths going from 400 nm to 1100 nm [38, 39].

Figure 3.5: Thorlabs PM100D Power Meter & S121C Power Head

MAX5483 Digital potentiometer

In order to control the output power, a Maxim Integrated MAX5483 digital potentiometer is used. This potentiometer offers 10 bit (1024 levels) control over a resistance range from 0 Ω to 10 KΩ. Furthermore, the MAX5483 has a linear gradient and features non-volatile behavior. This potentiometer can be powered in various ways, it can operate with either a +2.7 V to +5.25 V single power supply or ±2.5 V dual power supplies while it consumes 400 μA (max) when writing data, and 1.0 μA (max) when in standby [40].

The communication between the STM32 MCU and the programmable resister is done using a pin configurable 3-wire serial SPI interface [40]. This is done using the SPI, DIN, SCLK, and $\overline{CS}$ pins provided as seen in Table 3.1. This allows setting the optical laser output power. More can be seen in Section 3.1.

Table 3.1: SPI pin description MAX5483. Adapted from [40]

SPI	Interface-Mode Select. Select serial SPI interface when SPI = 1. Select serial up/down interface when SPI = 0.
DIN	Serial SPI Interface Data Input (SPI = 1)
	Up/Down Control Input (SPI = 0). With DIN low, a high-to-low SCLK transition decrements the wiper position. With DIN high, a high-to-low SCLK transition increments the wiper position.
SCLK	Serial SPI Interface Clock Input (SPI = 1)
	Wiper Increment Control Input (SPI = 0). With $\overline{CS}$ low, the wiper position moves in the direction determined by the state of DIN on a high-to-low transition.
$\overline{CS}$	Active-Low Digital Input Chip Select

TP-Link TL-WR702N

This router was used to communicate with the OSCAR-QUBE wireless when using a physical Ethernet cable was not possible. Due to its small dimensions (57 × 57 ×18 mm) [41] this router could easily be fitted along with the OSCAR-QUBE in the vacuum bell for testing. The router can be powered using a micro USB port using a 5 V power supply [41]. These low power requirements made it easy to run parasitically on the power lines going to the OSCAR-QUBE.

FLIR i7 Thermal Imaging Camera

In order to capture thermal images from the OSCAR-QUBE during testing, the FLIR i7 thermal imaging camera is used. This thermal imaging camera features an image resolution of 140 by 140 pixels with a thermal sensitivity of less than 0.15°C at a temperature of 25°C. The FLIR i7 is optimized for a temperature range going from –20°C up to 250°C [42].

Vacuum bell and Trivac D2.5LD vacuum pump

The Vacuum bell used during the project is a University-owned model seen in Figure 3.6, with a diameter of roughly 25 cm. It features a pass-through for up to three wires which were used for the ground, 12 V, and 5 V lines to supply power to the OSCAR-QUBE. The large size was needed to accommodate the OSCAR-QUBE, the connection interface for the DB13W3 connector, and the router to enable the wireless interface to communicate with the OSCAR-QUBE. The medium vacuum was formed using the Leybold Trivac D2.5LD vacuum pump (Figure 3.7). It is a dual-stage oil-sealed rotary vane vacuum pump and rated for 2.5 m^3/h [43].

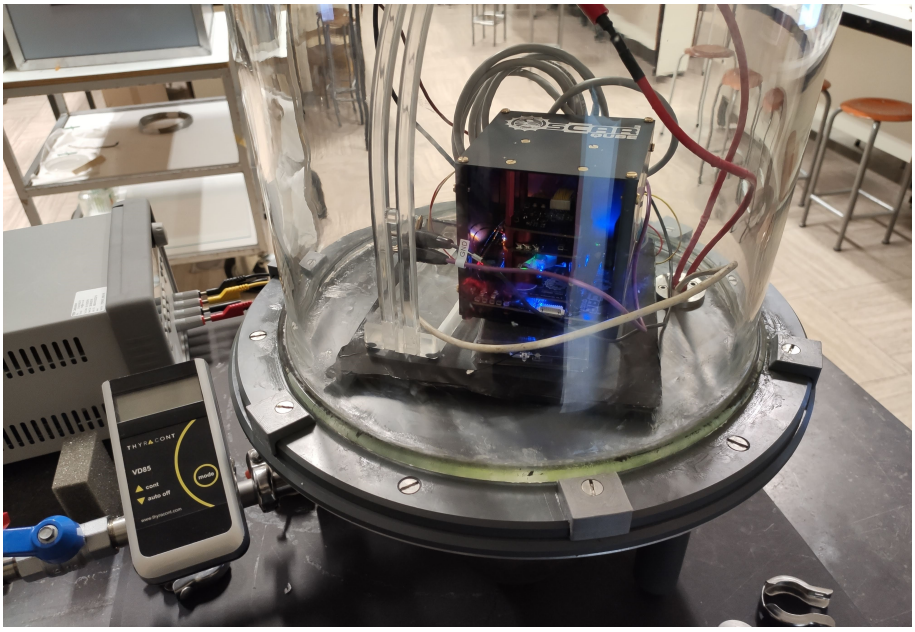

Figure 3.6: OSCAR-QUBE in the vacuum bell under atmospheric pressure.

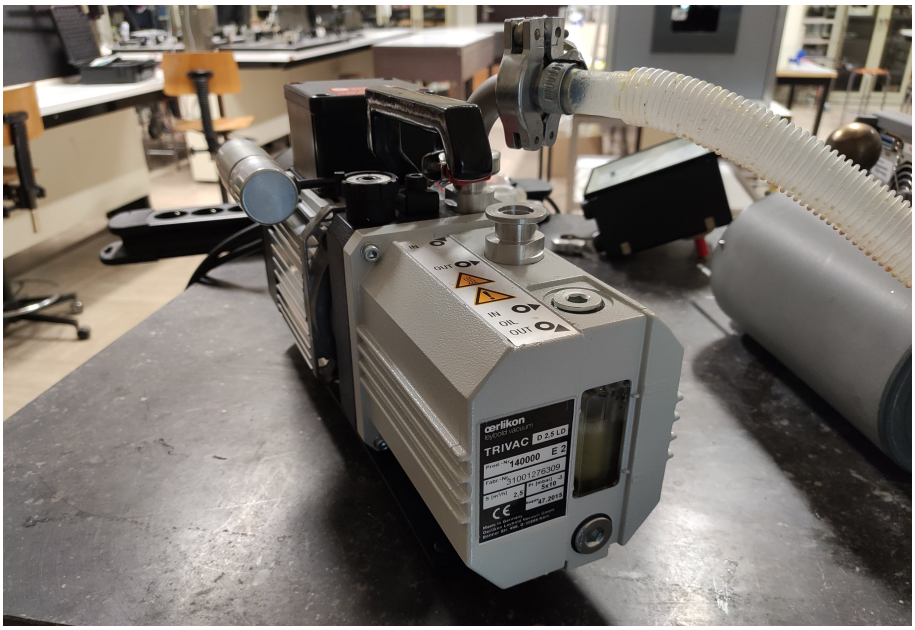

Figure 3.7: Trivac vacuum pump.

FPGA

The Field Programmable Gate Array (FPGA) allows the MW and laser subsystems to perform advanced pulsed measurement techniques. An FPGA is required for this due to the limited speed of the MCU GPIO pins. Using the STM32 for this objective would bottleneck the measurements. Therefore, an additional part in the form of an FPGA is introduced. This will handle the switching of the laser and MW subsystems to create the TTL pulse sequences with a minimum pulse width of 10 ns. Based on the size, performance, and availability, the decision was made to integrate an existing FPGA in the form of a commercial-off-the-shelf (COTS) component. For this, a Xilinx Artix-7 based FPGA development board, more specifically the Digilent Cmod A7-35T [44], was integrated onto the powerboard with the output channel signals being guided to the destination boards using UFL connectors.

Analog Discovery

The Digilent Analog Discovery 2, as seen in Figure 3.8 is a multi-functional USB oscilloscope. It enables users to measure and visualize frequency signals. It was designed to replace several laboratory devices, such as, Oscilloscopes, Waveform and Pattern Generators, Power Supplies, Voltmeters, Data Loggers, Logic, Static I/O, Spectrum, Network, Impedance, and Protocol Analyzers [45]. The protocol analyzer can check SPI, I2C, CAN, AVR, and UART. The 16-channel digital logic analyzer is able to measure at a rate of 100 MS/s, 100MS/s). This all can be utilized using the accompanying software package [45].

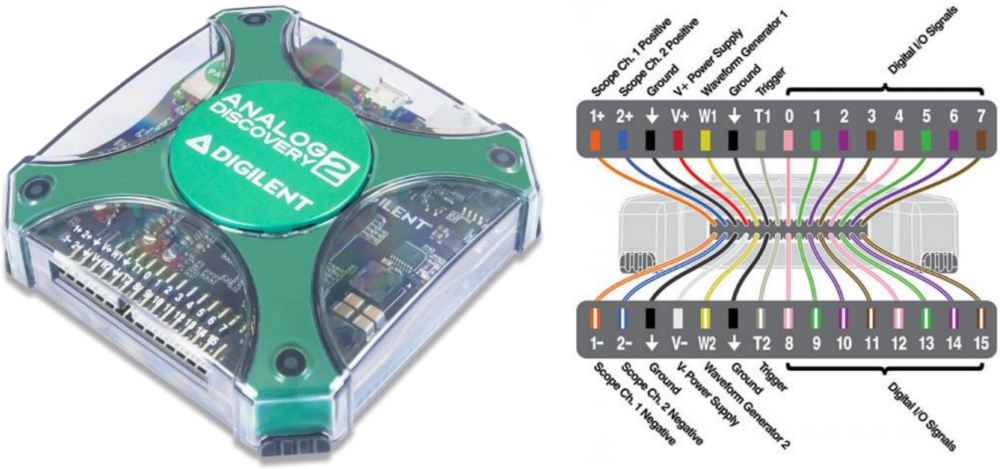

Figure 3.8: The Analog Discovery 2 and its pinout diagram. Source: Adapted from [45]

3.2 Software

Altium Designer

The PCB design process combines placing components and routing their electrical connections to connect the components physically. First, electrical schematics have to be made. These represent how every component is connected to each other electrically. Next, the layout of the components has to be determined, this is the placement of the components in a physical space. Finally, the PCB has to be routed. This is considered to be both art and science by many. The routing is making the electrical connections between components on the PCB. To do all of this, some software is required to make the process easier. The software used in this project to design circuits schematics and the PCB designs is Altium Designer version 20 and version 21. This is a well-known software package in the PCB design world. Being well known is not necessarily a good thing. Many consider Altium to be over-priced. This particular software package is used because, as students, the OSCAR-QUBE project can use it free of charge [46].

Packet Sender

As a means of communicating with the OSCAR-QUBE Packet Sender is used. This free open-source software (GNU General Public License v2) utility enables the transmission of TCP (Transmission control protocol) and UDP (User datagram protocol) data packets. The software is available for Windows, Mac, and Linux devices [47].

For the OSCAR-QUBE UDP packets are used for several reasons. Due to the nature of the project, fast readout and thus data-throughput are preferred. By design, UDP allows for faster, easier, and more efficient operation when compared to TCP. As the OSCAR-QUBE has limited power and resource expenditures, this is welcome, being limited to a maximum of 10 W and having an STM32 MCU (Micro Controller Unit). The disadvantage is that the delivery of the data packets is not guaranteed with UDP, unlike with TCP. Along with that, UDP only offers basic error checking using checksum verification.

Wireshark

To inspect the communications send with Packet Sender and to analyze the incoming packets, Wireshark is used. Wireshark is a free-to-use open-source network protocol analyzer [48]. It enables the user to inspect incoming and outgoing data communications over a range of connections, such as, but not limited to, Ethernet, WiFi, Bluetooth, USB,...

Python

For the processing of data and the creation of graphs, the Python programming language is used. The large coding community behind Python and the many libraries available make it especially useful to write and use programs quickly. Thanks to the built-in functions and the addition of libraries such as matplotlib, NumPy processing, and visualizing data has become a lot easier [49, 50].

3.3 Model philosophy

The method used within the engineering of the OSCAR-QUBE project revolves heavily around schematic and PCB design. Thanks to the feedback loop within the process, errors, flaws, or performance issues could be detected early on, as seen in Figure 3.9. The TBM was used for precisely this. After this, the PFM 1 and 2 were made, improving on the initial design. Finally, the best performing version was selected to be the FM, and the lesser model became the GM.

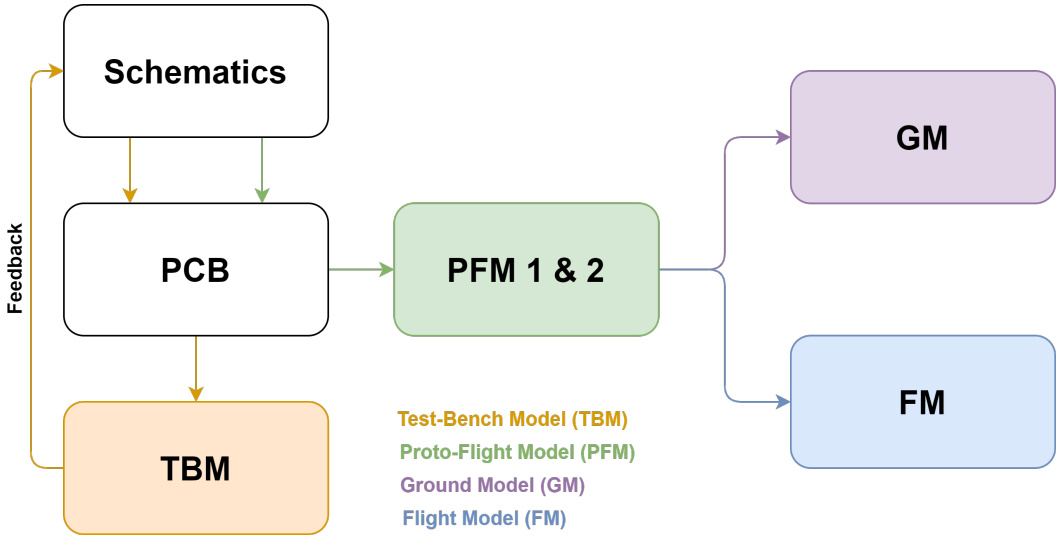

Figure 3.9: Project method process

3.3.1 Test-Bench Model

The test bench model (TBM) of the OSCAR-QUBE contains all of the subsystems separated into their individual functional blocks and put together so that verification, optimization, and debugging of each subsystem can be quickly done before the complete system integration. The TBM was built on an optical test bench. The optics and optical solutions used are identical to the ones used in the following models. The main difference is that the TBM was equipped with motorized stages to facilitate the scanning of the diamond sample. This step has proven very helpful for automated processes related to verifying the underlying physics principles and will speed up the development. The subsystems were designed and placed on separated PCBs, and each board has a dedicated microcontroller unit (MCU). This approach allowed the team to develop and test the software for the individual boards.

3.3.2 Proto-flight model

When comparing the TBM to the PFM versions, the changes are more apparent. First, the motorized XYZ stage used for scanning and mapping the diamond sample is not required in the PFM design. The PFM is a fully integrated model containing the verified to be working subsystems from the TBM. The Proto-flight models (PFM), PFM1, and PFM2 were distinguishable by the difference of the diamond sample. The sample used in PFM1 has the internal sample number #353. The sample used in PFM2 is #369. Aside from this, both PFM1 and PFM2 feature the same hardware being virtually identical. PFM2 with sample #369 has been promoted to FM and will travel to the ISS aboard a SpaceX rocket to perform measurements in orbit.

To summarize, the PFM versions have:

- Integrated design
- Permanent magnet holder
- Laser focuser & Photodiode housing
- Layout in form of stack
- Single control MCU with Ethernet interface

3.3.3 Ground and Flight Model

The Flight Model (FM) is the PFM2 using the #369 diamond sample. It was built up from scratch after the TBM. This ensured that all issues found in the TBM model to be resolved. This model was used to do all the necessary acceptance tests and will be placed aboard the ISS. Currently, this model has been approved and shipped to Turin, Italy, for the payload integration by ESA. The Ground Model (GM) is mainly identical to the FM, as seen in Figure 3.10. It will be used for troubleshooting and comparison of the FM during the experiment operation. The GM is PFM1 using the #353 diamond sample and can be recognized by the missing sticker compared to the FM.

Figure 3.10: PFM1 or GM on the left, PFM2 or FM on the right

Chapter 4

Experimental

4.1 System overview

The OSCAR-QUBE consists out of several critical subsystems with their own dedicated functions. The focus for this thesis is on the Laser Subsystem, indicated in Figure 4.1 by the orange dashed line. Other subsystems are the control, microwave, reference, optical readout, and photocurrent readout subsystem.

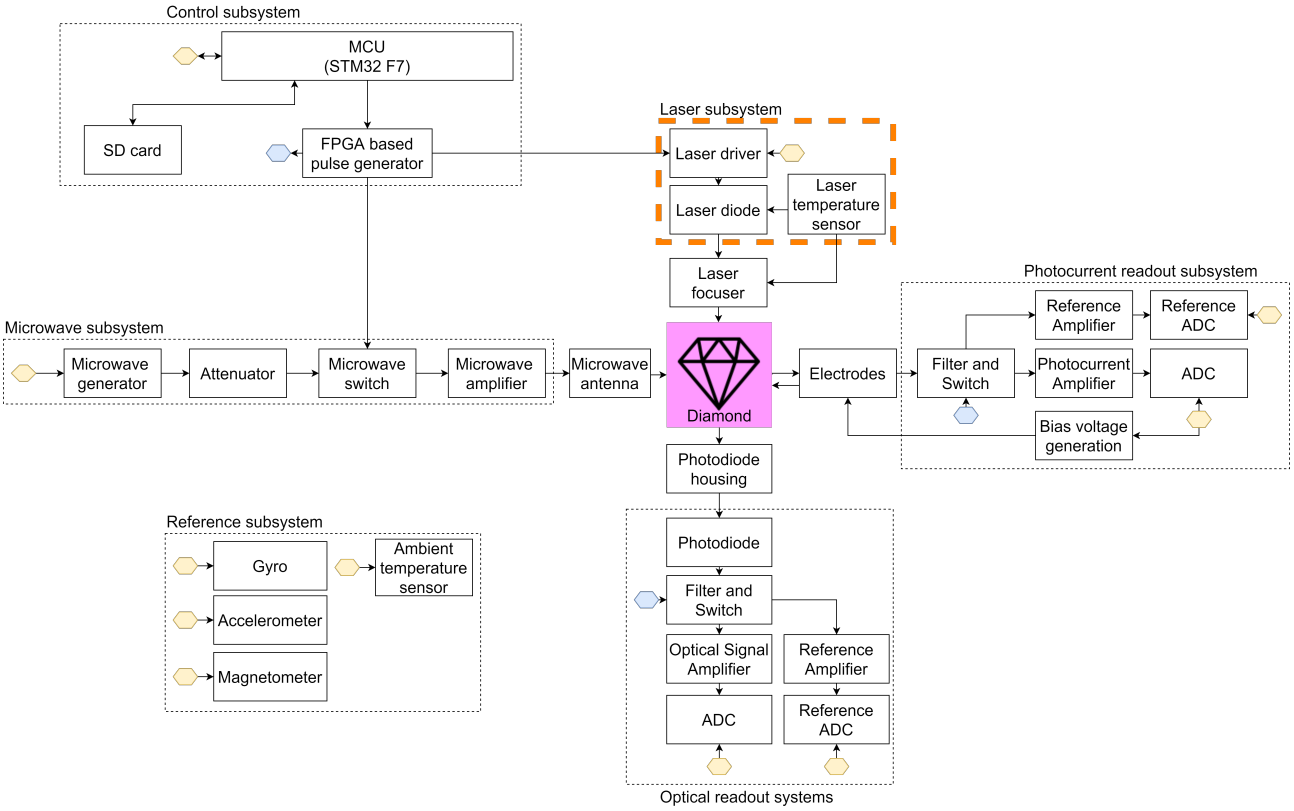

Figure 4.1: High-level subsystem overview for OSCAR-QUBE

4.2 Board stack

The subsystems seen in the previous section are integrated into the internal stack of the OSCAR-QUBE. This stack consists of four individual PCBs, as can be seen in Figure 4.2. The control and reference subsystem can be found on the power board. The MW and photocurrent readout subsystems are integrated into the science board. The optical readout system can be found on the optical board. Lastly, the laser subsystem is located on the laser board. The science, laser, and optical boards together make up the sensor part of the OSCAR-QUBE. The power board is equipped with a DB13W3 connector to interface with the Ice Cube Facility (ICF). The power board has the required mounting points to build up the entire sensor stack-up. The boards are attached to each other mechanically with brass standoffs.

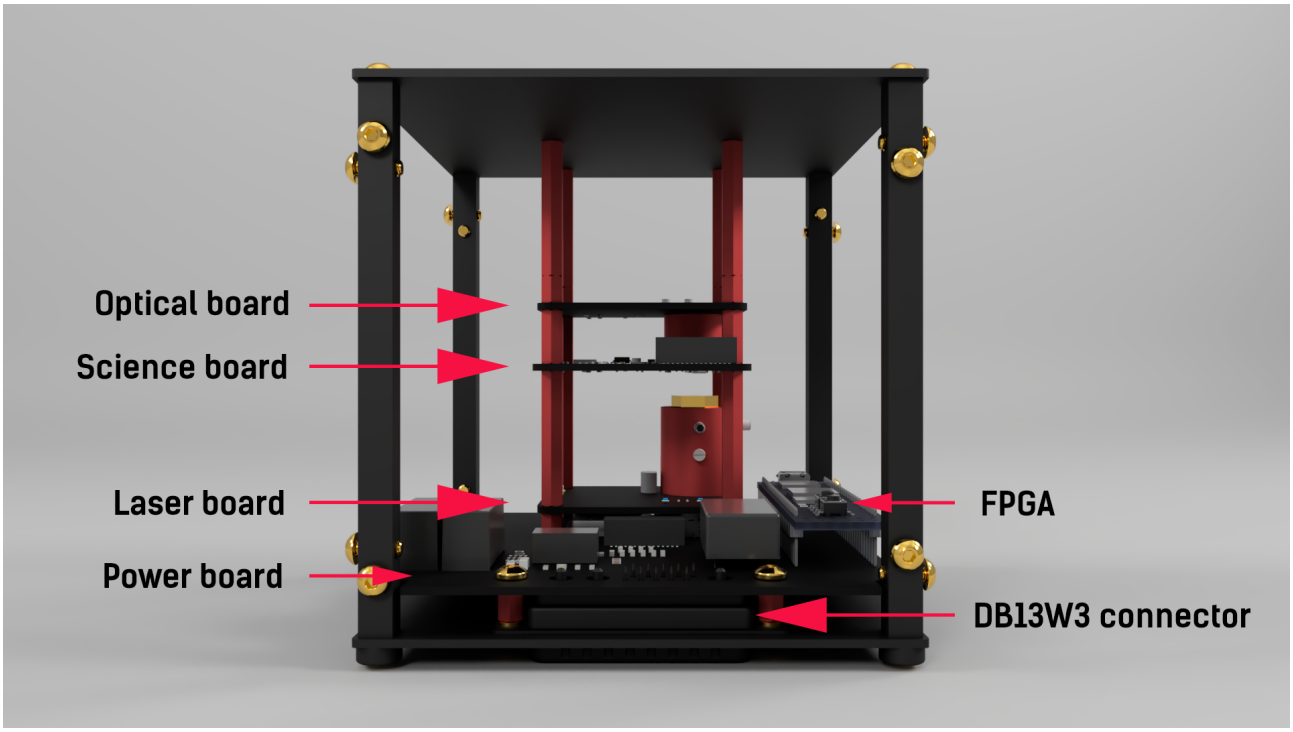

Figure 4.2: The internal stack layout of the OSCAR-QUBE

4.3 Laser Subsystem overview

The laser board is a custom board that holds the laser and the corresponding laser driver as seen in Section 3.1 and 3.1. This board is connected to the power board by a board-to-board connector. The laser board receives ground, power, and data signals from the power board. The power signals used for this subsystem consist of 3V3 and 7V. The 3V3 power is required for the laser driver (iC-NZN, IC1) and the programmable resistor (MAX5483EUD+, U1), which is used to fine-tune the laser power output. The 7V is required to drive the laser diode (L520P50, Thorlabs).

The laser subsystem makes use of a green LD with a center wavelength of 520 nm. The laser is controlled by a laser driver IC, which controls the output power of the LD. This driver allows for CW operation of LDs and spike-free switching with defined current pulses up to 155 MHz for pulsed operation. The optical laser power output of the laser subsystem can go up to 50 mW. This power output is regulated by the programmable resistor, which is controlled by the microcontroller. This by changing the value of the resistor (0-1023) to the desired setting. For additional information, an external temperature sensor (LMT86LP, U2) is bonded to the aluminum housing of the laser focuser. This sensor enables a precise temperature readout rather than an over-temperature warning through an error state that the laser driver provides.

The data signals are also carried over from the Power Board to the Laser Board. These signals are needed to adjust the laser driver and programmable resistor as needed. Both the control signal for the laser from the FPGA and the communication with the temperature sensor (LMT86LP, U2) are carried over UFL connectors. The temperature sensor enables feedback to the STM32 chip on the laser housing temperature. The FPGA ensures correct timings are used to activate the laser. Additionally, there are two status LEDs placed on the PCB, which the MCU can control.

The programmable resistor can be controlled by the microcontroller using 3-Wire Serial SPI. By writing specific values to the internal registers of the resistor, the microcontroller can configure the output power of the LD. This laser driver also outputs an error state when it detects over-temperature and overcurrent. The LD is enclosed into a housing. This housing has multiple functionalities. It enables the fine-tuning of the X, Y, and Z-axis to focus perfectly on the diamond sample. Additionally, the housing acts as a passive heatsink, distributing the heat generated during operation. This ensures the laser operates within its operational temperature range and prevents overheating.

All the capacitors on the board are ceramic and SMD. The dimensions of the board are 47.1 mm by 41.7 mm. The material of the PCB is FR4. The PCB is not conformal coated. The electrical schematic of the Laser Subsystem can be seen in Figure 4.3. The major components of the laser subsystem and the accompanying power consumption values can be seen in Table 4.1. The location of these components can be seen in Figure 4.4 and Figure 4.5.

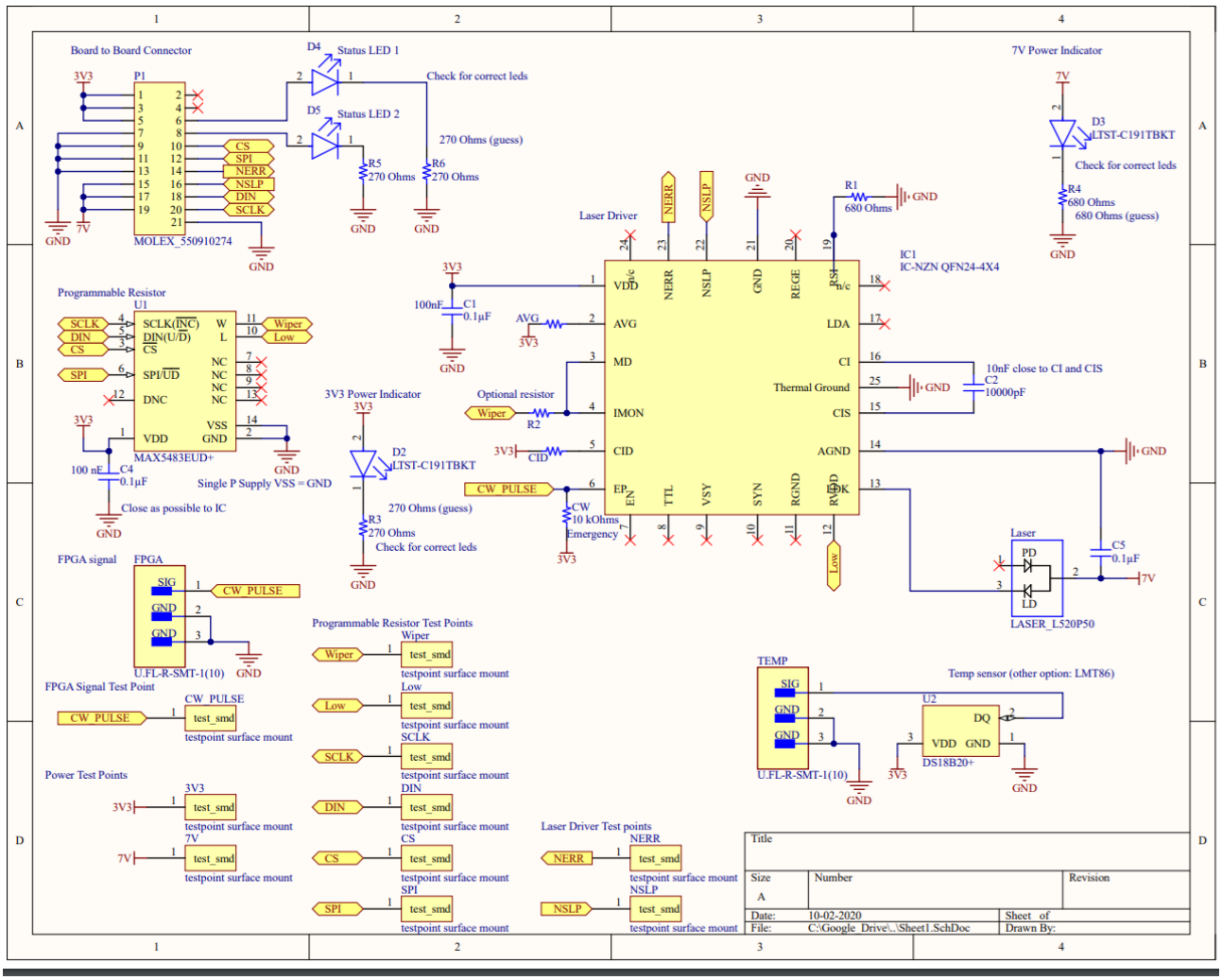

Figure 4.3: Electronics schematics of laser subsystem

Table 4.1: Main components and power consumption of the Laser Board

#	Component name	Nominal power consumption
1	Thorlabs L520P50	1050 mW (CW Max power)
2	Texas Instruments LMT86	17.82 μW
3	Maxim integrated MAX5483	13.2 mW
4	iCHaus iC-NZN	33 mW

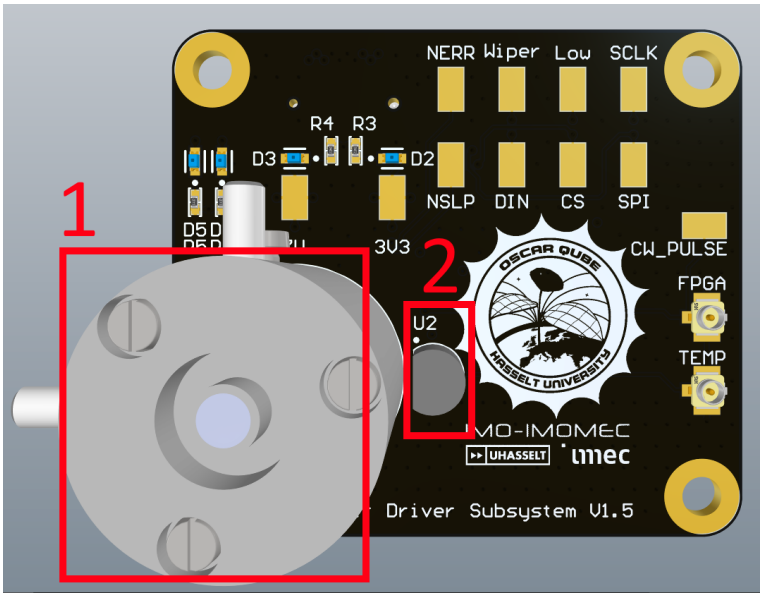

Figure 4.4: 3D view of the PCB: Top view

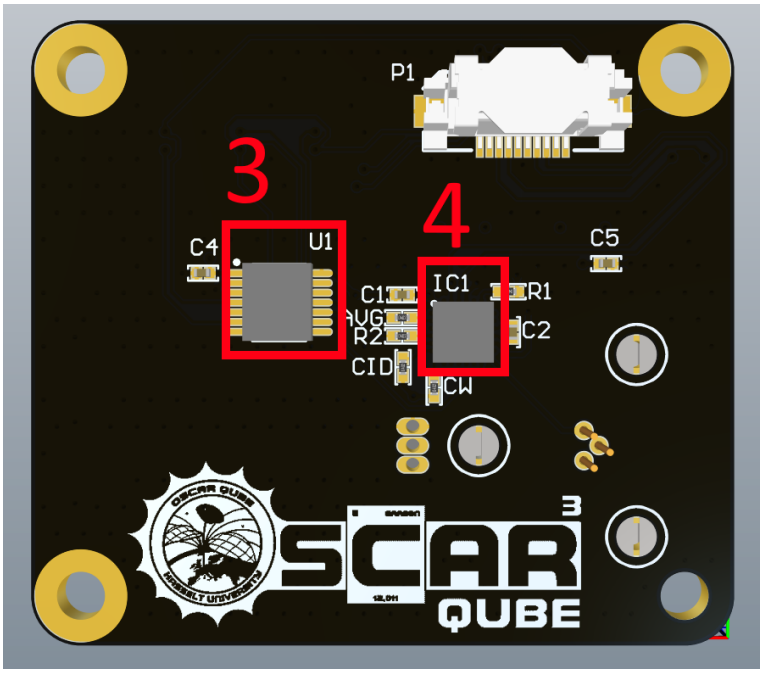

Figure 4.5: 3D view of the PCB: Bottom view

4.4 Subsystem testing

In this section, an overview of the work done in function for the laser subsystem itself is reported. This includes initial testing on components, the PCB, and the basic working of the subsystem itself. For the results and discussion of these tests, please be referred to section 5.1 of Chapter 5.

4.4.1 Laser driver evaluation kit

For the TBM, the Laser driver evaluation kit needed to undergo verification. To verify the basic working principle, it first of all needed to be able to drive the LD, as is seen in Figure 4.6. This for two configurations. Continuous-wave (CW) operation and pulsed operation.

Following the basic verification of the evaluation kit, its electrical schematics were analyzed in order to come up with a schematic for the project, as seen in Section 4.3. This schematic then needed to be routed in order to make a PCB. For this, the necessary components and placement requirements for the optimal performance needed to be checked against the datasheets.

The laser driver can use Automatic Power Control (APC) or use Automatic Current Control (ACC) mode to drive the laser. In order to have complete control of the laser output power, the ACC mode is used. This is most important in the high-power setting of the laser needed for PDMR. ACC, as the name suggests, offers a fixed current. Therefore, there is no real danger of overcurrent.

One disadvantage is that the laser output power slightly changes when the temperature changes. With APC, there is a risk of overcurrent with self-heating or aging effects of the LD, as the driver allows for additional current to be used to maintain an output power. This could lead to critical optical destruction (COD), resulting in a non-operable LD.

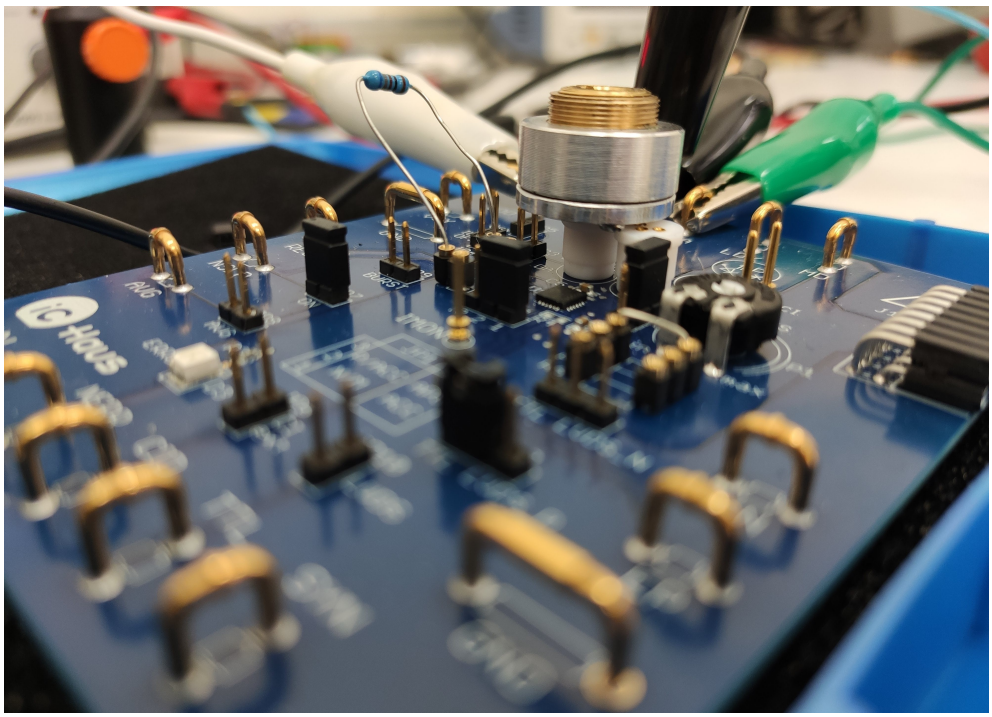

Figure 4.6: Preparations for testing on the iC-Haus evaluation kit.

4.4.2 Digital potentiometer

The NZN evaluation kit features a built-in analog potentiometer used to control the resistance values. However, due to the nature of this project, an alternative method is needed. The resistance needs to be tweaked with great accuracy in order to allow the system itself to operate without any issues. For the integrated solution, a digital potentiometer is needed.

In order to change the resistance, and therefore, the optical laser output power, the MAX5483 digital potentiometer got selected based on its 10-bit resolution and resistance range going from 0 Ω to 10 KΩ. Communication with this digital potentiometer takes place using the SPI protocol. Thanks to the built-in EEPROM (electrically erasable programmable read-only memory), the potentiometer can store the wiper position after being powered down and re-initialize it during start-up.

Testing was performed to verify its performance, the minimal and maximum resistance, and the linear behavior that it had according to the datasheet. Preparations can be seen in Figure 4.7. This is done using a 14-Pin SOIC to DIP Adapter, Nucleo development board (Communications), and a multimeter.

Figure 4.7: Preparations for testing on the MAX5483 using a 14-Pin SOIC to DIP Adapter on breadboard setup, seen on the left.

4.4.3 PCB

The PCB created for the laser subsystem offers two different voltages. All main electronics have been selected to work on a 3.3 V supply while the LD runs on a 7 V line. The powerboard provides these voltages through the use of a board-to-board connector, as seen in Figure 4.8. The test points (Figure 4.9) designed into the system offer an easy manner of verifying that the voltages are indeed correct.

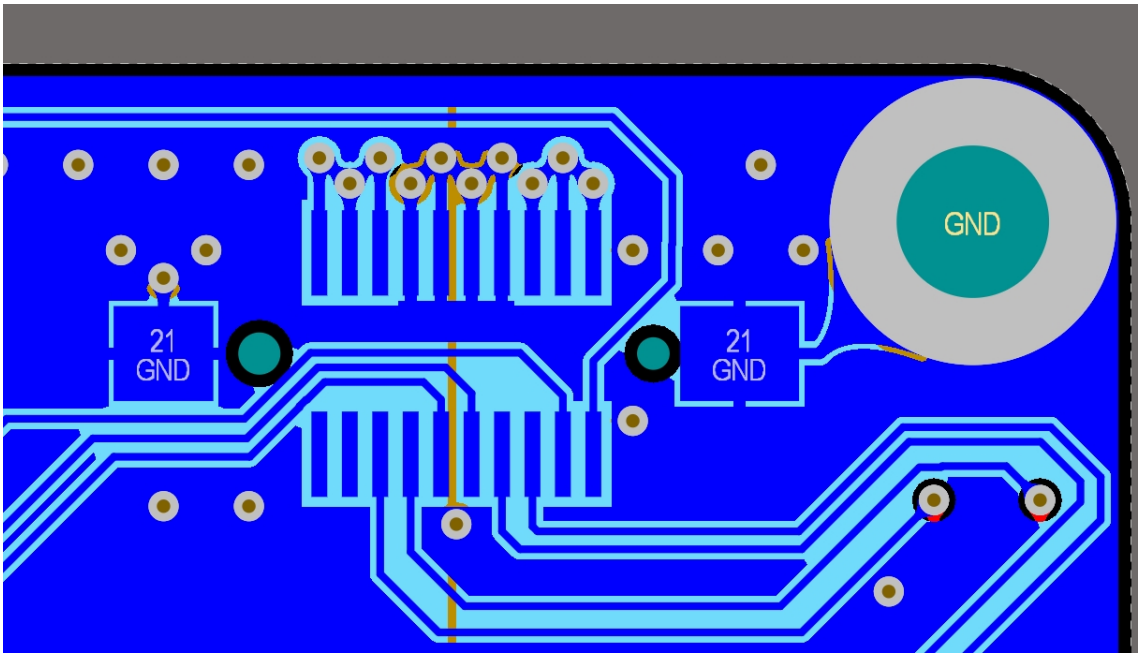

Figure 4.8: Board to board connector as seen in Altium Designer.

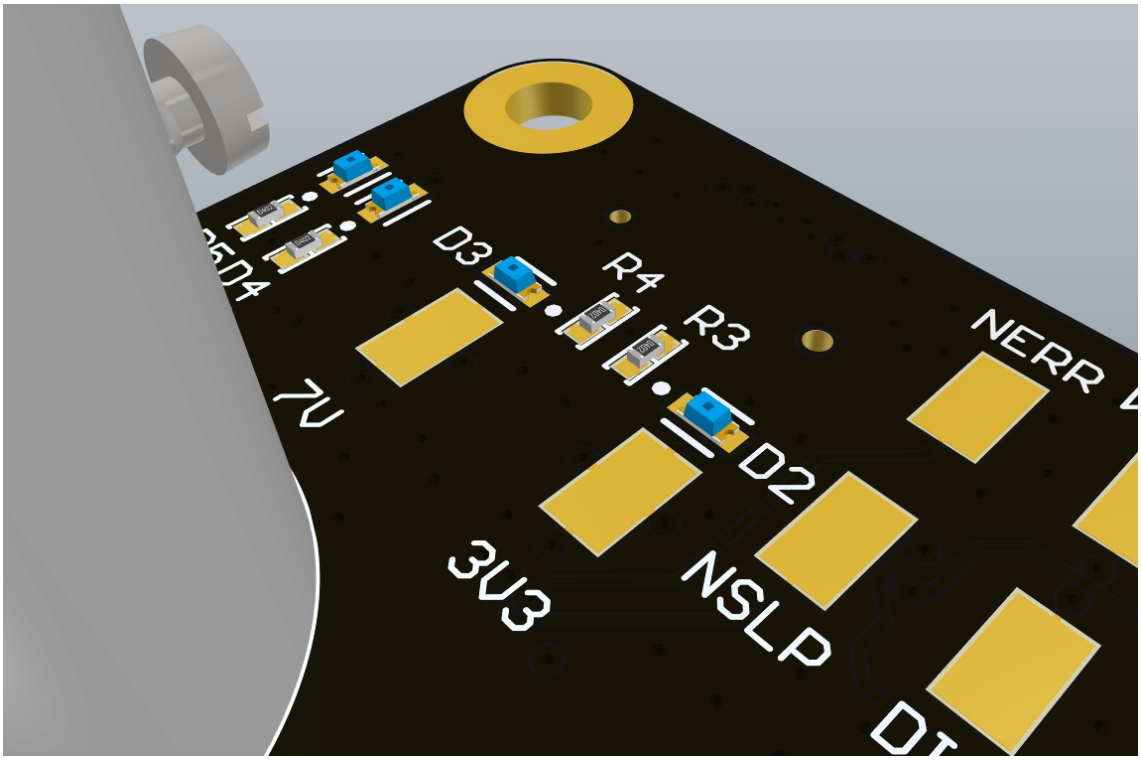

Figure 4.9: Testpoints on the laser subsystem PCB.

4.4.4 Driver and diode

For the laser subsystem, the long-term stability of optical laser output power is the most important for the final system. In order to measure the stability, the Thorlabs PM100 power meter was used in conjunction with the S121 Power Head. The laser beam itself was collimated to focus all of the output power in the measurement zone of the S121 Power Head.

The PM100D can measure the power output continuously at a rate of 200 samples per minute. During testing, seen in Figure 4.10, the OSCAR-QUBE is connected to the +12 V and +5 V rails provided by the lab power supply. An Ethernet cable is used for communications. The S121 is clamped into a heavy holder as means to prevent any misalignment after the initial setup. The power and temperature stability of can be checked by using the Thorlabs laser power meter to record the output power stability over time. This can be recorded to the SD card or by using the freely available Thorlabs PC software. These measurements took place in an ambient environment of 22 °C with a atmospheric pressure of 1013 millibar.

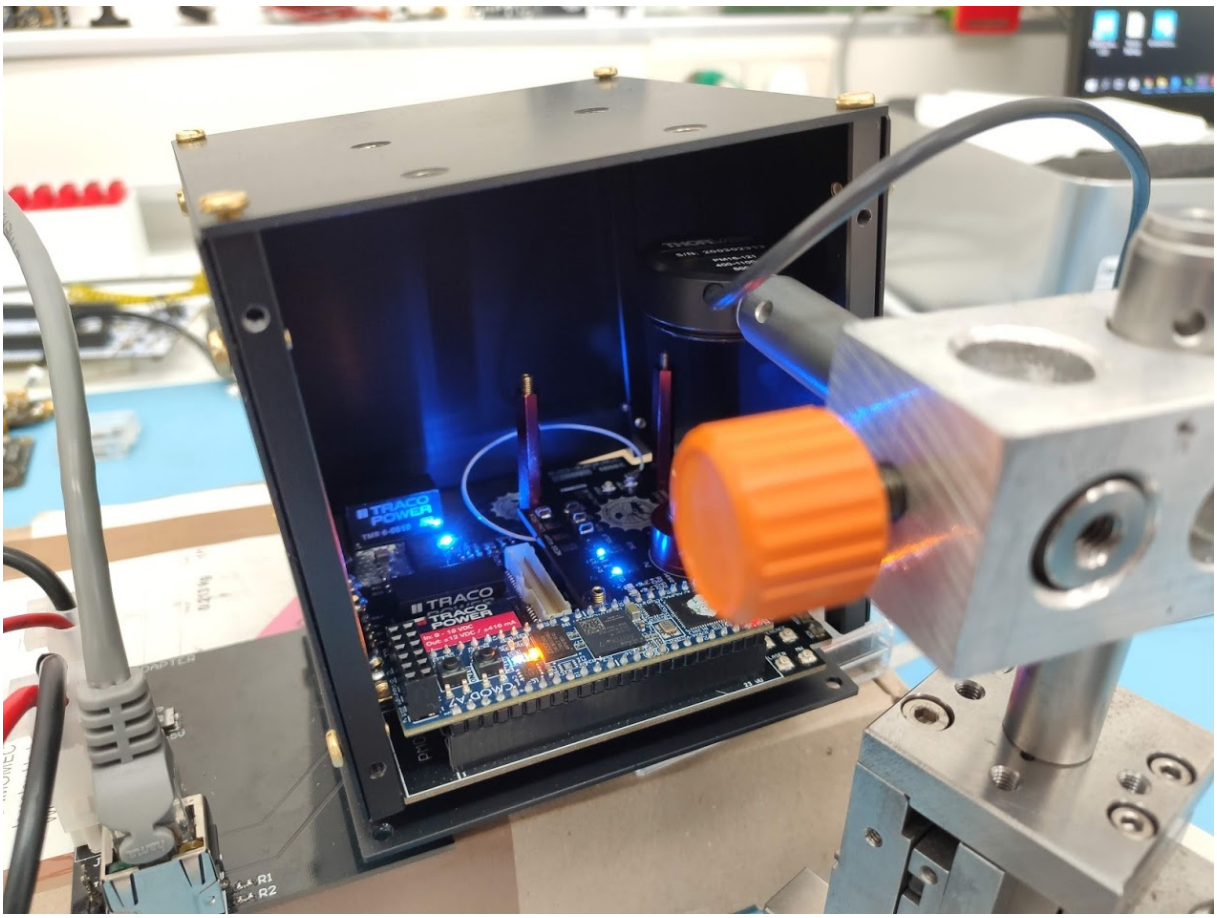

Figure 4.10: Optical laser output test setup.

4.5 System testing

Within the scope of this thesis, there also have been performed several tests on a system level. These are reported in this section. This includes testing the entire OSCAR-QUBE in a vacuum. After this, final performance tests using CW and pulsed ODMR were conducted to verify the operation of the sensor.

4.5.1 Power consumption

The power consumption of the entire experiment needs to remain below a maximum of 10 W. This is the maximum allowed power consumption for operation on the ISS ICE CUBE facility. This requires the verification of the power consumption over the entire range of laser output settings not only for the 5 V power consumption as seen in Figure 4.11 but also for the 12 V power consumption. The 7 V needed for the LD is converted from 12 V by the BA178M07FP-E2 Linear Voltage Regulator.

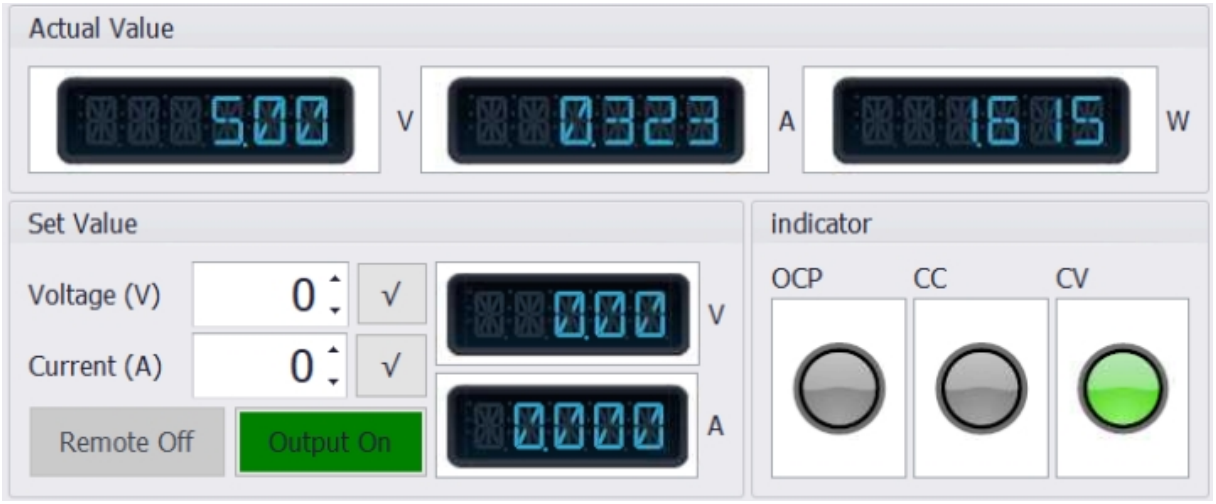

Figure 4.11: 5V power consumption on the OSCAR-QUBE.

4.5.2 Laser pulsing

Laser pulsing is used to improve the sensitivities the system is able to measure. The laser subsystem has been designed with this in mind. The FPGA delivers the pulse with the slightest possible pulse of 10 ns. This is on par with what the LD itself can handle at a rating of more than 100 MHz. The LD driver can offer pulsing up to 155 MHz. To test the pulsing, the response of the ODMR signal can be read out on the system level. Additionally, the response can be measured using an oscilloscope.

Using the the controls provided in the control software or User Home Base, laser pulsing can be configured. This can be done by setting the duration of the pulse and the window in which the measurement takes place. Further adjustments can be made to specify when in the window of measurement the laser pulse needs to be toggled. From here the system response to the pulses can be evaluated and exported for data processing.

At the pulse length of 5 μs the capacitive effect caused by the readout system can be observed already in the User Home Base as seen in Figure 4.12. On the top half, the resulting pulsed ODMR signal is seen. On the bottom, the pulse sequence is depicted with the settings in between. The ODMR signal here has already lost its square shape but still contains some resemblance to the expected original square wave.

Figure 4.12: UHB showing the pulsed ODMR response.

4.5.3 Vacuum testing

During operation in microgravity, the OSCAR-QUBE will be exposed to an environment where heat transfer by convection and conduction is reduced. Therefore testing the thermal behavior in a vacuum, where there is no convection possible due to the lack of a medium, is a good simulation. The lack of convectional cooling will lead to an increase of temperature. For more information, please refer to Section 2.6. In reality, the OSCAR-QUBE will be installed in the ICE CUBE facility in the Columbus module of the ISS, an environment with forced airflow. This solves the issue partially, but to verify that the OSCAR-QUBE can function in harsh conditions without exceeding its safety limits, it was tested in a vacuum of 0.68 millibar at 22 °C. By doing so, the convectional cooling effect is taken entirely out of the equation, leaving only conduction (except for conduction through gases) and radiation to cool the OSCAR-QUBE.

Wireless communication for the OSCAR-QUBE

For the vacuum testing, a wireless interface was set up in order to facilitate a live data feed, as the vacuum bell only allows for three leads to enter from the outside. This was done using the TP-link tl-wr702n mini router. This router was able to run parasitically on the 5 V power line going to the OSCAR-QUBE. The test setup can be seen in Figure 4.13. The communication was checked by using the packet sender to turn on and off the laser. After this, Wireshark was used to verify the packet speed of the incoming data.

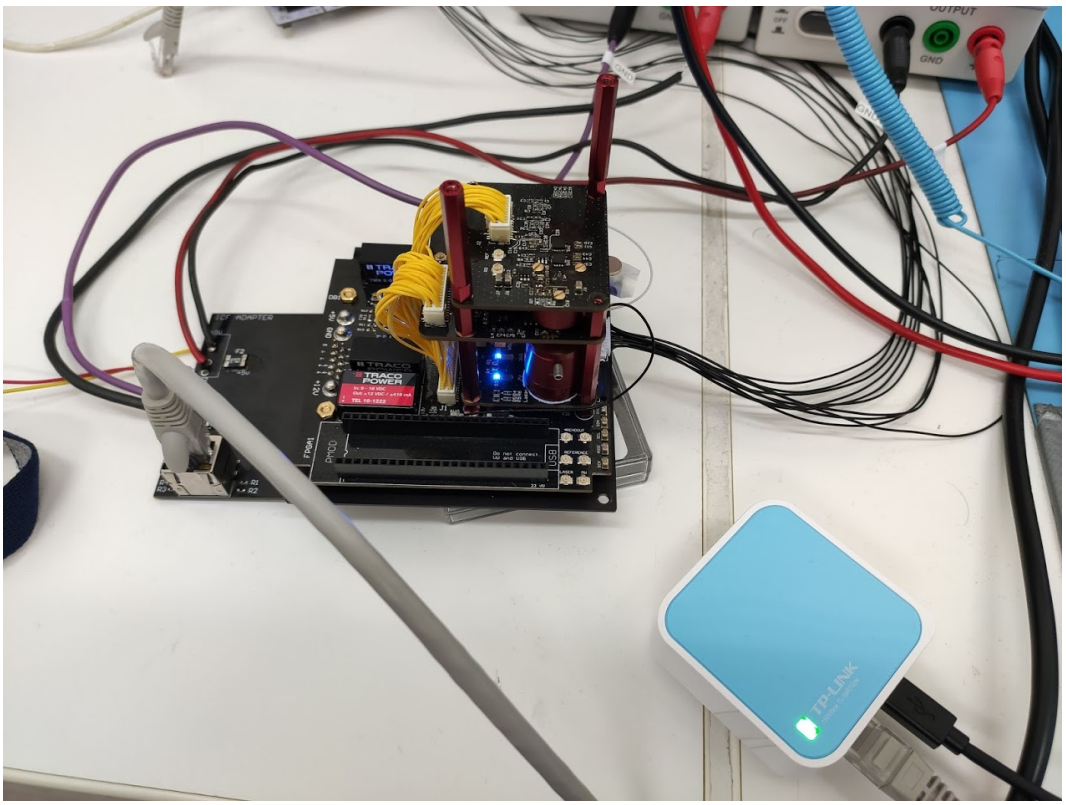

Figure 4.13: Wireless test setup.

Wireshark is used to confirm the wireless communication speed through the TP-link tl-wr702n mini router. The software is used to inspect the packet speed throughput. In Figure 4.14 the graph shows the number of packets per second in function of time.

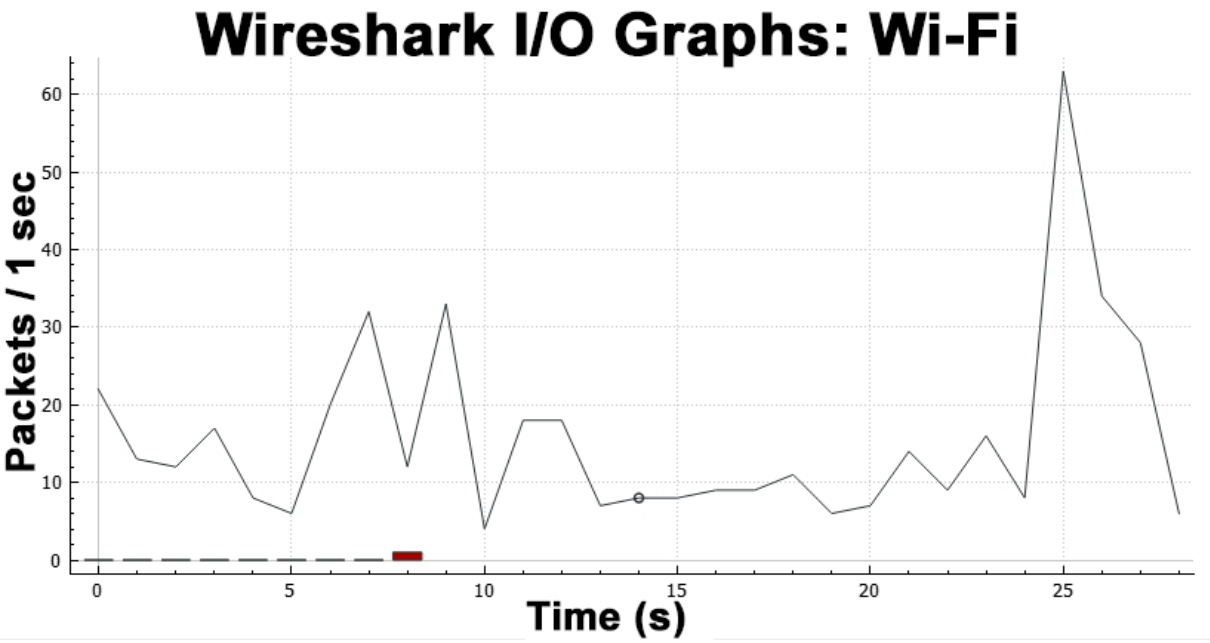

Figure 4.14: Wireshark I/O graph showing the incoming and outgoing packets.

Setup for operation in vacuum

First testing has been performed on the QUBE without the glass bell covering, acting as a baseline measurement. This can be seen in Figure 4.15. Next, the glass bell has been placed over the setup before creating a vacuum. The OSCAR-QUBE was tested in a (medium) vacuum. This was performed for three sets of laser output powers being ∼13 mW (R0200), ∼33 mW (R0100), and ∼50 mW (R0000).

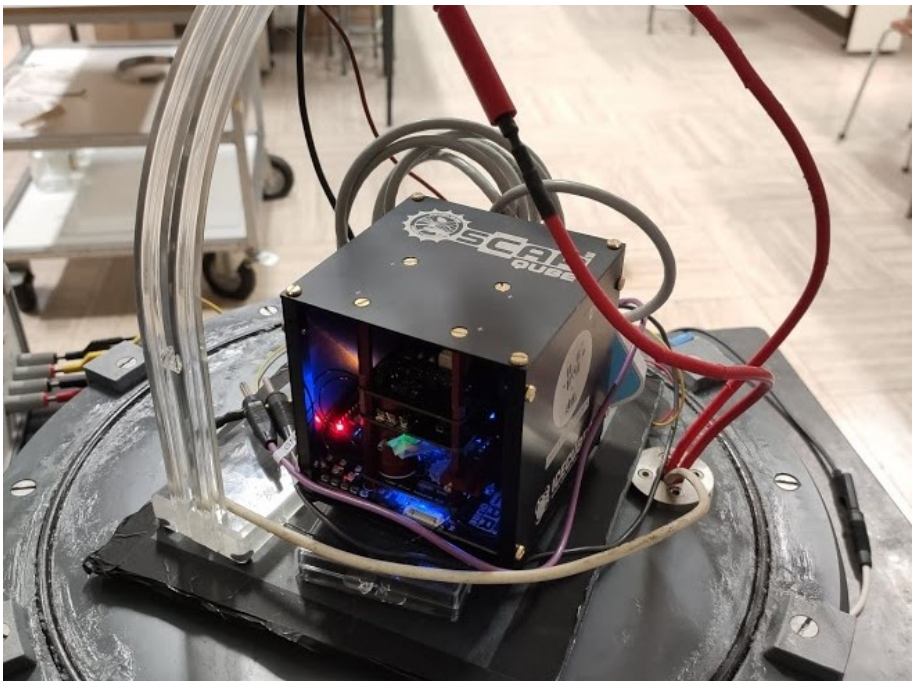

Figure 4.15: OSCAR-QUBE in open setup.

Data analyses during operation

During these tests, the data will be streamed via the wireless solution to a computer. This enables a live dashboard to control the OSCAR-QUBE and a monitoring dashboard to check the status of the OSCAR-QUBE. In Figure 4.16 the ODMR signal is visible, while in Figure 4.17 the temperature for the laser (green) and the power board (red) can be seen on the top, reference systems are also included to show acceleration, magnetic fields, and gyroscope information. Additionally, the data is stored in order to see what values show over time. After the testing, the data is processed and analyzed. For this, graphs of the temperature in function of time and mean ODMR voltage are used.

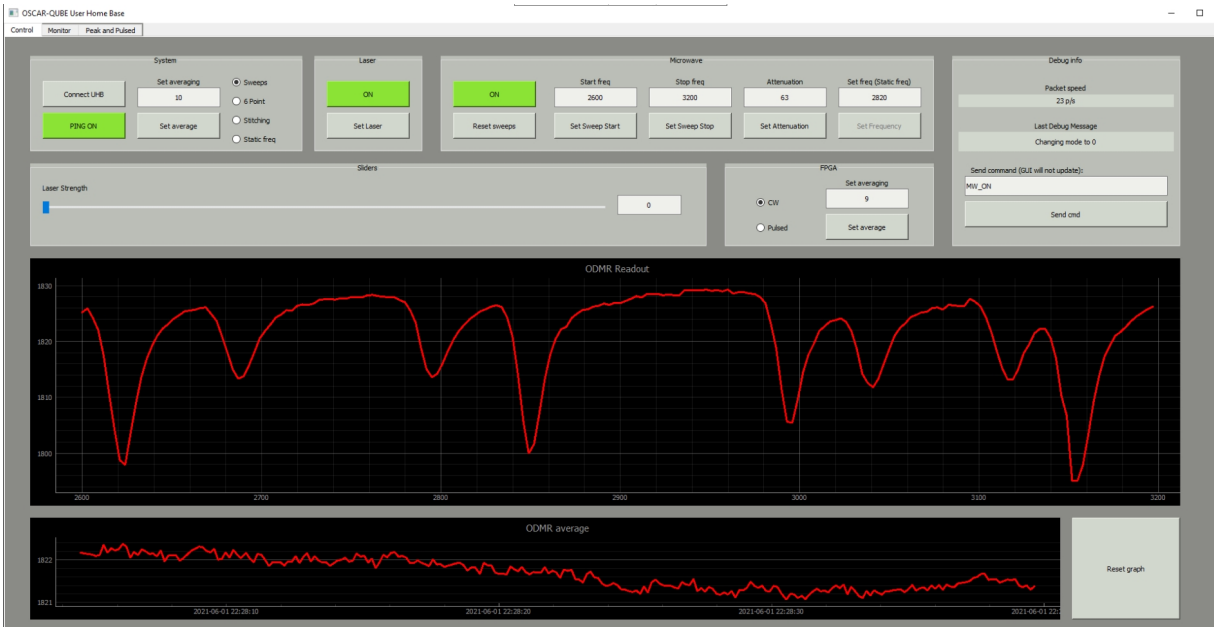

Figure 4.16: OSCAR-QUBE User Home Base control dashboard.

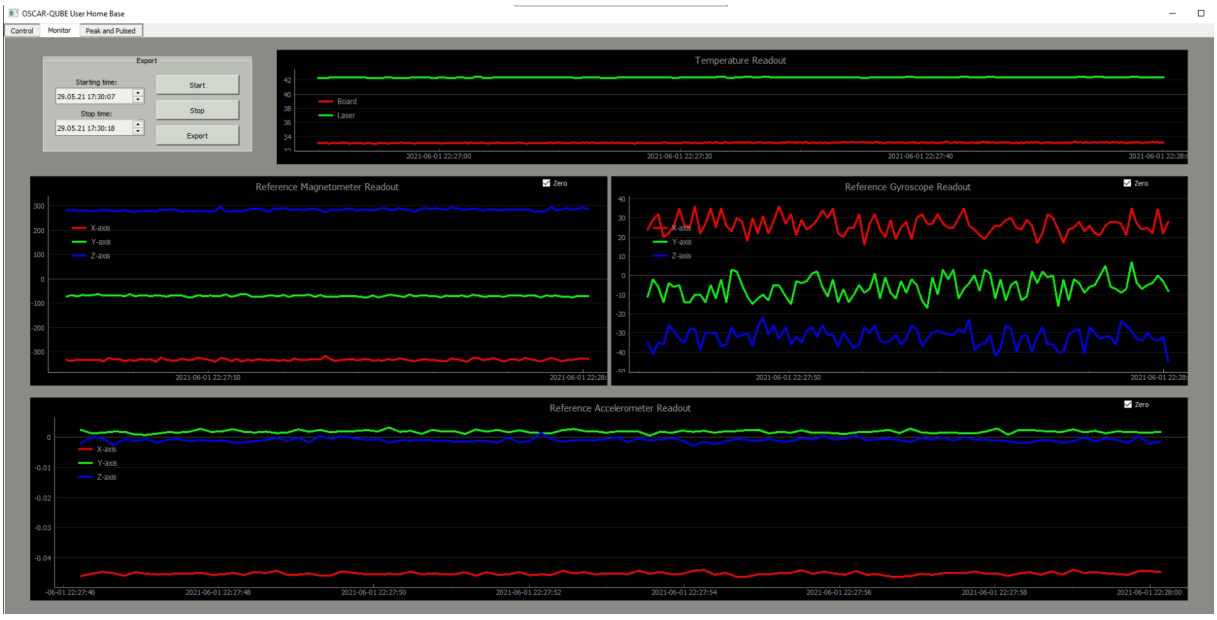

Figure 4.17: OSCAR-QUBE User Home Base monitor dashboard.

Thermal images

The thermal performance of the OSCAR-QUBE is first tested in non-vacuum by means of performing measurements at the full optical laser output power of ∼50 mW. After the temperatures stabilize, a FLIR thermal imaging camera is used to provide an insight into the heat distribution throughout the OSCAR-QUBE and the thermals on the laser housing itself. After the vacuum testing was concluded, additional images were taken in order to verify the readings obtained from the OSCAR-QUBE itself. Additionally, this allows the verification of the outside shell temperature. The temperatures reached with this test will be the absolute maximum temperatures as there is no cooling effect other than dissipation by conduction and radiation.

Figure 4.18: Glass acting like a mirror for infrared radiation.

4.5.4 Final performance testing

After the stress testing, a test is performed with the OSCAR-QUBE running continuously in a lab environment that is not temperature controlled. The temperature at the time was stable enough to perform this test. The system was set up to reach a stable operation based on the temperature. After this, the OSCAR-QUBE started to perform measurements for more than two hours.

ODMR and PDMR

For ODMR, the use of CW ODMR and pulsed ODMR is verified. Furthermore, the minimal laser power needed to obtain an ODMR signal is checked. The quality of the ODMR signal is checked for CW and pulsed ODMR. Room for improvements upon these signals can be found by using averaging.

The OSCAR-QUBE is PDMR ready. However, the diamond samples available to us are not geared towards the use of PDMR. The quality of the PDMR measurements is not up to par. Nonetheless, it is possible to get measurements from the PDMR signal.

Chapter 5

Results and discussion

In this chapter, the results of testing the subsystem can be seen. This for tests done both on the system and on a subsystem level. The system-level tests directly correlate to the performance of the entire OSCAR-QUBE. The subsystem level tests relate to the tests done to verify the working of the subsystem itself.

5.1 Subsystem test results

5.1.1 Laser driver evaluation kit

In Figure 5.1, the iC Haus laser driver evaluation kit can be seen. During the initial testing, an LED was used to be sure the LD itself would not be damaged unnecessarily. Testing was performed for two configurations, CW operation, and pulsed operation. Both of which proved to be possible, as testing with a function generator implicated.

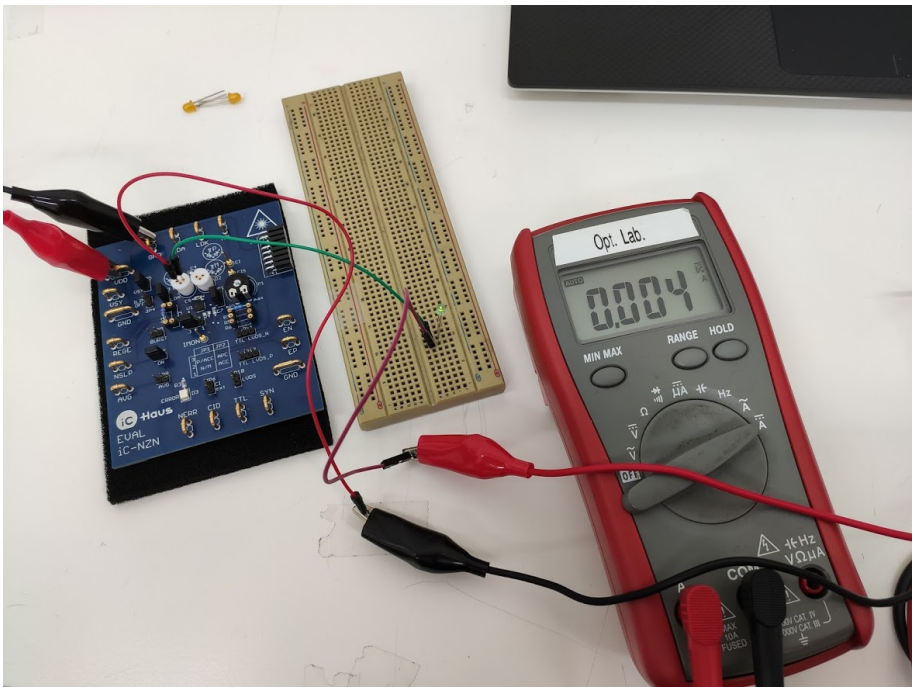

Figure 5.1: Testing of the laser driver evaluation kit using an LED.

5.1.2 Digital potentiometer

The linearity of the digital potentiometer was verified. This was done by measuring the resistance over the wiper and low pin of the MAX5483 over the entire range (0-1023) using steps of 10. The result, as seen in Figure 5.2, shows the linear nature of the MAX5483 digital potentiometer over the entire range.

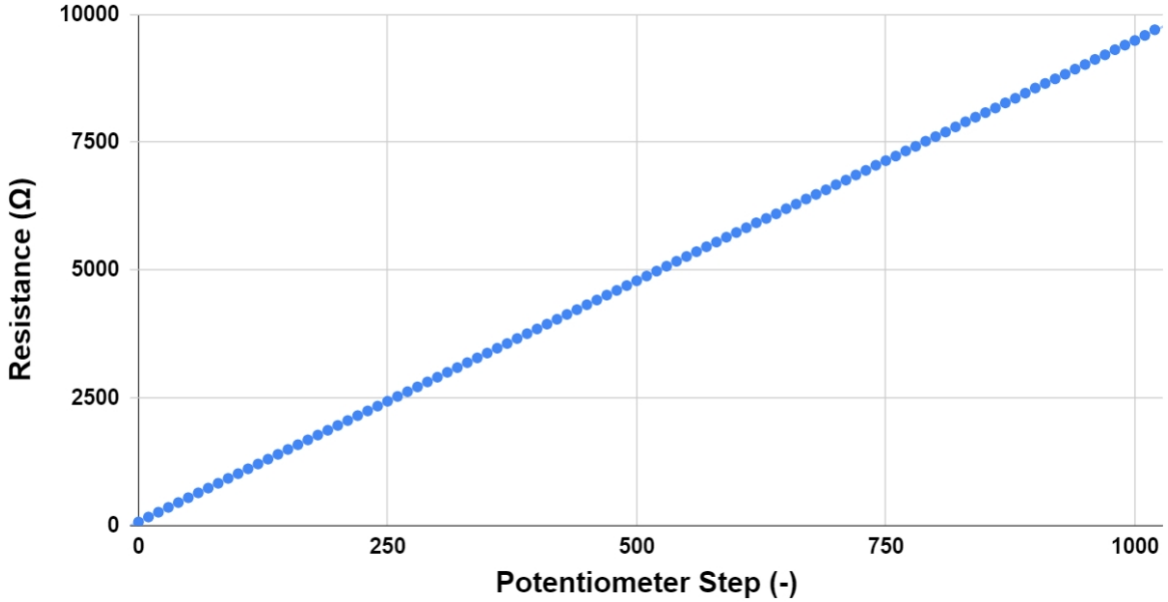

Figure 5.2: Resistance in function of potentiometer setting

5.1.3 PCB

For the laser board the initial work was to solder the required components onto the PCB. This was done partially by hand, where possible the PCB oven was used to solder the components. The LD and temperature sensor are through hole components wich ware soldered into place after all other components had been placed.

The laser board is depicted in Figure 5.3. Here is seen that testing and debugging has been made easier by providing testing points for every signal of importance on the PCB. The LD housing seen here is not yet anodized to its final red anodized coating. The via stitching is clearly visible on the right of the image under this angle. It can also be noted that the bottom left standoff drill hole is not coated nor connected to a net. The other standoff drill holes are connected to ground. This drill hole, and the corresponding standoff is close to the LD housing which itself is connected to the 7 V net. To minimize the risk of creating a short circuit this drill hole was not connected to a net, and not coated.

In general, the testing consisted of verifying that the voltages received are correct. The procedure is to use a multimeter to measure the voltage between the ground and the 3V3 and 7V test pads incorporated into the PCB design. The result is that the voltages measured on the test pads are 3.287 V and 7.05 V, respectively, as can be seen in Figure 5.4.

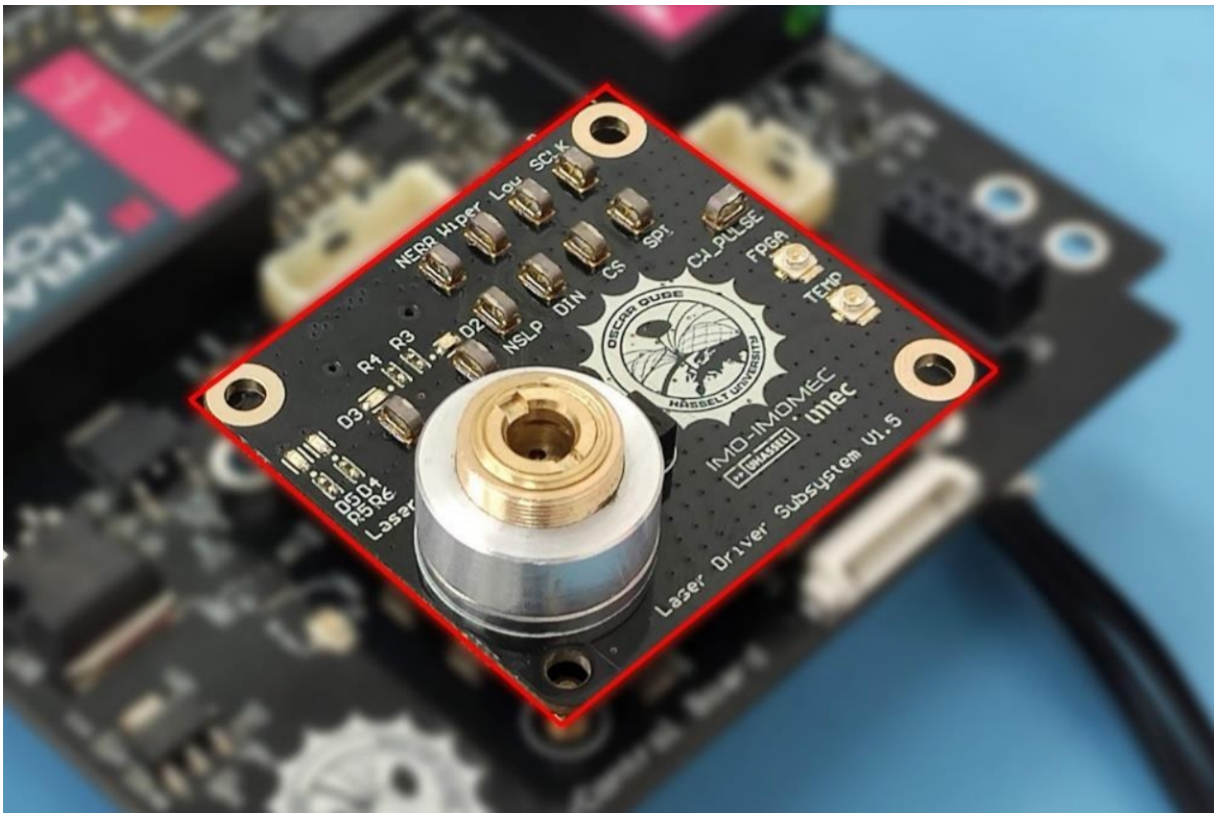

Figure 5.3: Laser subsystem (within red highlight) on top of Power Board

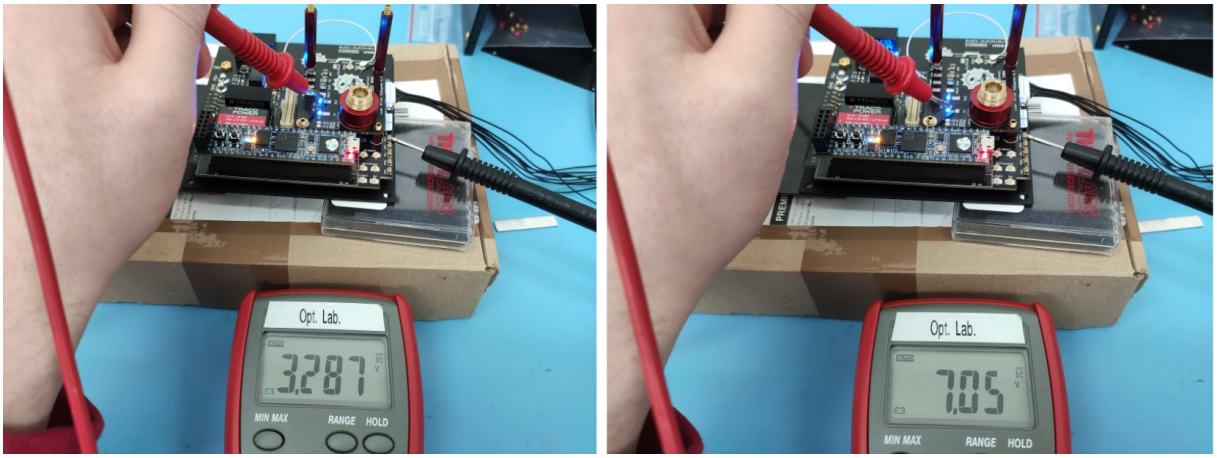

Figure 5.4: Voltages measured on the Laser Board

5.1.4 Driver and diode

Now the communication channels can be checked. This relates to the SPI communication with the programmable resistor. This is done by using packet sender first to initialize the system, using the 'START' command while verifying it using the analog discovery as seen in Figure 5.5. This is then followed by setting the resistance using the appropriate 'LASER_SETRXXXX' command. XXXX is a value ranging from 0000 to 1023, corresponding with the 10-bit levels of the digital potentiometer.

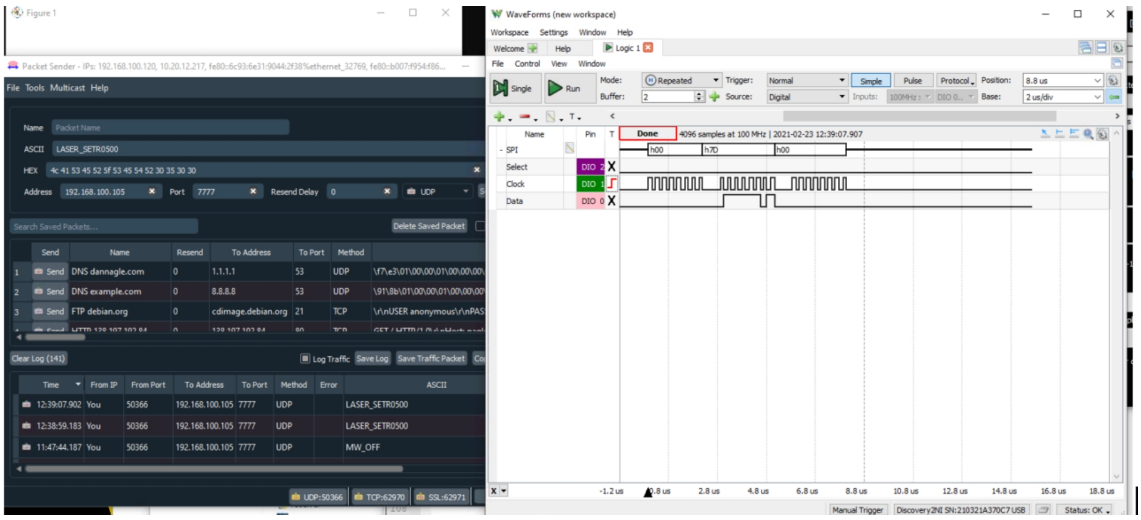

Figure 5.5: Screenshot verifying the communication using the analog discovery and packet sender

After this, the system response to these commands can be checked. The laser can be turned on with 'LASER_ON'. Turning the laser off can be done using the 'LASER_OFF' command. A lower resistance setting needs to be set to increase the laser output power, such as can be done using the 'LASER_SETR0200' command. These steps can be seen in Figure 5.6.

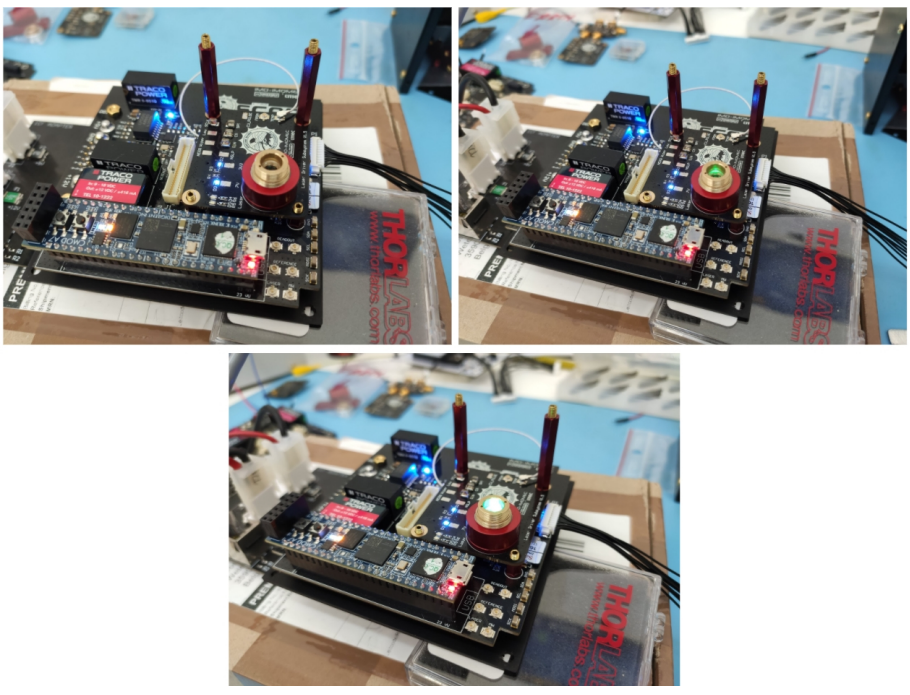

Figure 5.6: On the left laser is off, on the right laser is on. Bottom higher power setting.

By setting a range of different potentiometer values and measuring the response of the output optical power of the laser, the power output in function of resistance was recorded. This is can be seen in Figure 5.7. Initially, there is some power needed to get going, resulting in a slow increase in power. This is explained by the threshold current needed for the LD itself. From a potentiometer setting of 200 and lower, a linear behavior can be observed. At a setting of 0, the power output reaches 49.5 mW out of the maximum of 50 mW stated in the datasheet of the LD. This also shows that the current limit resistor selected for the laser driver was correct. The temperatures at these potentiometer settings can be seen in Figure 5.8.

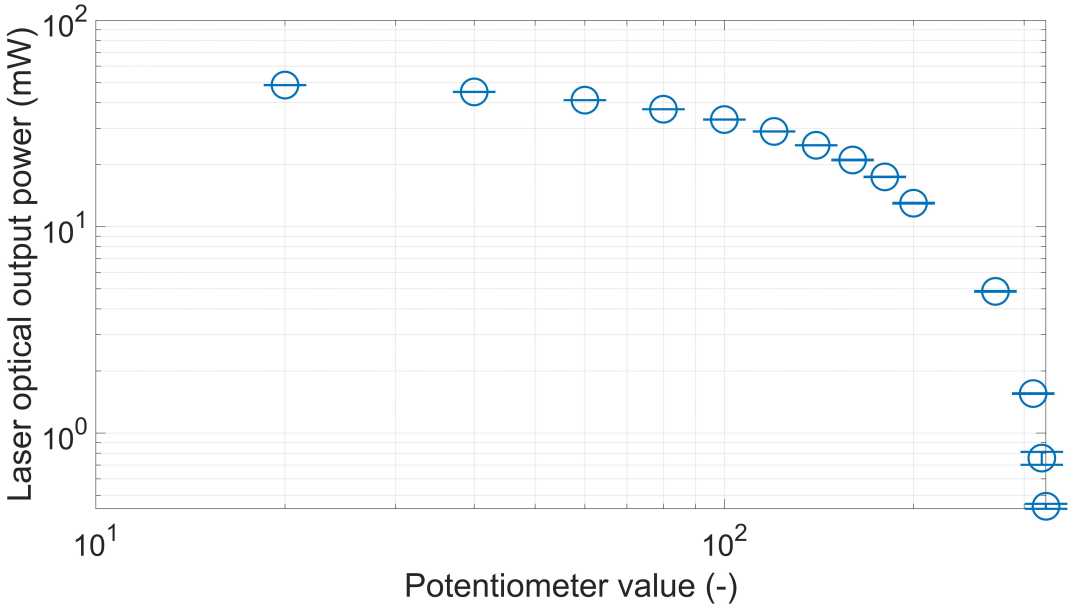

Figure 5.7: Optical laser output power in relation to the potentiometer setting. Note that, due to the nature of the Logarithmic scale the laser power value corresponding with potentiometer value 0 is not visible.

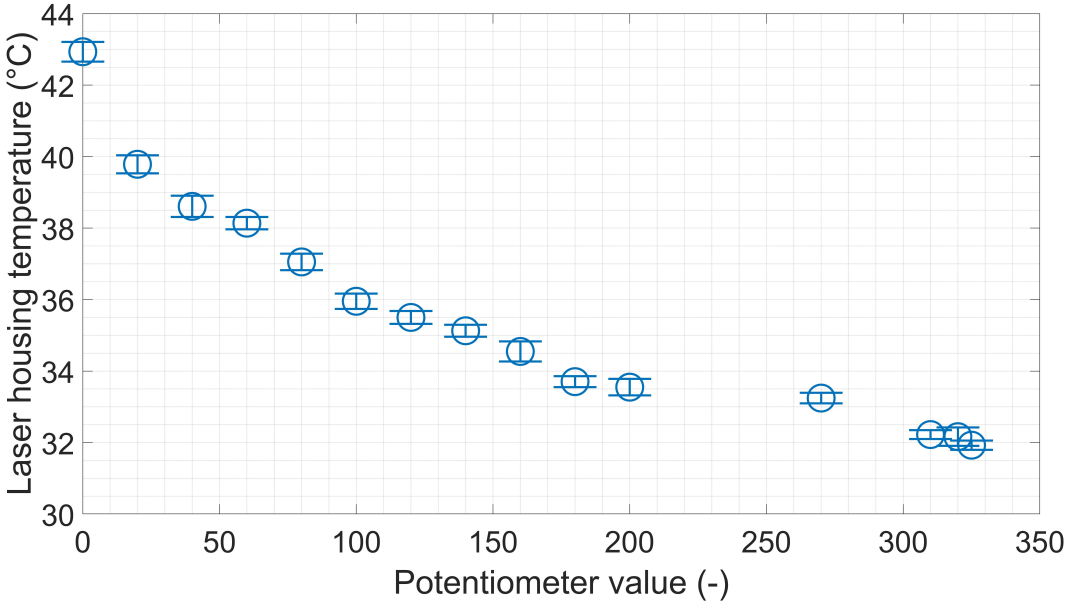

Figure 5.8: Temperature in relation to the potentiometer setting.

The values from the graphs on the previous page are presented in Table 5.1. These measurements took place in an ambient environment of 22 °C with a atmospheric pressure of 1013 millibar. The standard deviations are also shown in the percentage of the corresponding value. The absolute largest standard deviation for the laser output power of 20.97 mW and is 0.074 mW at a potentiometer setting of 160. This corresponds to 0.353% of 20.97 mW. In percentage terms, the largest deviation can be found at a potentiometer setting of 200. Here the output power is 12.95 mW, and the standard deviation is 0.058 mW, equal to 0.448%. For the temperature, similar observations are made. The absolute largest standard deviation is 0.298 °C, at a potentiometer setting of 20, and the largest standard deviation in percentage terms can be found at potentiometer setting 160 at 0.813%.

This concludes that the most significant standard deviation on the output power in percentage terms is 0.5%. For temperature, the most significant temperature deviation is 0.8%. **Note**, the values above a potentiometer setting of 300 are not included in this mindset. These values result in optical laser output powers that are not used to collect any data. Therefore, their performance is not of interest in the scope of this thesis.

Table 5.1: Potentiometer settings with corresponding laser output values. In bold the maximum values for the standard deviations are shown. For improved readability please refer to Appendix A

Potentiometer setting (-)	0	20	40	60	80	100	120	140	160	180	200	270		310	320	325
Laser Output Power (mW)	49.54	48.66	45.02	41.06	37.11	33.05	28.94	24.77	20.97	17.45	12.95	4.84		1.55	0.79	0.45
Standard deviation (mW)	0.027	0.024	0.016	0.009	0.008	0.014	0.026	0.028	**0.074**	0.031	0.058	0.022		0.006	0.055	0.012
Standard deviation (%)	0.055	0.049	0.036	0.022	0.021	0.042	0.089	0.113	0.353	0.178	**0.448**	0.455		0.387	6.962	2.667
Laser Temperature (°C)	42.93	39.79	38.61	38.14	37.05	35.95	35.50	35.13	34.55	33.70	33.55	33.24		32.22	32.17	31.92
Standard deviation (°C)	0.276	0.251	**0.298**	0.173	0.229	0.215	0.179	0.169	0.281	0.154	0.229	0.148		0.123	0.256	0.131
Standard deviation (%)	0.641	0.631	0.772	0.453	0.618	0.598	0.504	0.481	**0.813**	0.457	0.683	0.445		0.382	0.796	0.410

Lastly, a TTL signal was applied to the Laser TTL port by using a square wave signal generator. At low frequencies, the laser visibly blinked in response to the applied frequency. At a higher frequency, the intensity detected on the photodiode halved, which corresponded to the expectations for the 50% duty cycle that was set. After this, a pulse sequence was programmed to the FPGA that creates laser pulses of 400 ns. When checking these pulses using the analog discovery, as seen in Figure 5.9 it shows that the laser subsystem is able to create laser pulses with a duration of 400 ns.

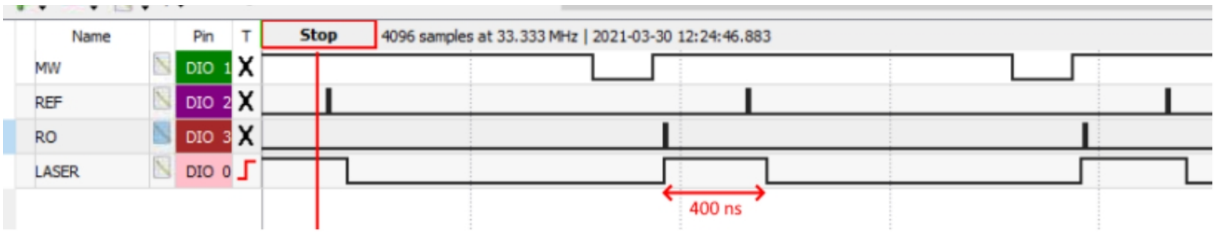

Figure 5.9: The Analog Discovery shows a laser pulse length of 400 ns.

Optical and thermal Stability

By combining the temperature sensor data and the output power data of measurement, a graph as seen in Figure 5.10 emerges. This graph shows the course temperature and output power take over a period of more than 20 minutes. During this time, the temperature is situated between 37.6 °C and 38.6 °C, as shown on the left. The laser output power measured by the PM100D power meter and the S121 power head is situated in the range of 41.03 mW to 41.07 mW shown on the right. Here it is seen that the variation of laser output power for this entire graph is smaller than 0.04 mW. However, this is not enough to prove optical and thermal stability on its own. The data needs to be processed to show where the most values are situated.

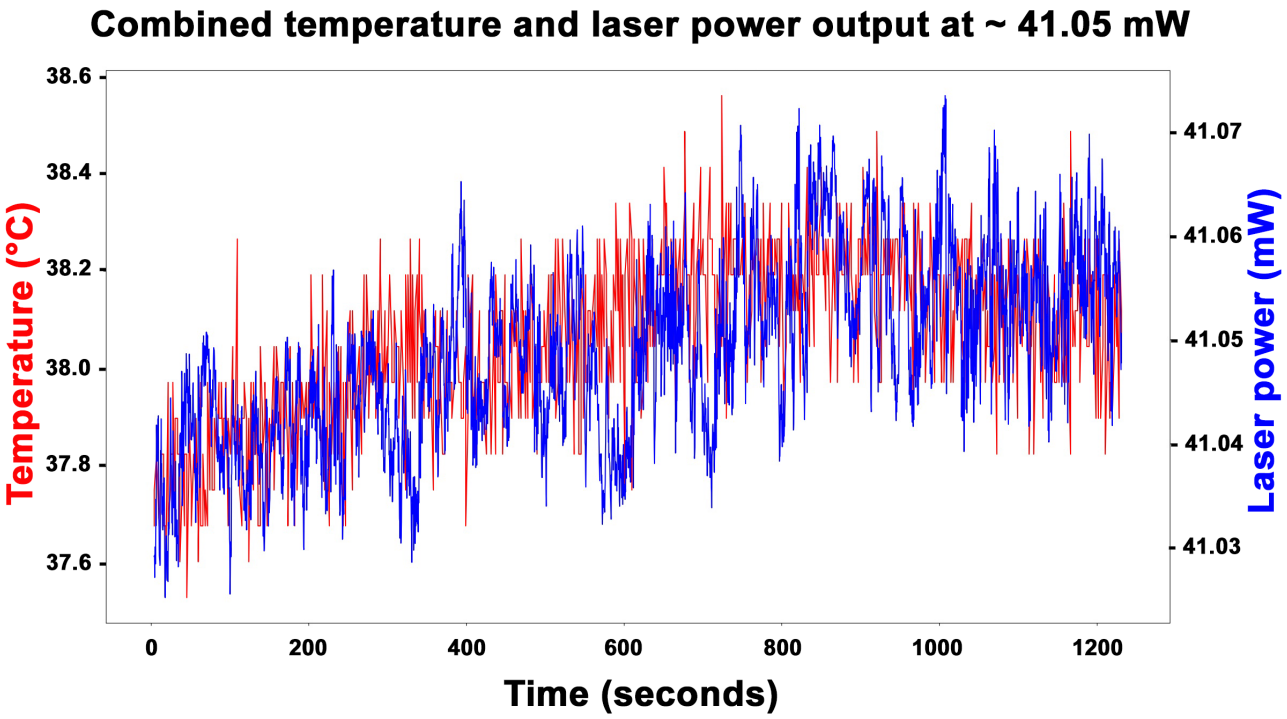

Figure 5.10: Laser output power and temperature over time at R0060

The data collected during the stability measurements are now presented to show the spread of the samples themselves. By using bar plots, the amount of samples is presented for each range of laser power values measured using the Thorlabs PM100D and S121 setup. This is done for three main settings to cover the entire range of the laser. Both optical and thermal stability results are shown for low, medium, and high laser output powers on the following pages.

For the low output power the entire range goes from 1.54 mW to 1.57 mW, as seen in Figure 5.11 while the temperature ranges from 31.78 °C to 32.66°C as Figure 5.12 indicates. What is seen here amounts to the amount of samples found at the corresponding ranges on the X-axis. For the laser power graph similarities with a Gaussian function can be recognized showing its stability, as most values are in the center of the range. The temperature graph is more spread out, yet most of the values are still contained in the center of the range. This stable behavior is desired for the OSCAR-QUBE.

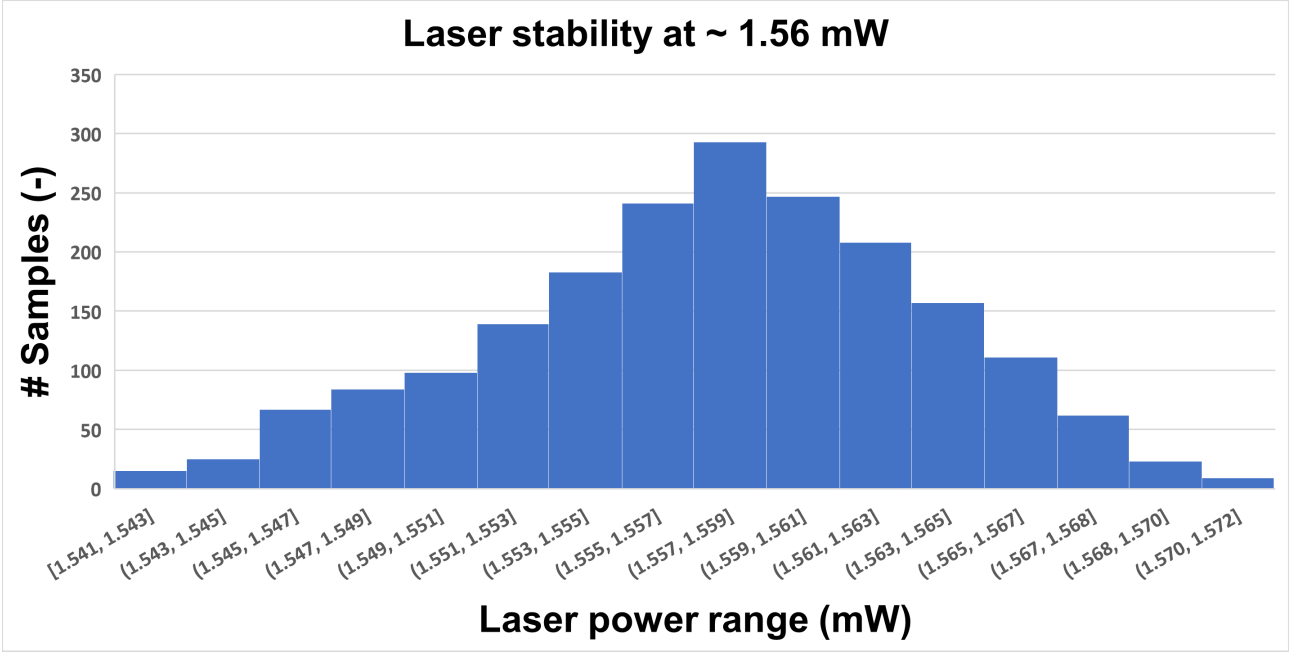

Figure 5.11: Testing the laser output power stability at potentiometer setting R0310.

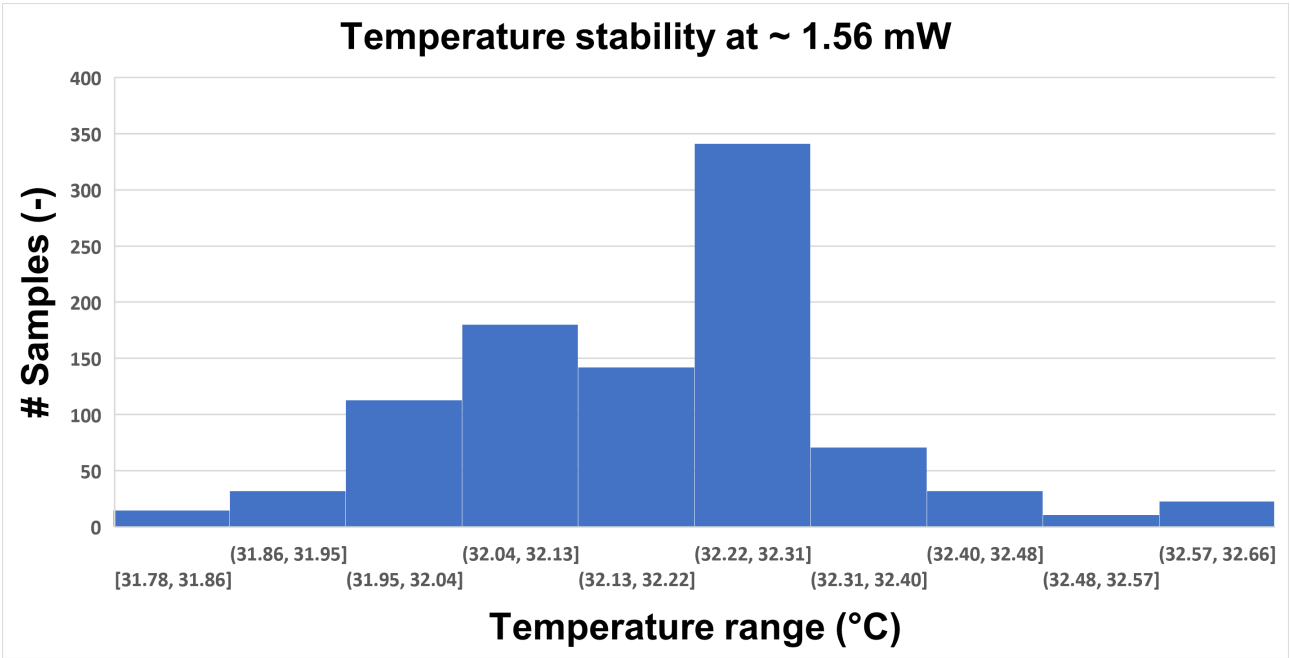

Figure 5.12: Testing the temperature stability at potentiometer setting R0310.

Continuing with the medium laser power setting at approximately 17.45 mW, Figure 5.13 and 5.14 should be observed. Here the output power ranges from 17.42 mW to 17.47 mW. The temperature at the low-end amount to 33.33 °C, while on the upper end, it is 34.06°C. For the laser power stability a shift from lower to higher powers is seen. This can be from slight cooling during the start of the measurement, leasing the output power to increase. The Gaussian function here is also recognizable with a clear center. For the temperature, the limited resolution of the sensor leads to larger bar sections. Nonetheless, the Gaussian function holds true. The vast majority of temperatures is situated in the center of the range.

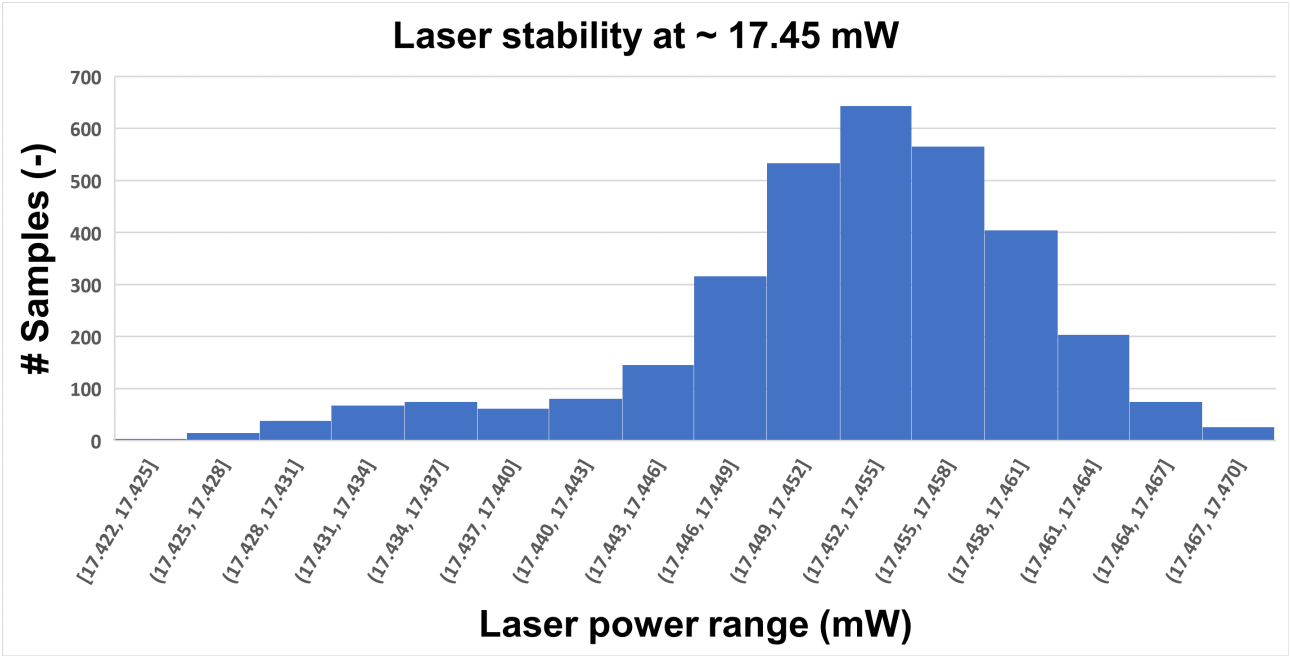

Figure 5.13: Testing the laser output power stability at potentiometer setting R0180.

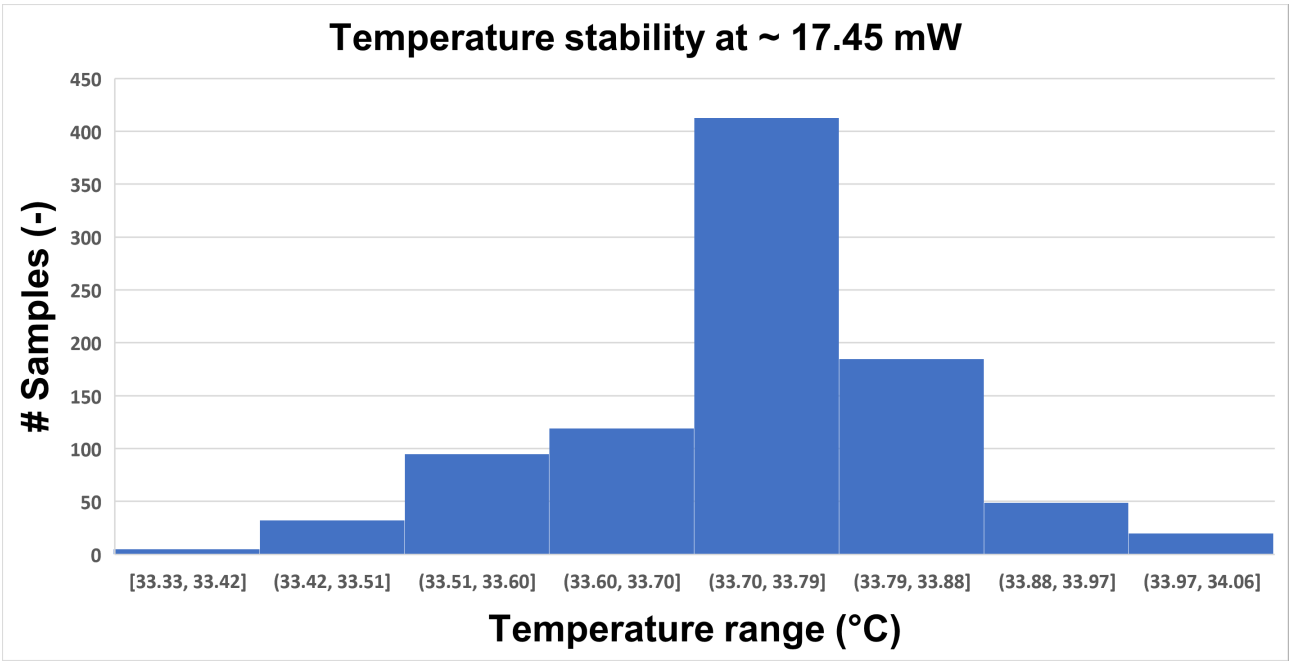

Figure 5.14: Testing the temperature stability at potentiometer setting R0180.

Finally, at the high laser output power of roughly 41.05 mW, Figure 5.15 shows an output power range going from 41.02 to 41.07 mW. The accompanying Figure 5.16 shows temperature ranges from 37.53 °C to 38.56 °C. The trend of the Gaussian curve is continued in the high output power stability test. The number of samples rises quickly to reach a maximum in the middle of the range, after which a fast decline is observed. For this test, the temperature stability graph shows the Gaussian trend clearly, indicating the stability of the subsystem.

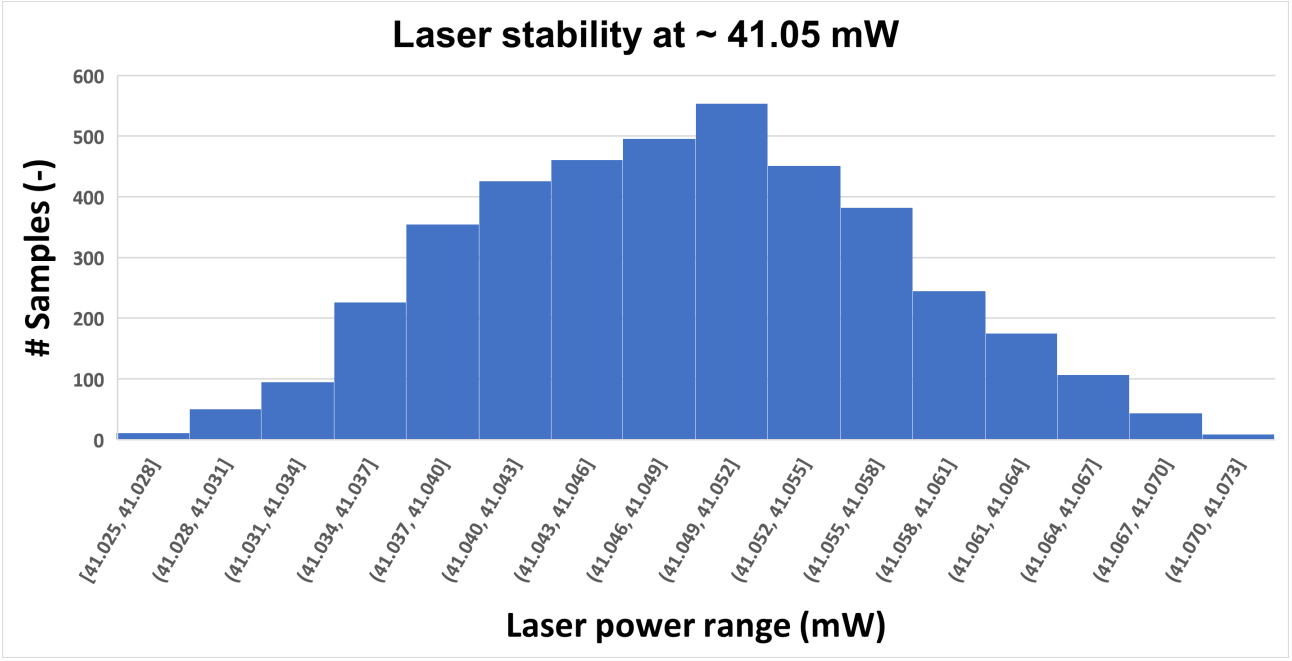

Figure 5.15: Testing the laser output power stability at potentiometer setting R0060.

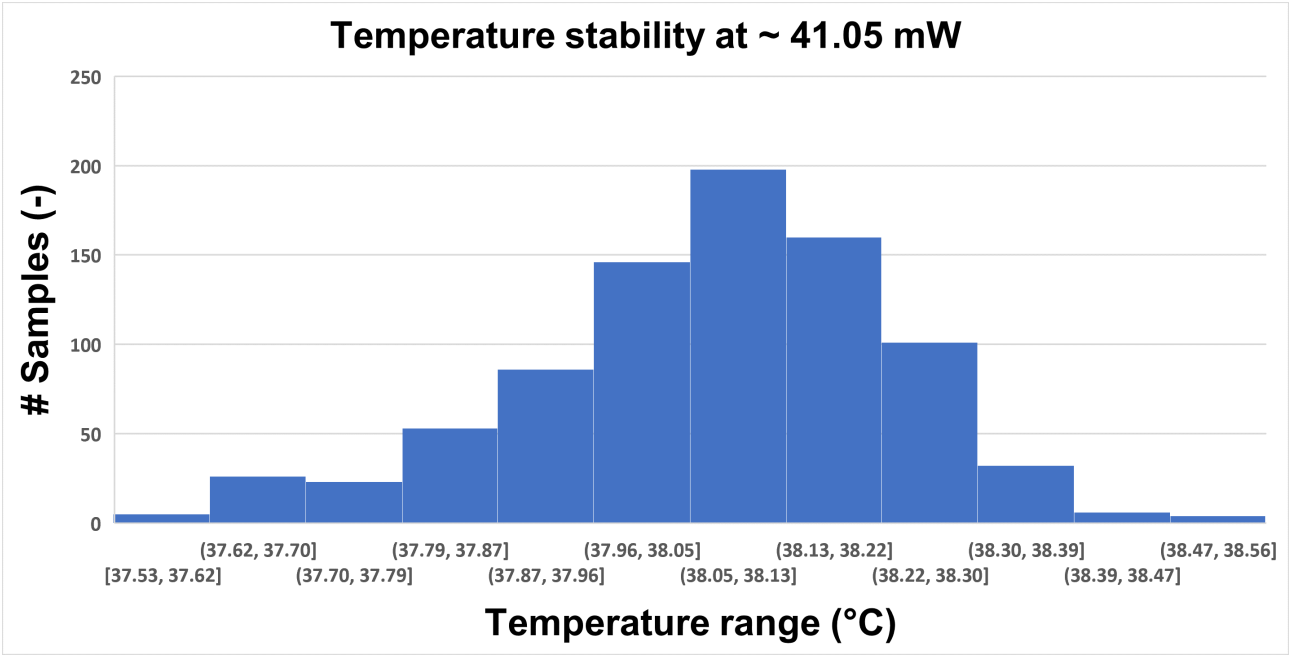

Figure 5.16: Testing the temperature stability at potentiometer setting R0060.

5.2 System test results

5.2.1 Power consumption

The current consumption of the entire system on the 12 V line reaches a peak of 400 mA when the laser is turned to full power. With the laser turned off, this is only 250 mA. The LD draws power from the 12 V line via a 12 V to 7 V Linear Voltage Regulator (BA178M07FP-E2). The current draw for both the system and the LD over a range of potentiometer values can be seen in Figure 5.17. When viewing the power draw, as seen in Figure 5.18, the entire system power draw on the 12 V line remains below 5 W at 4.79 W. However, the LD power draw is situated at 1.79 W, which is 0.74 W to over the diode limit of 1.05 W.

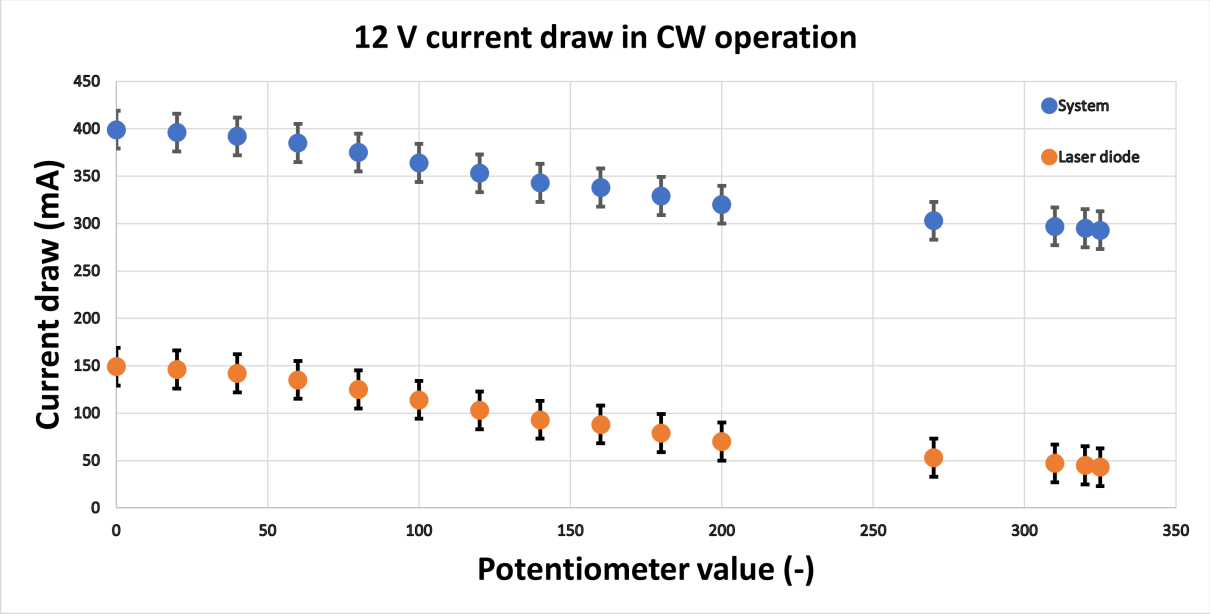

Figure 5.17: 12 V current draw for Laser diode and System in CW operation.

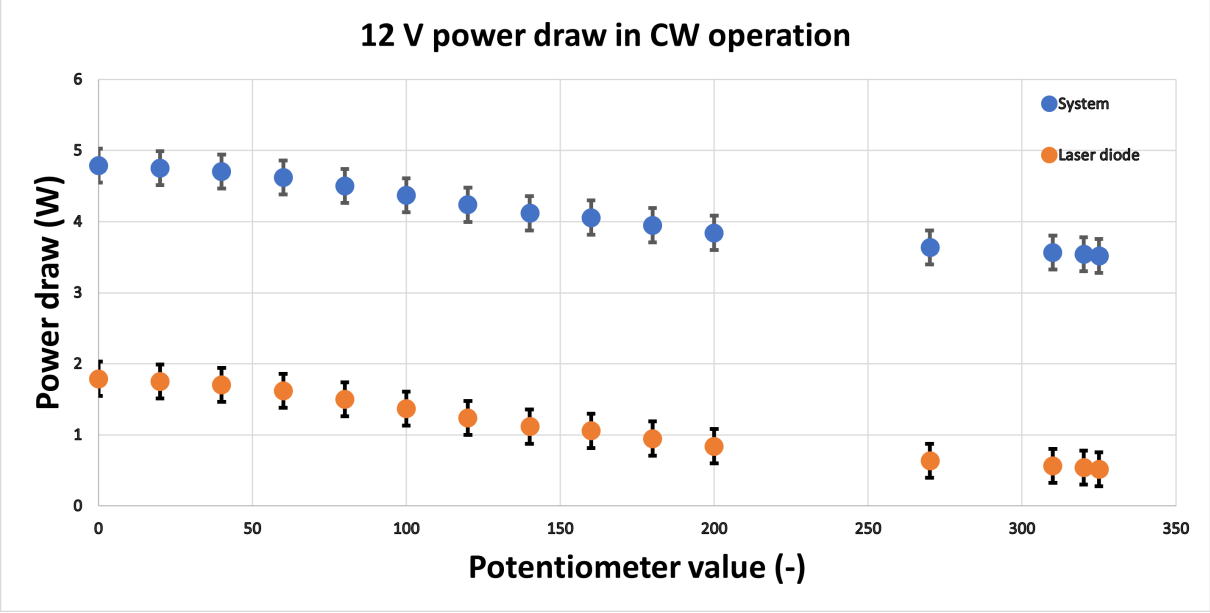

Figure 5.18: 12 V power draw for Laser diode and System in CW operation.

This 1.8 W usage is a distorted view of the situation. The Voltage regulator used in this case has a conversion efficiency of only 58% as can be seen in Equation 5.1 [51]. The current flow going to the diode itself is limited to 150 mA at a voltage of 7 V. Therefore, the LD itself can only consume 1050 mW of power. This power consumption is 58% of the 1.8 W depicted by the power draw.

$$\eta = \frac{V_{out}}{V_{in}} = \frac{7}{12} = 0.5833 \text{ [51]} \tag{5.1}$$

5.2.2 Pulse performance

The laser driver offers a maximum frequency of 155 MHz. According to the datasheets, the minimum pulse length that the FPGA can provide is ten ns long, and the LD itself features a modulation frequency of at least 100 MHz. This leads to the primary limitation being posed by the diode and the FPGA at 10 ns. Secondary limitations can be caused by the entire chain of the readout subsystem.

By using the Rhode & Schwarz RTC1002 oscilloscope to measure the system response to the same 5 μs pulse results in the response seen in Figure 5.19. Here the capacitive charging and discharging are much more apparent. By looking closer at the oscilloscope's time base, it is noticed that the applied 5 μs laser pulse results in a longer response pulse of approximately 6 μs. This indicates there is an inevitable system delay. In this case, this delay should be more noticeable when shorter pulses are applied.

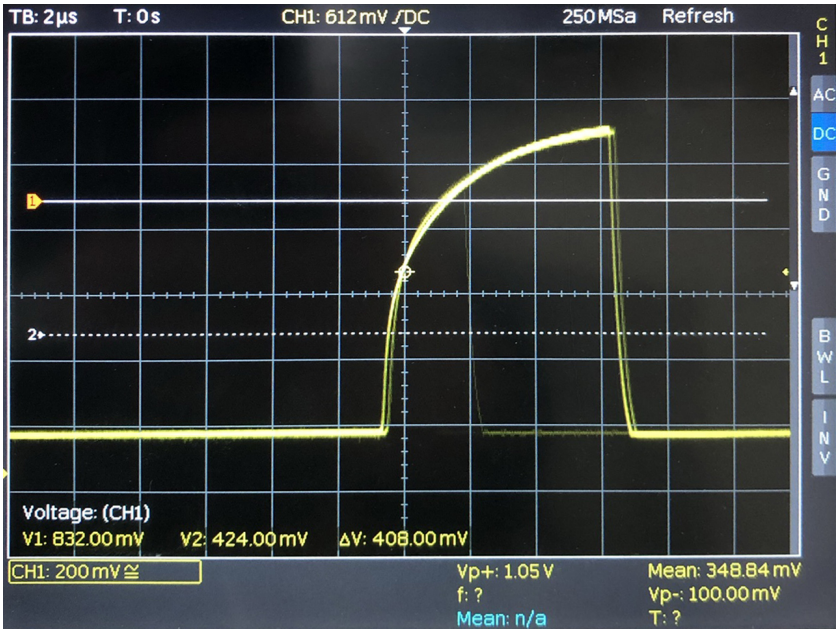

Figure 5.19: Oscilloscope showing the 5 μs pulse.

When lowering the pulse width to 100 ns, ten times the theoretical limit, the previous results are confirmed. In Figure 5.20 the system response to a 100 ns pulse can be seen. In Figure 5.21, this same pulse is seen but when employing averaging over 1024 samples. Here the square wave has been completely removed by the integrating effect the readout system has on the input pulse. Most noticeably, here is that the oscilloscope time base indicates the pulse duration to be about 150 ns, 50% longer than the 100 ns pulse that is applied. This indicates the presence of a system delay between the application of the pulse and the readout itself.

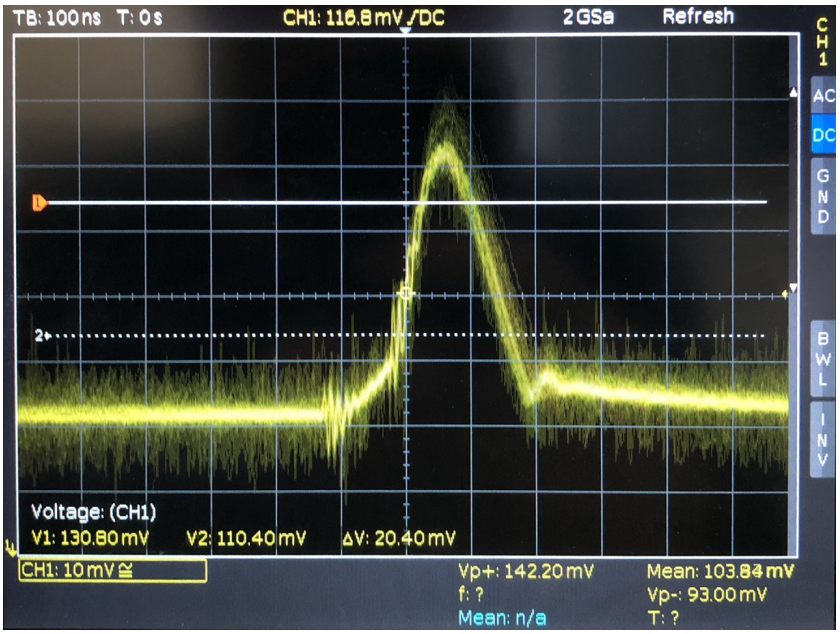

Figure 5.20: Oscilloscope showing the 100 ns pulse.

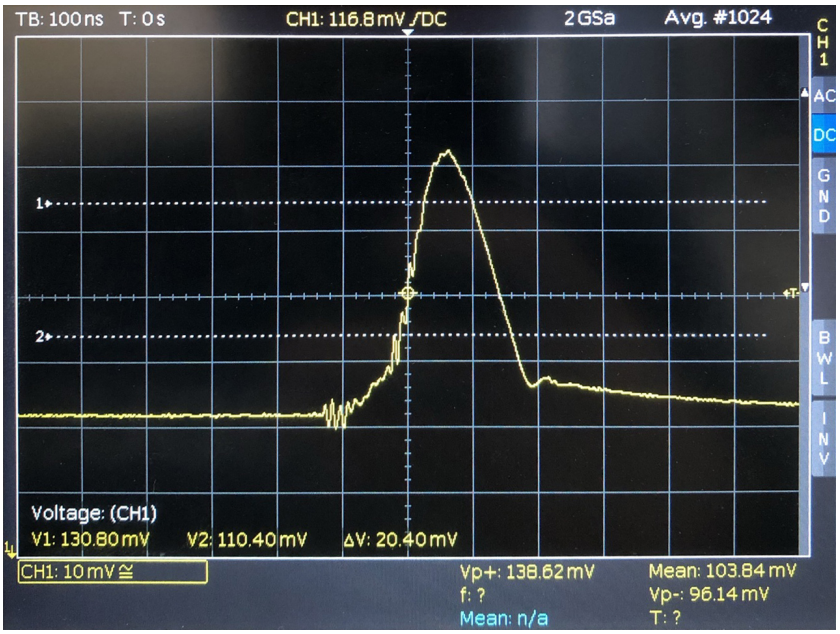

Figure 5.21: Oscilloscope showing the averaged 100 ns pulse.

By observing the capacitive effects first in the microsecond range and in these nanosecond range measurements and an elongated response, it is clear that there are some secondary limitations posed by the readout circuitry and possibly the NV centers as well. The NV centers feature a particular activation time, and the amplification of the applied pulse happening after the photodiode by the readout subsystem acts as an integrator. The readout system having this integrating effect is causing the square wave of the pulses to be rounded. Ultimately a triangle shape is seen.

5.2.3 Vacuum testing

Before operating in a vacuum, a baseline is set by testing the OSCAR-QUBE thermal performance in non-vacuum by performing measurements at full optical laser output power. The highest temperature on the laser, according to the readout, reaches 40°C. According to the FLIR camera used, the hottest point was 42.7°C. This difference can be accounted for by the placement of the temperature sensor and by the laser housing acting as a heat spreader. The outside of the OSCAR-QUBE reaches only 28°C. Figure 5.22 first shows a regular image on top with a FLIR image on the bottom with a similar perspective. **Note** that, in the top left image the OSCAR-QUBE is placed under the glass bell and the corresponding FLIR image bellow was taken before the glass bell was placed. This image is placed for illustrative purposes.

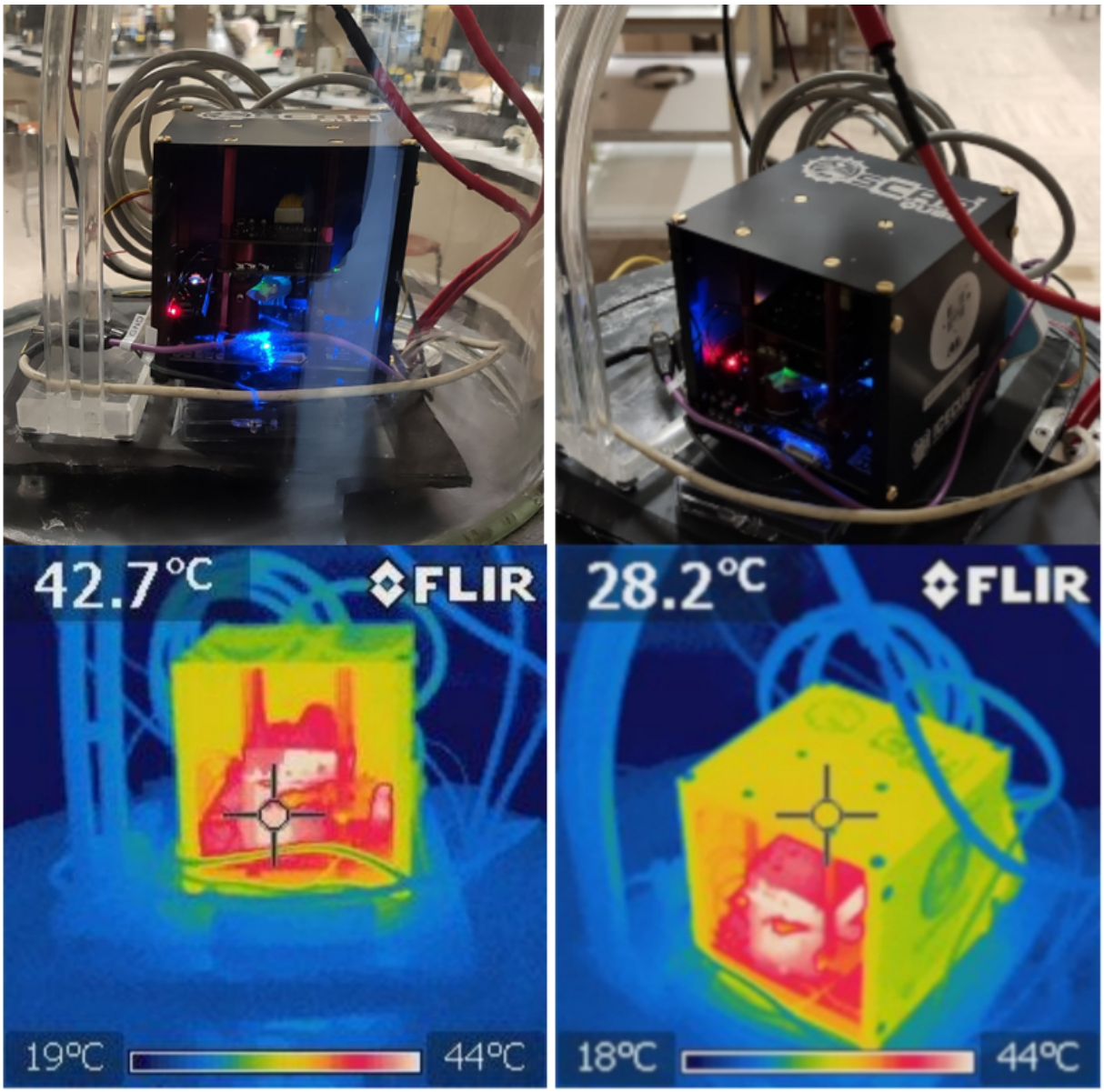

Figure 5.22: FLIR image before testing the OSCAR-QUBE in vacuum. On the left a frontal perspective is shown to measure the inside temperature of the OSCAR-QUBE. On the right an angled perspective is shown to measure the outside temperature of the OSCAR-QUBE. Regular picture on the top, thermal picture on the bottom

After this, the vacuum is being formed to test the OSCAR-QUBE within this extreme environment. The OSCAR-QUBE was tested in a (medium) vacuum of 0.68 millibar or 68 Pa, as can be seen in Figure 5.23.

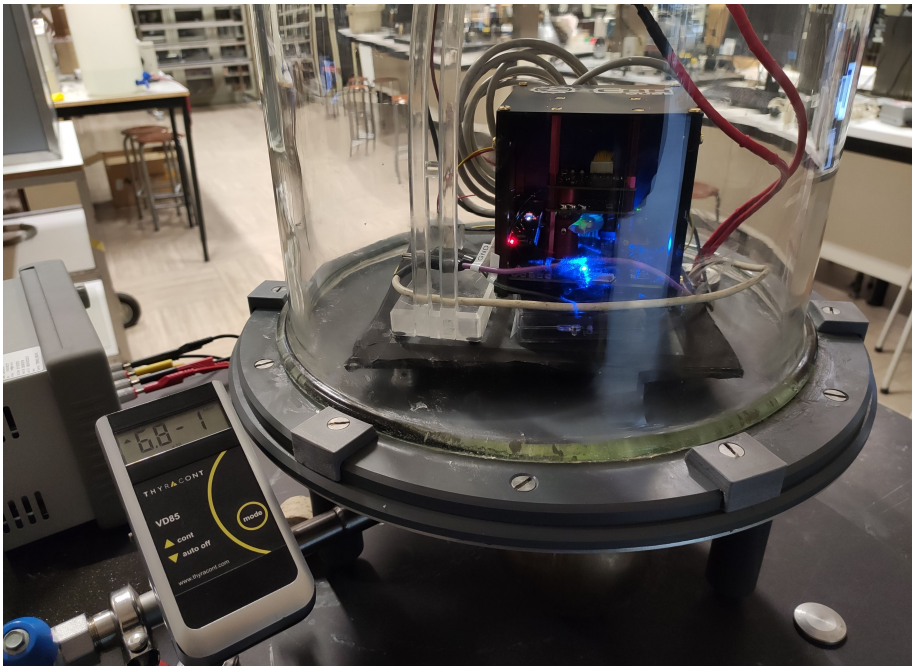

Figure 5.23: OSCAR-QUBE under 68 Pa (medium) vacuum.

The vacuum formation was done during the run at 13 mW (R0200), resulting in some initial fluctuation for this run. After this, the resistance is lowered to R0100, which is 33 mW. Finally, the full power setting of 50 mW (R0000) is used to run the setup. This is all being done while the ODMR signal is being measured. For the test at 13 mW, the highest temperature measured is 47°C. For the test on 33 mW and 50 mW, the highest recorded temperatures are 57°C, and 65°C, respectively. These recordings can be seen in Figure 5.24. The temperature was recorded at 45 samples per second.

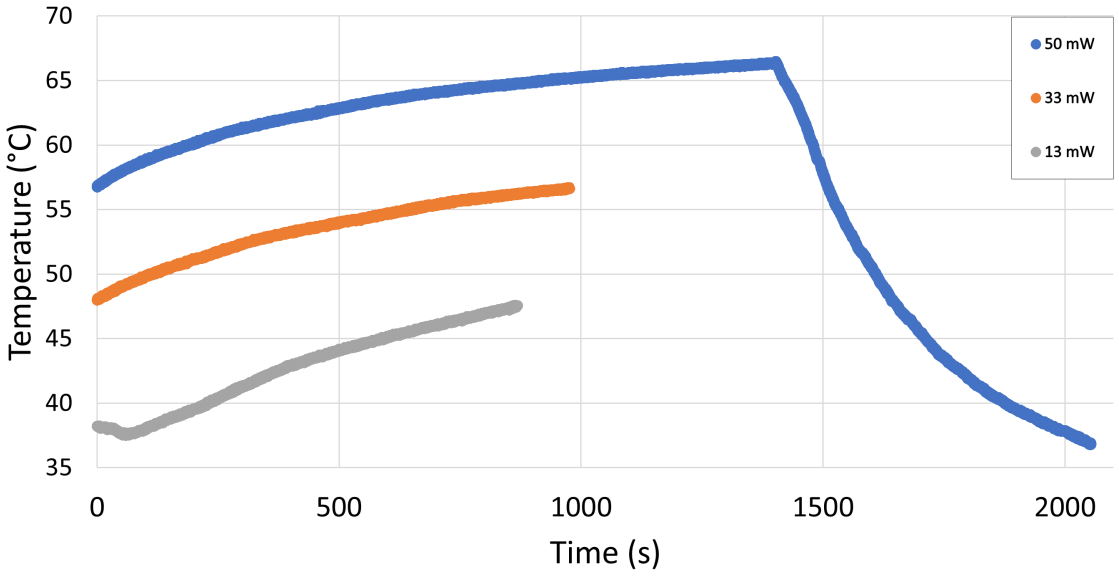

Figure 5.24: Graph showing the laser temperature over a number of samples.

On its own, the previous graph does not say a lot. The entire ranges include the heating, and for the data on 50 mW, it even shows the cooldown. A more in-depth view is created by selecting the last 15k samples, averaging them, and calculating the standard deviation. In Figure 5.25 these are added to the measurements that were conducted in ambient environments of 22 °C and 1013 millibar atmospheric pressure.

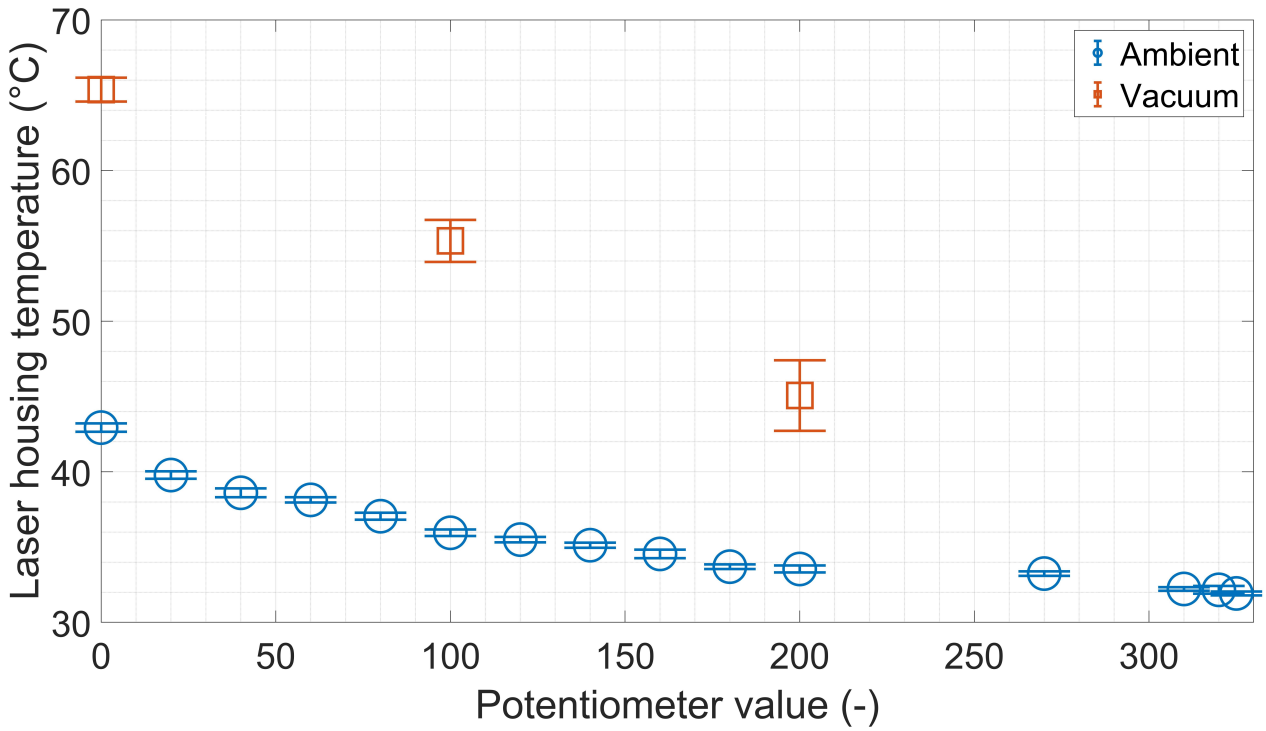

Figure 5.25: Ambient and vacuum temperature in relation to potentiometer value.

Here, it was evident that the lack of convectional heat transfer and the reduced conduction heat transfer significantly affects the temperatures to which the LD and other components are exposed. These differences can be observed in Table 5.2 which expands on 5.1. The temperature delta increases over time for higher power output.

Furthermore, the standard deviations are significantly higher compared to the results in ambient testing. This can be accounted for by the prolonged heating effect happening in the vacuum environment. The temperatures need more time to stabilize in vacuum compared to atmospheric operation. Table 5.2 and Figure 5.24 confirm this. The highest standard deviation (5.2%) is found in the first test, which was performed at 13 mW. The following tests, at 33 mW and 50 mW, delivered lower standard deviations in absolute and percentage terms. The test at the highest power output was performed for a longer duration, allowing the temperature to stabilize, resulting in a lower standard deviation.

Table 5.2: Potentiometer settings with corresponding laser output values and the temperatures in ambient and vacuum operation. In bold the maximum values for the standard deviations are shown. For improved readability please refer to Appendix A

Potentiometer setting (-)	0	20	40	60	80	100	120	140	160	180	200	270		310	320	325
Laser Output Power (mW)	49.54	48.66	45.02	41.06	37.11	33.05	28.94	24.77	20.97	17.45	12.95	4.84		1.55	0.79	0.45
Standard deviation (mW)	0.027	0.024	0.016	0.009	0.008	0.014	0.026	0.028	**0.074**	0.031	0.058	0.022		0.006	0.055	0.012
Standard deviation (%)	0.055	0.049	0.036	0.022	0.021	0.042	0.089	0.113	0.353	0.178	**0.448**	0.455		0.387	6.962	2.667
Laser Temperature (°C)	42.93	39.79	38.61	38.14	37.05	35.95	35.50	35.13	34.55	33.70	33.55	33.24		32.22	32.17	31.92
Standard deviation (°C)	0.276	0.251	**0.298**	0.173	0.229	0.215	0.179	0.169	0.281	0.154	0.229	0.148		0.123	0.256	0.131
Standard deviation (%)	0.641	0.631	0.772	0.453	0.618	0.598	0.504	0.481	**0.813**	0.457	0.683	0.445		0.382	0.796	0.410
Laser Temp. Vacuum (°C)	65.37	/	/	/	/	55.32	/	/	/	/	45.06	/		/	/	/
Standard deviation (°C)	0.793	/	/	/	/	1.397	/	/	/	/	**2.339**	/		/	/	/
Standard deviation (%)	1.213	/	/	/	/	2.524	/	/	/	/	**5.189**	/		/	/	/
Laser Temp. Delta (°C)	22.44	/	/	/	/	19.37	/	/	/	/	11.51	/		/	/	/

After the tests were concluded, the OSCAR-QUBE was quickly re-pressurized to capture the thermals with the FLIR camera. In Figure 5.26, the hottest temperature being displayed is 64.4°C. Compared to the thermals on the inside of the OSCAR-QUBE, the outside is much cooler. The hottest point on the outside, seen in Figure 5.27, of the OSCAR-QUBE, was 38°C.

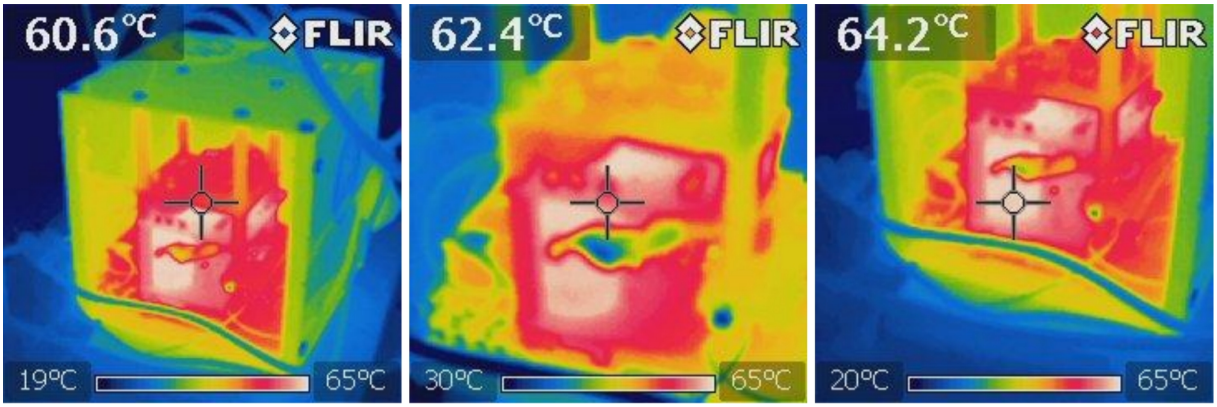

Figure 5.26: Thermal images of the inside captured by FLIR thermal camera.

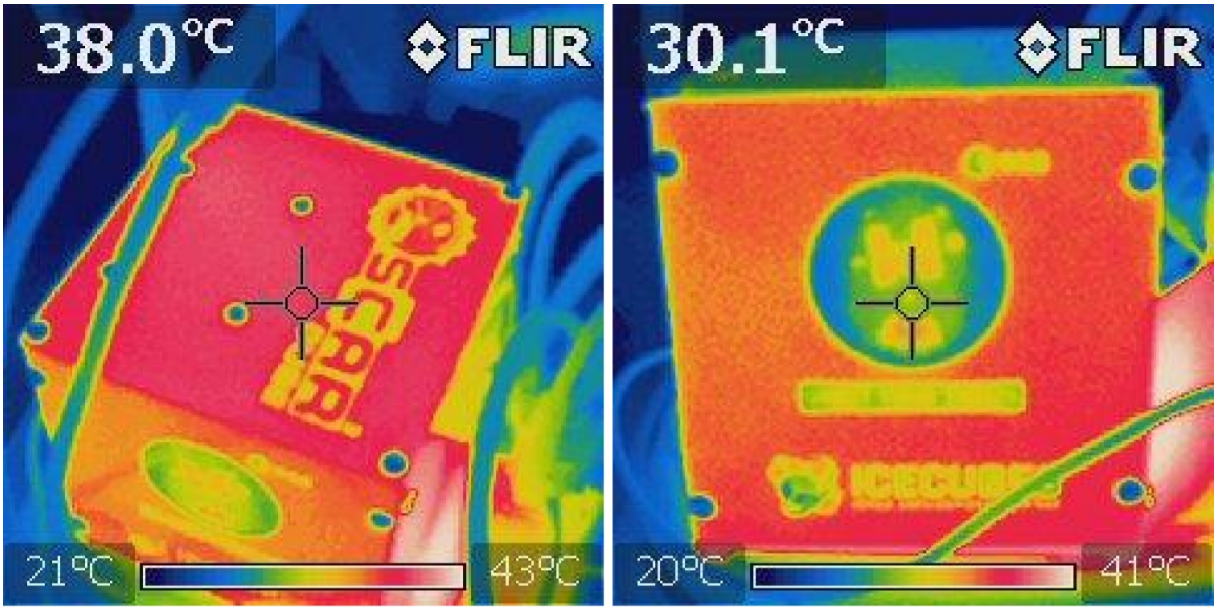

Figure 5.27: Thermal images of the outside captured by FLIR thermal camera.

In addition to the temperature being taken directly after testing, several FLIR images have been captured 10 minutes after these tests were concluded. These can be seen in Figure 5.28. Here it is seen that the hottest temperatures have dropped by 8°C. The highest temperature on the outside can be found at the bottom of the QUBE at 29.9°C.

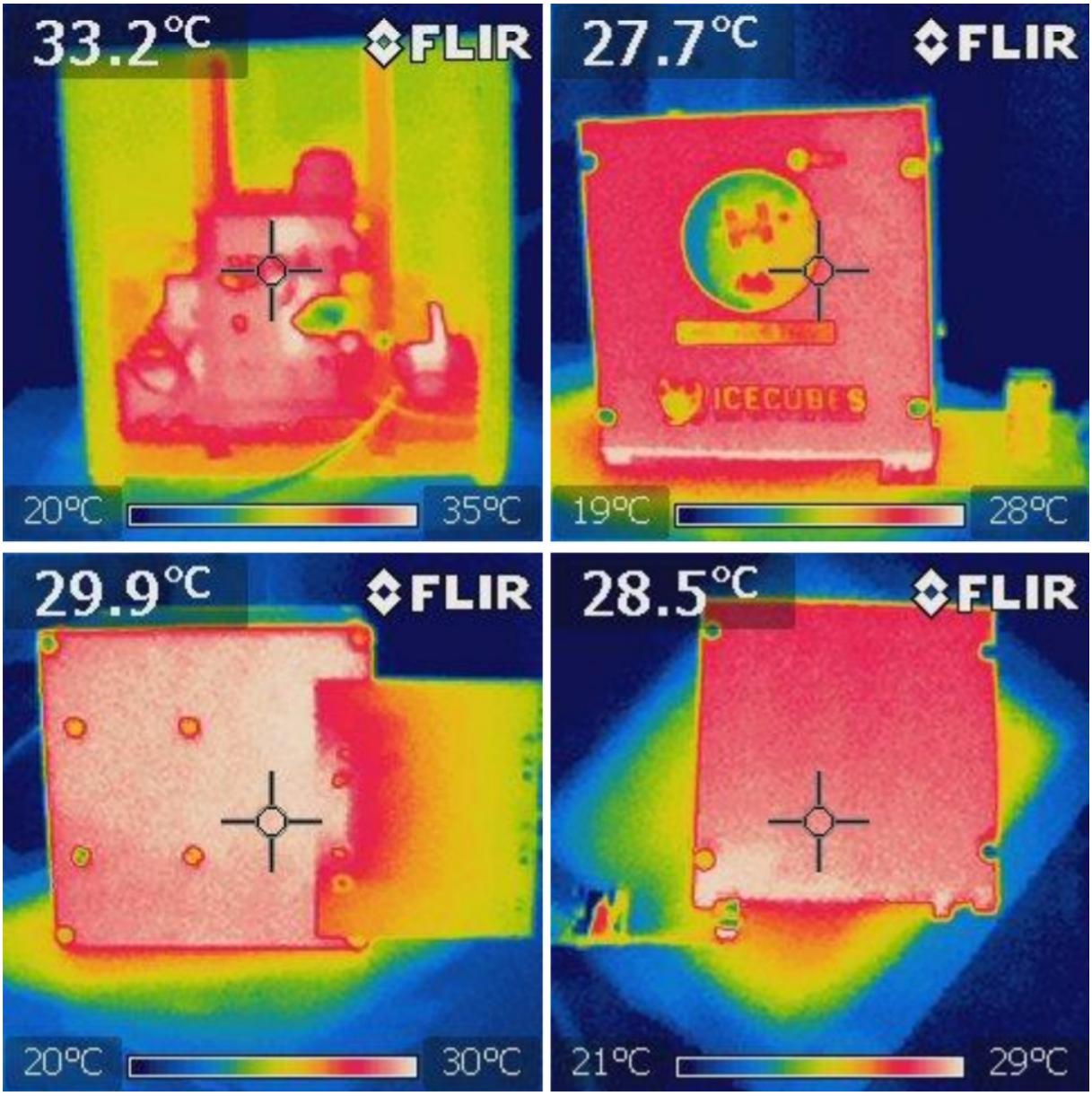

Figure 5.28: Thermals after 10 minutes of not being powered.

When processing the data gathered during testing, the measurements are able to show us the mean ODMR voltage for any given set. The higher the optical laser output power, the higher the resulting ODMR voltage. This can be seen in Figure 5.29. However, with an increase in temperature, this ODMR voltage drops. This behavior is as expected. When operating continuously within a stable temperature environment, such shifting behavior is not seen.

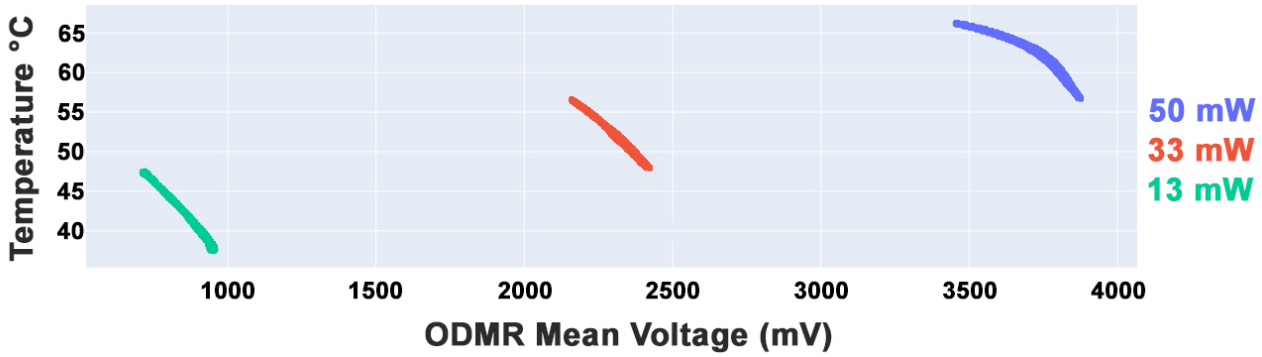

Figure 5.29: Mean ODMR voltage in function of the laser temperature.

Power consumption during vacuum testing

This is 467 mA and 403 mA, respectively. This sums up to 7.2 W of power. This includes the power that is used by the router from the 5V line.

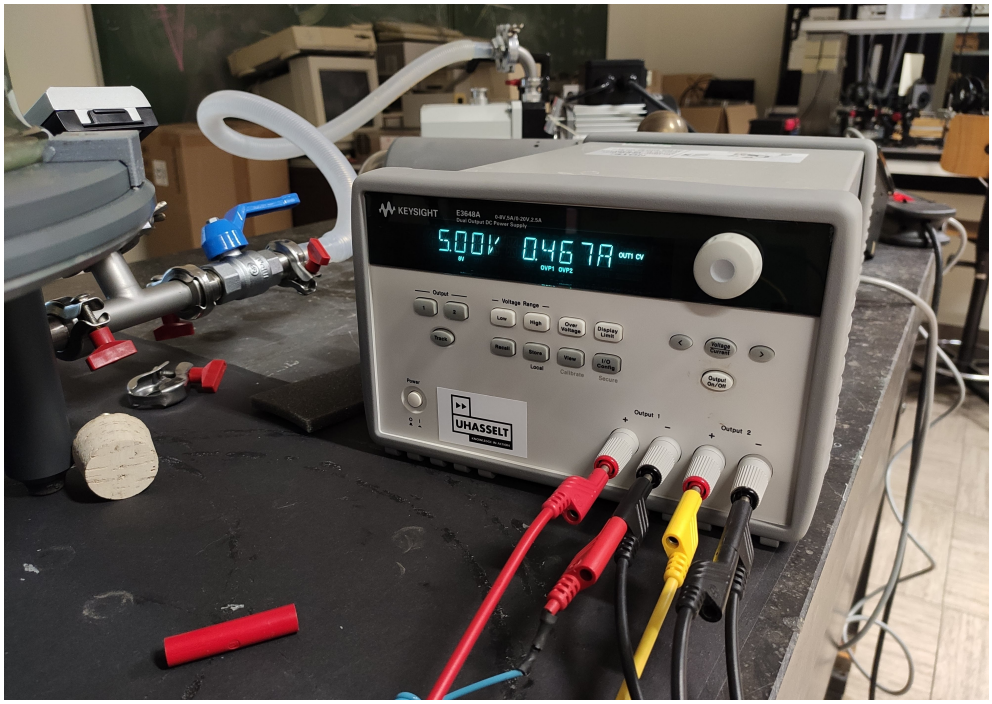

Figure 5.30: 5 V output and the corresponding current usage.

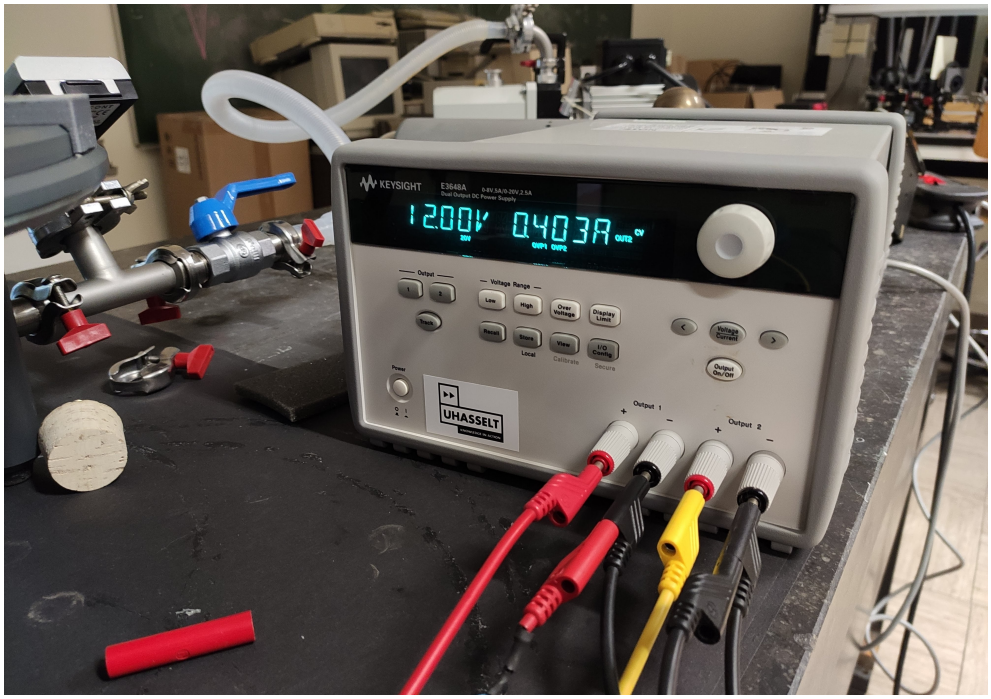

Figure 5.31: 12 V output and the corresponding current usage.

5.2.4 Final performance testing

In this section the final system performance is described. This is done for CW and pulsed ODMR. PDMR is not included, the reasoning behind this can be found in Section 5.3.

CW ODMR performance

The best ODMR signal is found with the highest laser powers. This can be seen in the delta of the ODMR voltage. This is the difference between the highest and the lowest voltage seen in the ODMR signal. The higher the laser power, the more significant the difference in the height of the peaks becomes. This delta can be seen in Table 5.3. The corresponding graphs can be seen in Appendix B.

Table 5.3: ODMR Delta in mV for the corresponding potentiometer settings.

Potentiometer setting (-)	0	25	50	75	100	200	270	310
Delta (mV)	31.98	30.95	28.50	25	22.01	9.43	4.01	1.12

In Figure 5.32 all the CW ODMR signals for the potentiometer settings seen in the previous graph are shown. From a quick visual inspection it is clear that the R0310 and R0270 setting are the worst from the range. When excluding these, as seen in Figure 5.33, the remaining potentiometer setting seem to deliver good results with well defined peaks in the ODMR signal.

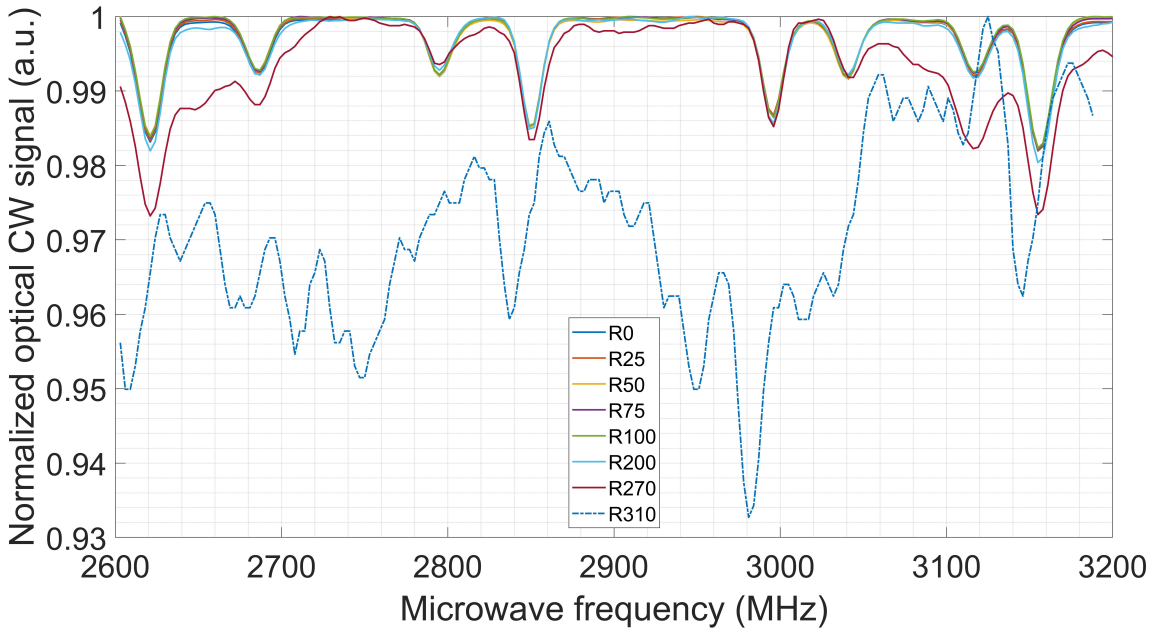

Figure 5.32: Comparison of ODMR quality for potentiometer settings ranging from R0000 to R0310.

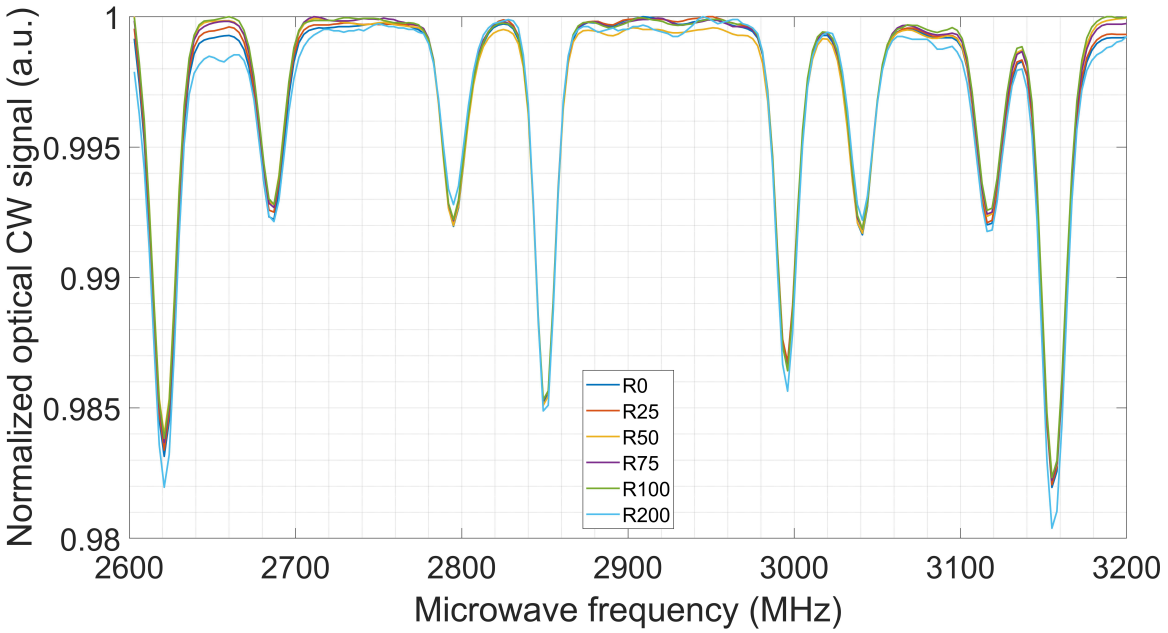

Figure 5.33: Comparison of ODMR quality for potentiometer settings ranging from R0000 to R0200.

The CW ODMR performance is tested at $\tilde{5}0$ mW. Without any averaging there is some noise visible in the ODMR signals. By averaging, the signal the peaks get more defined and the top end of the signal gets flattened out. These differences can be observed in Figure 5.34. For the raw ODMR signals please see Appendix C.

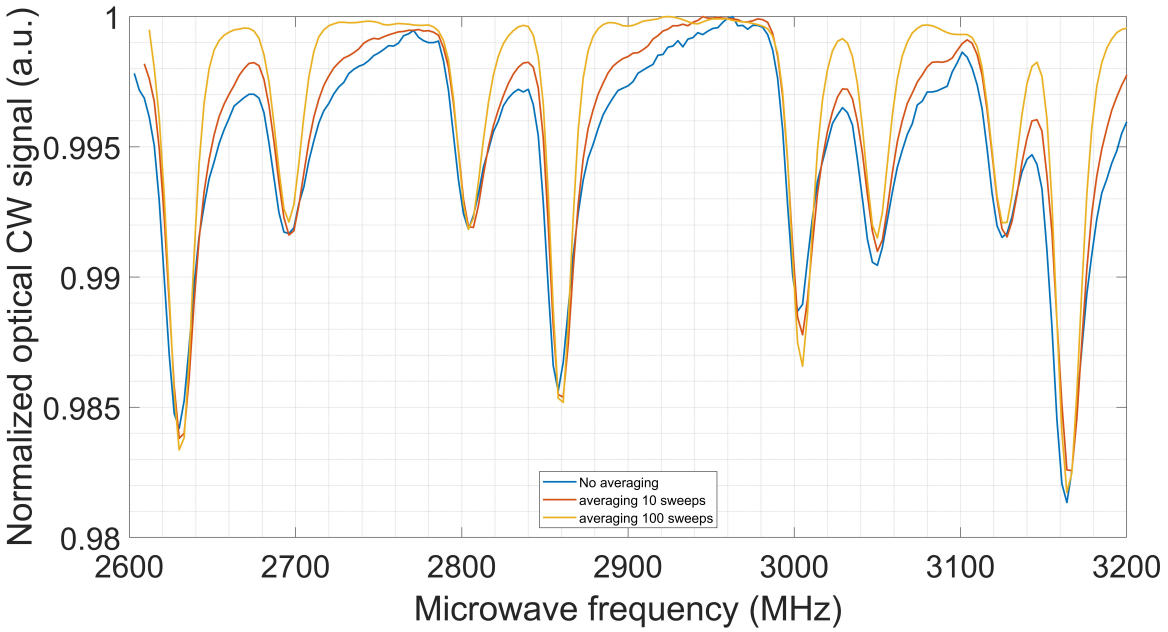

Figure 5.34: Comparison of CW ODMR signals using different levels of averaging.

Pulsed ODMR performance

For the pulsed ODMR, a similar effect is seen. However, without any averaging, the signal is almost unrecognizable as can be seen in the second part of Appendix C. By increasing the averaging the noise is cleaned up. The averaging starts at 10, followed by 100, and finally one at 400 sweeps. The pulse width is 5 μs which is equal to 5000 ns for Figure 5.35 and 1 μs or 1000 ns for Figure 5.36. The individual graphs can also be seen in Appendix C.

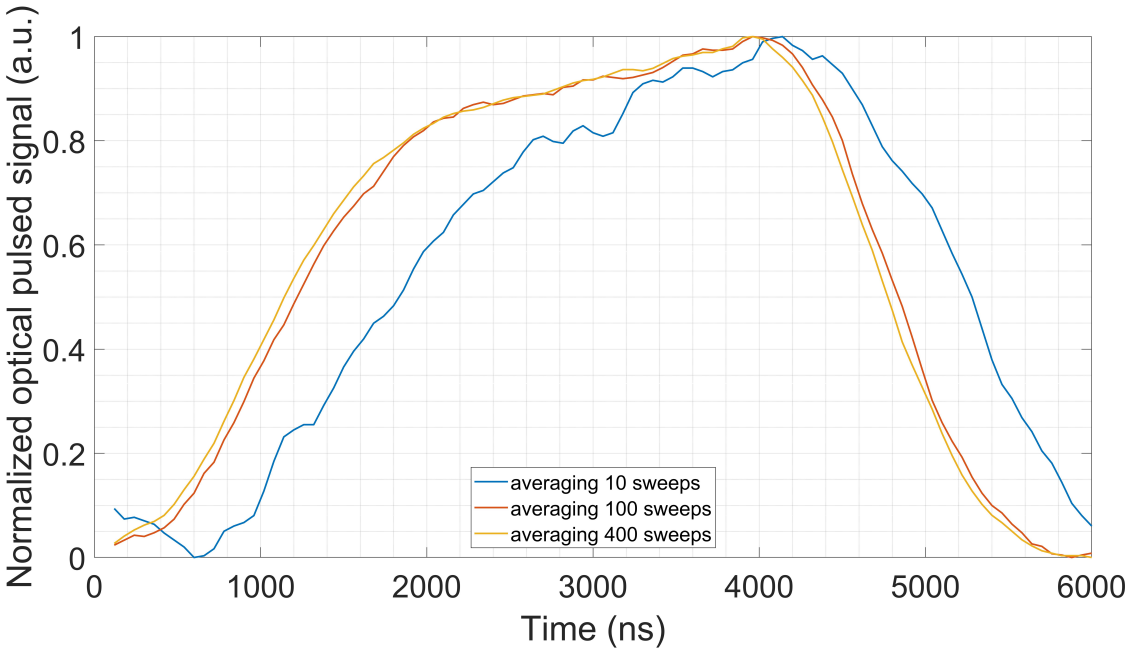

Figure 5.35: Comparison of 5 μs pulsed ODMR signals using different levels of averaging.

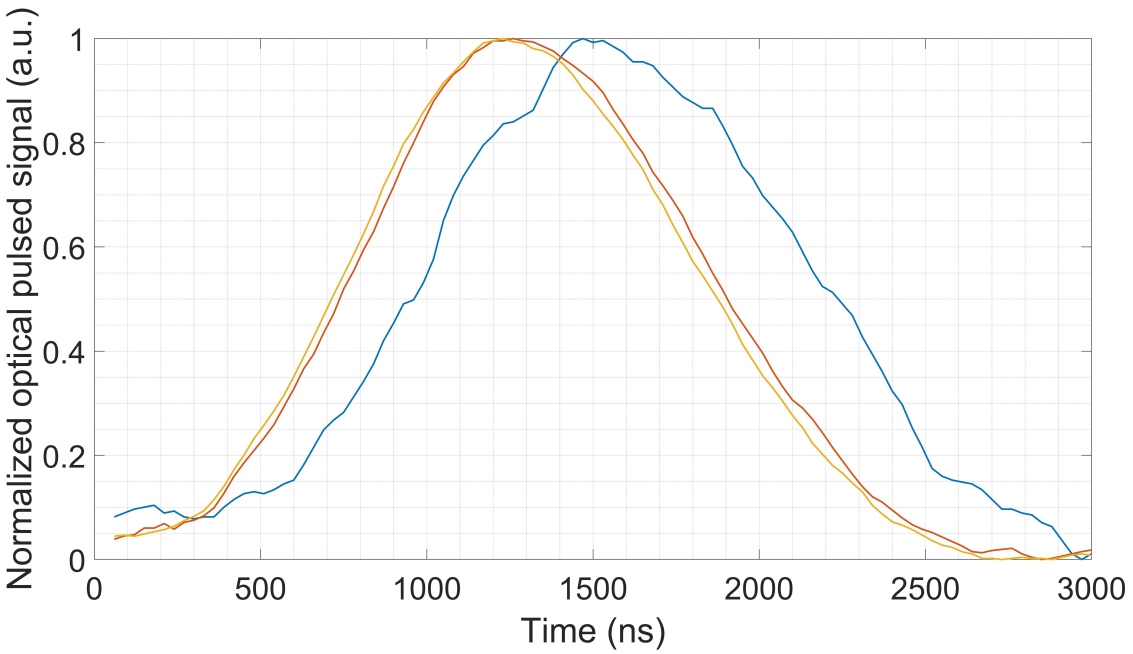

Figure 5.36: Comparison of 1 μs pulsed ODMR signals using different levels of averaging.

5.3 Issues

During the testing, the non-nominal behavior of the laser power as a function of set resistance with the digital potentiometer was observed. This can be seen in Table 5.4. By checking the values, it was evident that the digital potentiometer was setting its resistance incorrectly. Resistance is dropping and rising inexplicably before plummeting by over 5000 Ω. During further inspection, a problem with the interface was found, which due to slight tilt, was not having proper contact after the stack assembly. The board-to-board connector was re-soldered, which resolved the issues.

Table 5.4: Notes taken during a debug session to find the cause of the irregular power output.

Potentiometer setting	Laser Power (mW)	Resistance (Ω)
900	0.045	9220
800	0.04	8760
700	0.06	9800
600	0.05	7960
500	14.5	2470

Simultaneous readout of ODMR and PDMR is possible on the TBM. Figure 5.37 displays both ODMR and PDMR taken by the TBM using sample #353. However, due to the limitations of the different diamond samples used in the flight and ground model, the obtained PDMR does not yield good results. For that reason, the focus has been primarily on ODMR.

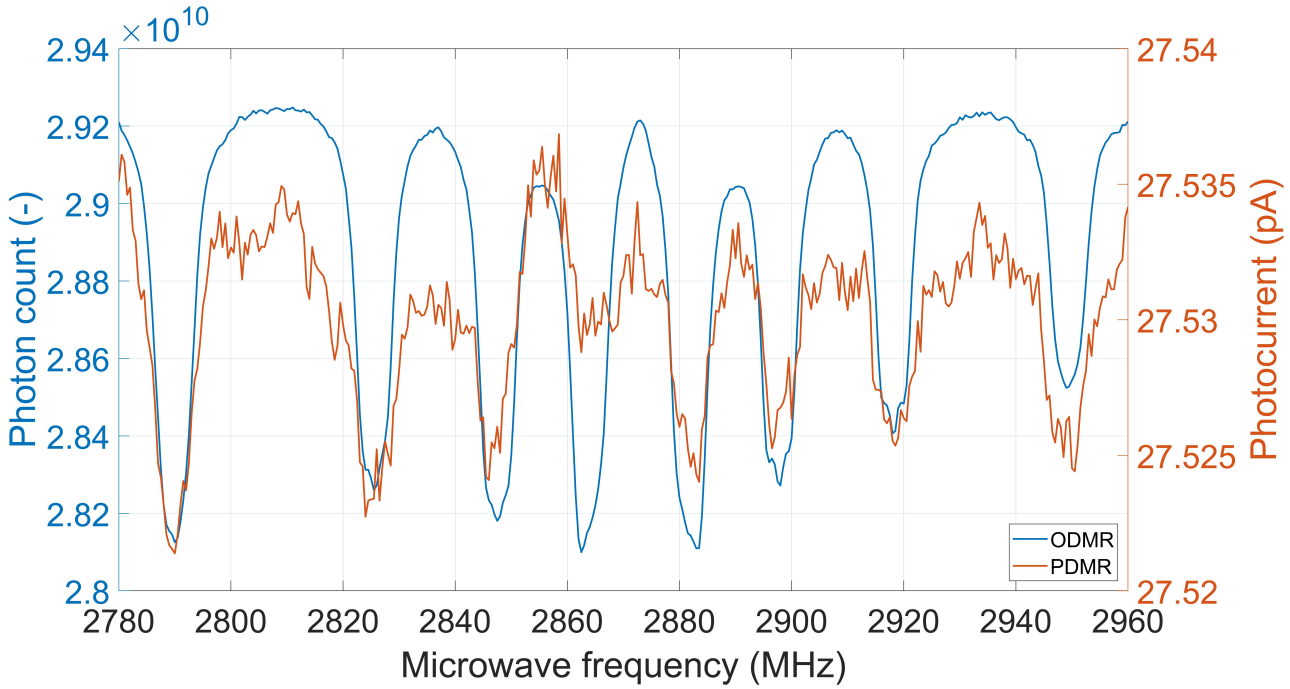

Figure 5.37: PDMR measurement taken on the test-bench model using diamond sample #353.

Chapter 6

Conclusion

This thesis set out to develop the laser subsystem for the OSCAR-QUBE with the testing and characterization of the performance in pulsed and continuous-wave operation in mind. This can be split up into a set of phases. The research phase is followed by the preliminary design phase, critical design phase, and operational phase.

Within the research phase of this thesis, there was much documentation to read in order to get up to speed on the science and technology behind the project itself. This can be seen in the thorough theoretical background, seen in Chapter 2. After this, the desired specifications for the OSCAR-QUBE laser subsystem got determined.

Following the research phase, the preliminary design phase is entered. In this phase, the initial electrical schematics, PCB layout, and the Test-Bench Model (TBM) of the OSCAR-QUBE laser subsystem were developed. Any issues that surfaced during this phase of development for any of the subsystems got resolved.

The critical design phase is next. No issues arose during the previous phase for the laser subsystem, resulting in using the same electrical schematics and PCB layout for the Proto-Flight Models (PFM). These models were used to finalize the testing before participating in the official ESA flight acceptance review (FAR). Testing done in this phase shows that the laser subsystem features an optical output power that ranges from 0 mW to 50 mW, with a standard deviation below 0.5%, temperatures that remain below 43 °C in ambient environments, with a standard deviation of 0.8%. The minimum pulse width of 10 ns the laser diode can provide is more than enough as the typical used pulse widths range from 1 μs to 4 μs.

At the time of finalizing this thesis, the OSCAR-QUBE passed the FAR and is being prepared for payload integration to be flown on the SpaceX Commercial Resupply Service mission, planned for the 18^{th} of August 2021, more specifically SpaceX CRS-23. By successfully passing in-depth reviews and tests performed in conjunction with ESA engineers and subcontractors, the development of the laser subsystem for the OSCAR-QUBE sensor in line with this thesis was a success. As the timeline regarding the 'Orbit Your Thesis!' program exceeds the timeline for the master's, the project's operational phase aboard the ISS is not covered within this thesis. Furthermore, the return to Earth or decommission phase is not covered either. Future OSCAR members will need to continue the work by gathering, analyzing, and presenting our quantum magnetometer results based on diamond. Even after this, work can be done to improve the performance of the technology further.

Future work

- Investigate the correlation between temperature and ODMR mean voltage.
- Investigate the application of pulse schemes to ODMR and PDMR measurements.
- Resolve capacitive behavior of the readout system.
- Analyze the data the OSCAR-QUBE collects in orbit.

References

[1] "Materials science — rexus/bexus." 2021 [Online], Available: `http://rexusbexus.net/experiments/scientific-research/materials-science/`, [Accessed on May 23, 2021].

[2] "Magnetic field research — rexus/bexus." 2021 [Online], Available: `http://rexusbexus.net/experiments/scientific-research/magnetic-field-research/`, [Accessed on May 23, 2021].

[3] L. Rondin, J.-P. Tetienne, T. Hingant, J.-F. Roch, P. Maletinsky, and V. Jacques, "Magnetometry with nitrogen-vacancy defects in diamond," *Reports on Progress in Physics*, vol. 77, p. 056503, may 2014.

[4] P. R. W. HUDSON and P. P. PHAKEY, "Defects in natural type IB diamond," *Nature*, vol. 269, pp. 227–229, Sept. 1977.

[5] A. Haque and S. Sumaiya, "An overview on the formation and processing of nitrogen-vacancy photonic centers in diamond by ion implantation," *Journal of Manufacturing and Materials Processing*, vol. 1, p. 6, Aug. 2017.

[6] "Optical studies of the 1.945 eV vibronic band in diamond," *Proceedings of the Royal Society of London. A. Mathematical and Physical Sciences*, vol. 348, pp. 285–298, Feb. 1976.

[7] J. O. Orwa, C. Santori, K. M. C. Fu, B. Gibson, D. Simpson, I. Aharonovich, A. Stacey, A. Cimmino, P. Balog, M. Markham, D. Twitchen, A. D. Greentree, R. G. Beausoleil, and S. Prawer, "Engineering of nitrogen-vacancy color centers in high purity diamond by ion implantation and annealing," *Journal of Applied Physics*, vol. 109, p. 083530, Apr. 2011.

[8] T. Wolf, P. Neumann, K. Nakamura, H. Sumiya, T. Ohshima, J. Isoya, and J. Wrachtrup, "Subpicotesla diamond magnetometry," *Phys. Rev. X*, vol. 5, p. 041001, Oct 2015.

[9] M. W. Doherty, N. B. Manson, P. Delaney, F. Jelezko, J. Wrachtrup, and L. C. Hollenberg, "The nitrogen-vacancy colour centre in diamond," *Physics Reports*, vol. 528, pp. 1–45, July 2013.

[10] J. M. Taylor, P. Cappellaro, L. Childress, L. Jiang, D. Budker, P. R. Hemmer, A. Yacoby, R. Walsworth, and M. D. Lukin, "High-sensitivity diamond magnetometer with nanoscale resolution," *Nature Physics*, vol. 4, pp. 810–816, Sept. 2008.

[11] D. Griffiths, *Introduction to quantum mechanics*. Englewood Cliffs, N.J: Prentice Hall, 1995.

[12] A. Gruber, "Scanning confocal optical microscopy and magnetic resonance on single defect centers," *Science*, vol. 276, pp. 2012–2014, June 1997.

[13] E. Bourgeois, M. Gulka, and M. Nesladek, "Photoelectric detection and quantum readout of nitrogen-vacancy center spin states in diamond," *Advanced Optical Materials*, vol. 8, p. 1902132, Apr. 2020.

[14] S. A. Momenzadeh, R. J. Stöhr, F. F. de Oliveira, A. Brunner, A. Denisenko, S. Yang, F. Reinhard, and J. Wrachtrup, "Nanoengineered diamond waveguide as a robust bright platform for nanomagnetometry using shallow nitrogen vacancy centers," *Nano Letters*, vol. 15, pp. 165–169, Dec. 2014.

[15] P. Siyushev, M. Nesladek, E. Bourgeois, M. Gulka, J. Hruby, T. Yamamoto, M. Trupke, T. Teraji, J. Isoya, and F. Jelezko, "Photoelectrical imaging and coherent spin-state readout of single nitrogen-vacancy centers in diamond," *Science*, vol. 363, pp. 728–731, Feb. 2019.

[16] J. F. Barry, J. M. Schloss, E. Bauch, M. J. Turner, C. A. Hart, L. M. Pham, and R. L. Walsworth, "Sensitivity optimization for NV-diamond magnetometry," *Reviews of Modern Physics*, vol. 92, Mar. 2020.

[17] E. Bourgeois, A. Jarmola, P. Siyushev, M. Gulka, J. Hruby, F. Jelezko, D. Budker, and M. Nesladek, "Photoelectric detection of electron spin resonance of nitrogen-vacancy centres in diamond," *Nature Communications*, vol. 6, Oct. 2015.

[18] K. Jensen, V. M. Acosta, A. Jarmola, and D. Budker, "Light narrowing of magnetic resonances in ensembles of nitrogen-vacancy centers in diamond," *Physical Review B*, vol. 87, Jan. 2013.

[19] N. Bar-Gill, L. Pham, C. Belthangady, D. L. Sage, P. Cappellaro, J. Maze, M. D. Lukin, A. Yacoby, and R. Walsworth, "Spectroscopy of composite solid-state spin environments for improved metrology with spin ensembles," *arXiv preprint arXiv:1112.0667*, 2011.

[20] K. Xia, "Spectroscopy of single rare earth solid-state qubits," 2016.

[21] J. Hecht, *The Laser Guidebook*. New York Blacklick: McGraw-Hill Professional PublishingMcGraw-Hill Companies, The distributor, 1999.

[22] X. Qin, W. Zhang, L. Wang, Y. Zhao, Y. Tong, X. Rong, and J. Du, "An FPGA-based hardware platform for the control of spin-based quantum systems," *IEEE Transactions on Instrumentation and Measurement*, vol. 69, pp. 1127–1139, Apr. 2020.

[23] U. M. Malzahn, "Driving laser diodes." Apr. 2006 [Online], Available: `https://www.ichaus.de/upload/pdf/laser-handout2ups.pdf`, [Accessed on Oct 03, 2020].

[24] iC Haus, "ic-nzn n-type laser diode driver." 2018 [Online], Available: `https://www.ichaus.de/upload/pdf/NZN_datasheet_D1en.pdf`, [Accessed on Oct 03, 2020].

[25] EUCommision, "Commission decision of 5 february 2014 on the safety requirements to be met by european standards for consumer laser products pursuant to directive 2001/95/ec of the european parliament and of the council on general product safety." Feb. 5, 2014 [Online], Available: `https://eur-lex.europa.eu/legal-content/EN/TXT/PDF/?uri=CELEX:32014D0059&from=EN`, [Accessed on Mar 5, 2021].

[26] O. P. Inc., "Optima laser diode application notes and glossary." [Online], Available: `http://www.optima-optics.com/pdf/NOTES.PDF`, [Accessed on Oct 10, 2020].

[27] P. Horowitz, *The art of electronics*. New York, NY, USA: Cambridge University Press, 2015.

[28] T. Jarvis, "Best practice in circuit board design." [Online], Available: http://home.iitb.ac.in/~pradeepsarin/students/tether/generalectronicsfundaes/EMCPCB.pdf, [Accessed on Oct 21, 2020].

[29] Altium, "Pcb design techniques to reduce emi." [Online], Available: https://resources.altium.com/sites/default/files/uberflip_docs/file_731.pdf, [Accessed on Nov 09, 2020].

[30] Altium, "Via stitching and via shielding — altium designer 21 user manual — documentation." Jan. 6, 2021 [Online], Available: https://www.altium.com/documentation/altium-designer/via-stitching-and-via-shielding-ad, [Accessed on Feb 25, 2021].

[31] S. Ling, *University physics*. Houston, Texas Minneapolis: OpenStax College, Rice University, Open Textbook Library, 2016.

[32] NASA, "Microgravity science on the iss." 2021 [Online], Available: https://www.nasa.gov/pdf/501343main_Microgravity_Science.pdf, [Accessed on May 12, 2021].

[33] "ic-nz1d evaluation board description." [Online], Available: https://www.distrelec.be/Web/Downloads/_t/ds/iC-NZ-EVAL-NZ1D_eng_tds.pdf, [Accessed on Oct 03, 2020].

[34] "Thorlabs - l520p50 520 nm, 50 mw, Ø5.6 mm, a pin code, laser diode." [Online], Available: https://www.thorlabs.com/thorproduct.cfm?partnumber=L520P50, [Accessed on Oct 03, 2020].

[35] I. Thorlabs, "L520p50 - 520 nm laser diode, 50 mw." Apr. 2015 [Online], Available: https://www.thorlabs.com/drawings/364c8b5973220b0e-91B0955E-B45E-56BF-F567D4EE0D280670/L520P50-SpecSheet.pdf, [Accessed on Sept 25, 2020].

[36] "Thorlabs - pm100d compact power and energy meter console, digital 4" lcd." [Online], Available: https://www.thorlabs.com/thorproduct.cfm?partnumber=PM100D, [Accessed on May 08, 2021].

[37] "Operation manual thorlabs instrumentation optical power and energy meter pm100d." [Online], Available: https://www.thorlabs.com/drawings/60f30d5ca1b76ea4-07AAF1C7-C456-3469-C5E74F7914A2C9E8/PM100D-Manual.pdf, [Accessed on May 08, 2021].

[38] "Thorlabs - s121c standard photodiode power sensor, si, 400 - 1100 nm, 500 mw." [Online], Available: https://www.thorlabs.com/thorproduct.cfm?partnumber=S121C, [Accessed on May 08, 2021].

[39] "Thorlabs - s121c compact photodiode power head with silicon detector - datasheet." [Online], Available: https://www.thorlabs.com/drawings/60f30d5ca1b76ea4-07AAF1C7-C456-3469-C5E74F7914A2C9E8/S121C-SpecSheet.pdf, [Accessed on May 08, 2021].

[40] Maxim-Integrated, "Max5481–max5484 10-bit, nonvolatile, linear-taper digital potentiometer." 2010 [Online], Available: https://datasheets.maximintegrated.com/en/ds/MAX5481-MAX5484.pdf, [Accessed on Oct 14, 2020).

[41] "Tl-wr702n — 150mbps wireless n nano router — tp-link." [Online], Available: https://www.tp-link.com/us/home-networking/wifi-router/tl-wr702n/, [Accessed on May 06, 2021].

[42] "Flir i7 datasheet." 2009 [Online], Available: https://www.instrumart.com/assets/FLIR-i7-Data-Sheet.pdf, [Accessed on May 06, 2021].

[43] "Leybold trivac d 2.5 ld, rotary vane vacuum pump. operating instructions,." [Online], Available: https://www.idealvac.com/files/ManualsII/Leybold_D_E2_5OI.pdf, [Accessed on May 08, 2021].

[44] Digilent, "Cmod a7 reference manual." 2016 [Online], Available: https://reference.digilentinc.com/_media/cmod_a7/cmod_a7_rm.pdf, [Accessed on May 17, 2021].

[45] Digilent, "Analog discovery 2 reference manual." 2015 [Online], Available: https://reference.digilentinc.com/_media/reference/test-and-measurement/analog-discovery-2/ad2_rm.pdf, [Accessed on May 19, 2021].

[46] "Pcb design software & tools — altium." [Online], Available: https://www.altium.com/, [Accessed on May 05, 2021].

[47] "Packet sender - free utility to for sending / receiving of network packets. tcp, udp, ssl.." [Online], Available: https://packetsender.com/, [Accessed on May 05, 2021].

[48] "Wireshark." [Online], Available: https://www.wireshark.org/, [Accessed on May 05, 2021].

[49] "Matplotlib: Python plotting — matplotlib 3.4.1 documentation." [Online], Available: https://matplotlib.org/, [Accessed on May 05, 2021].

[50] "Numpy." [Online], Available: https://numpy.org/, [Accessed on May 05, 2021].

[51] R. Semiconductor, "Ba178mxx series application information." 2020 [Online], Available: https://fscdn.rohm.com/en/products/databook/applinote/ic/power/linear_regulator/ba178mxx_app_info_an-e.pdf, [Accessed on May 22, 2021].

Appendix A

Appendix - Large Tables

Table A.1: Potentiometer settings with corresponding laser output values. In bold the maximum values for the standard deviations are shown.

Potentiometer setting (-)	0	20	40	60	80	100	120	140	160	180	200	270		310	320	325
Laser Output Power (mW)	49.54	48.66	45.02	41.06	37.11	33.05	28.94	24.77	20.97	17.45	12.95	4.84		1.55	0.79	0.45
Standard deviation (mW)	0.027	0.024	0.016	0.009	0.008	0.014	0.026	0.028	**0.074**	0.031	0.058	0.022		0.006	0.055	0.012
Standard deviation (%)	0.055	0.049	0.036	0.022	0.021	0.042	0.089	0.113	0.353	0.178	**0.448**	0.455		0.387	6.962	2.667
Laser Temperature (°C)	42.93	39.79	38.61	38.14	37.05	35.95	35.50	35.13	34.55	33.70	33.55	33.24		32.22	32.17	31.92
Standard deviation (°C)	0.276	0.251	**0.298**	0.173	0.229	0.215	0.179	0.169	0.281	0.154	0.229	0.148		0.123	0.256	0.131
Standard deviation (%)	0.641	0.631	0.772	0.453	0.618	0.598	0.504	0.481	**0.813**	0.457	0.683	0.445		0.382	0.796	0.410

Table A.2: Potentiometer settings with corresponding laser output values and the temperatures in ambient and vacuum operation.

Potentiometer setting (-)	0	20	40	60	80	100	120	140	160	180	200	270		310	320	325
Laser Output Power (mW)	49.54	48.66	45.02	41.06	37.11	33.05	28.94	24.77	20.97	17.45	12.95	4.84		1.55	0.79	0.45
Standard deviation (mW)	0.027	0.024	0.016	0.009	0.008	0.014	0.026	0.028	**0.074**	0.031	0.058	0.022		0.006	0.055	0.012
Standard deviation (%)	0.055	0.049	0.036	0.022	0.021	0.042	0.089	0.113	0.353	0.178	**0.448**	0.455		0.387	6.962	2.667
Laser Temperature (°C)	42.93	39.79	38.61	38.14	37.05	35.95	35.50	35.13	34.55	33.70	33.55	33.24		32.22	32.17	31.92
Standard deviation (°C)	0.276	0.251	**0.298**	0.173	0.229	0.215	0.179	0.169	0.281	0.154	0.229	0.148		0.123	0.256	0.131
Standard deviation (%)	0.641	0.631	0.772	0.453	0.618	0.598	0.504	0.481	**0.813**	0.457	0.683	0.445		0.382	0.796	0.410
Laser Temp. Vacuum (°C)	65.37	/	/	/	/	55.32	/	/	/	/	45.06	/		/	/	/
Standard deviation (°C)	0.793	/	/	/	/	1.397	/	/	/	/	**2.339**	/		/	/	/
Standard deviation (%)	1.213	/	/	/	/	2.524	/	/	/	/	**5.189**	/		/	/	/
Laser Temp. Delta (°C)	22.44	/	/	/	/	19.37	/	/	/	/	11.51	/		/	/	/

Appendix B

Appendix - ODMR Quality

The graphs shown here, are showing the ODMR signal using 300 samples to average over an increasing amount of laser power. The purpose is to highlight that the lower potentiometer setting, corresponding to higher laser output power values, lead to higher quality measurements.

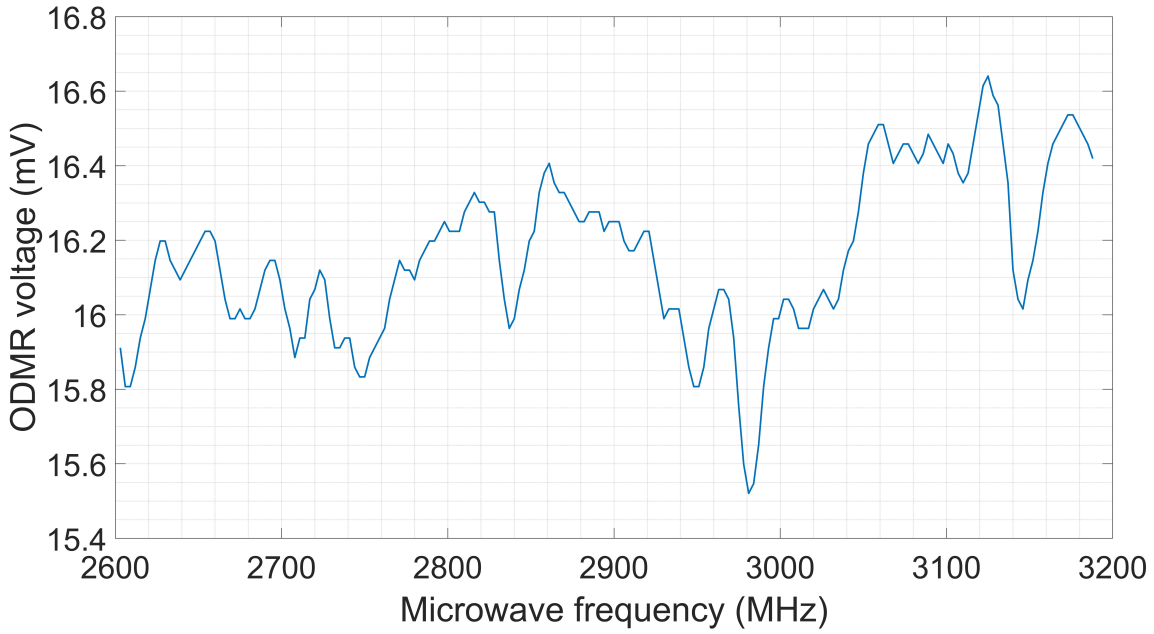

Figure B.1: ODMR Quality at R0310

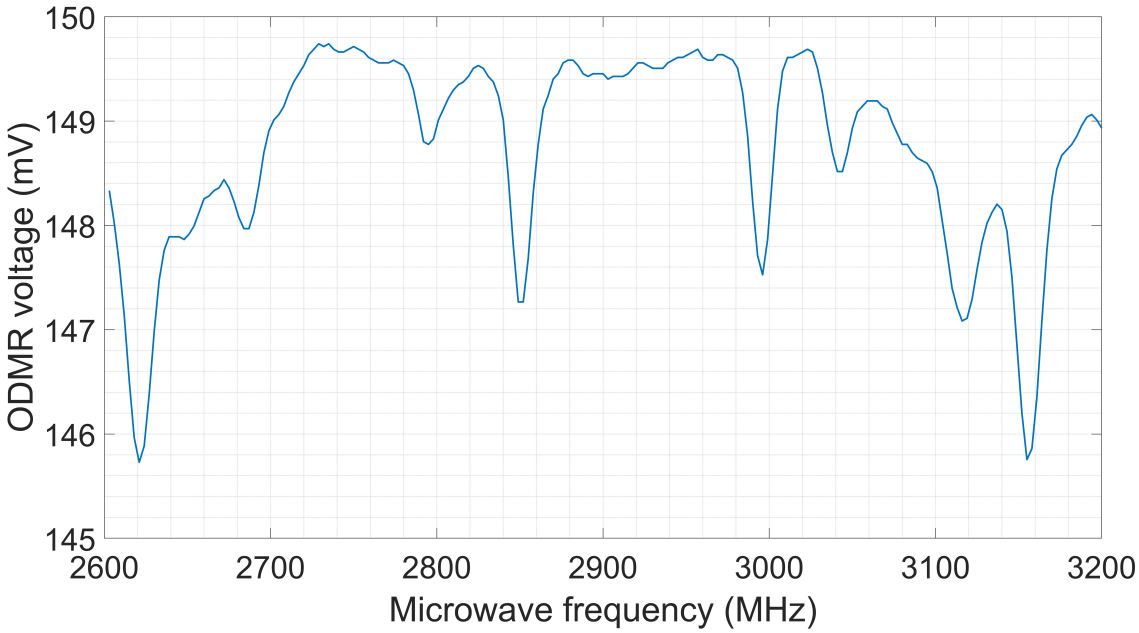

Figure B.2: ODMR Quality at R0270

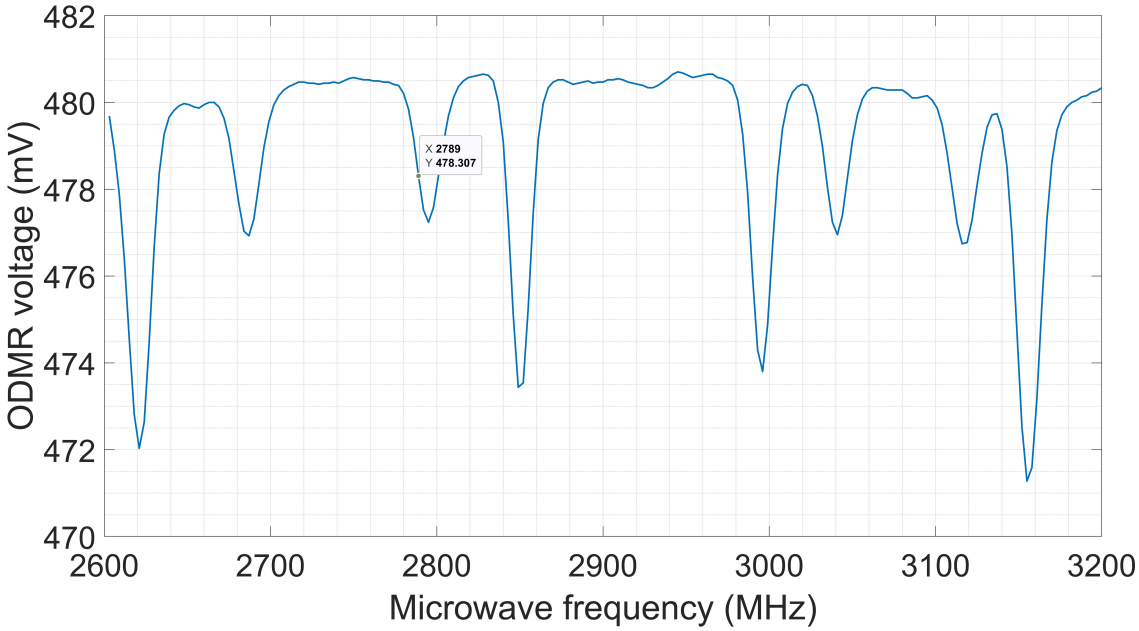

Figure B.3: ODMR Quality at R0200

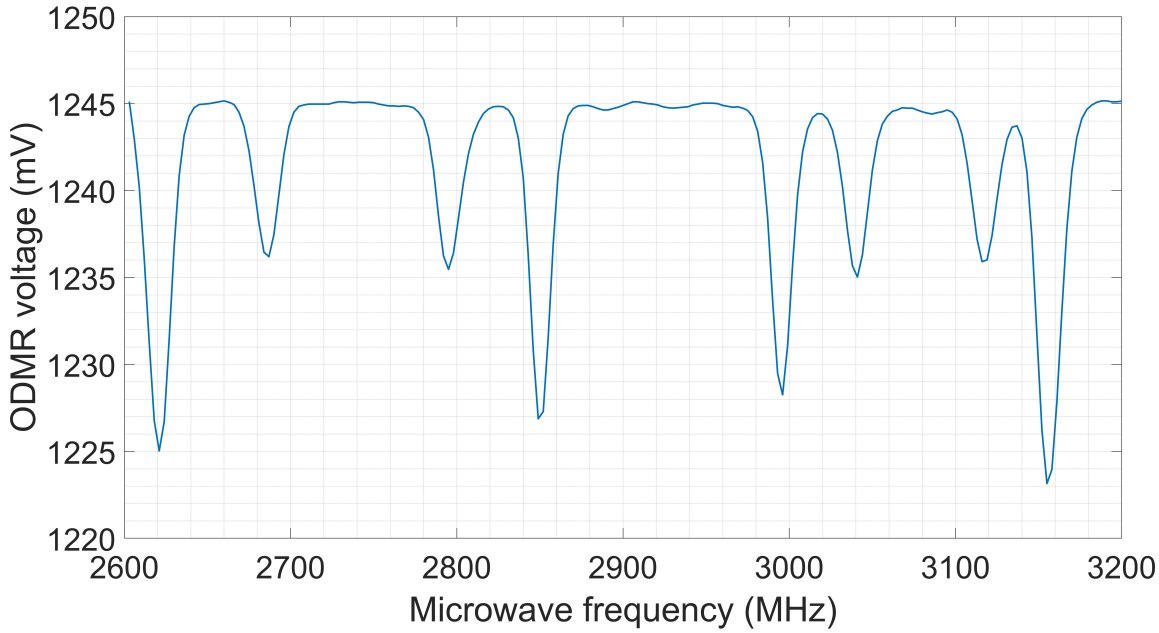

Figure B.4: ODMR Quality at R0100

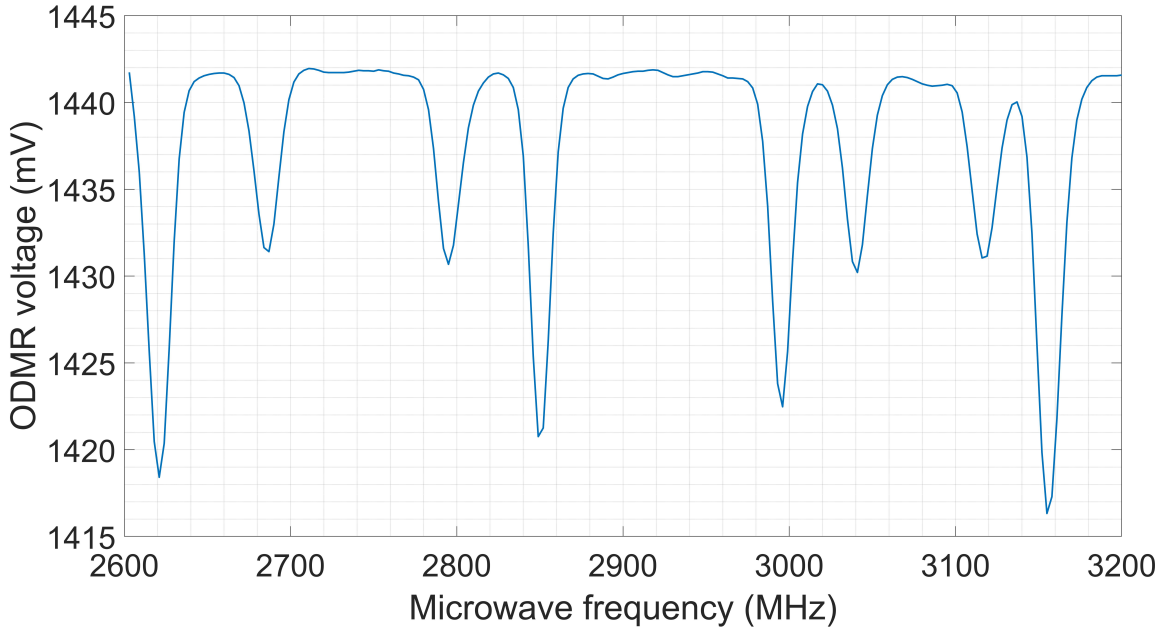

Figure B.5: ODMR Quality at R0075

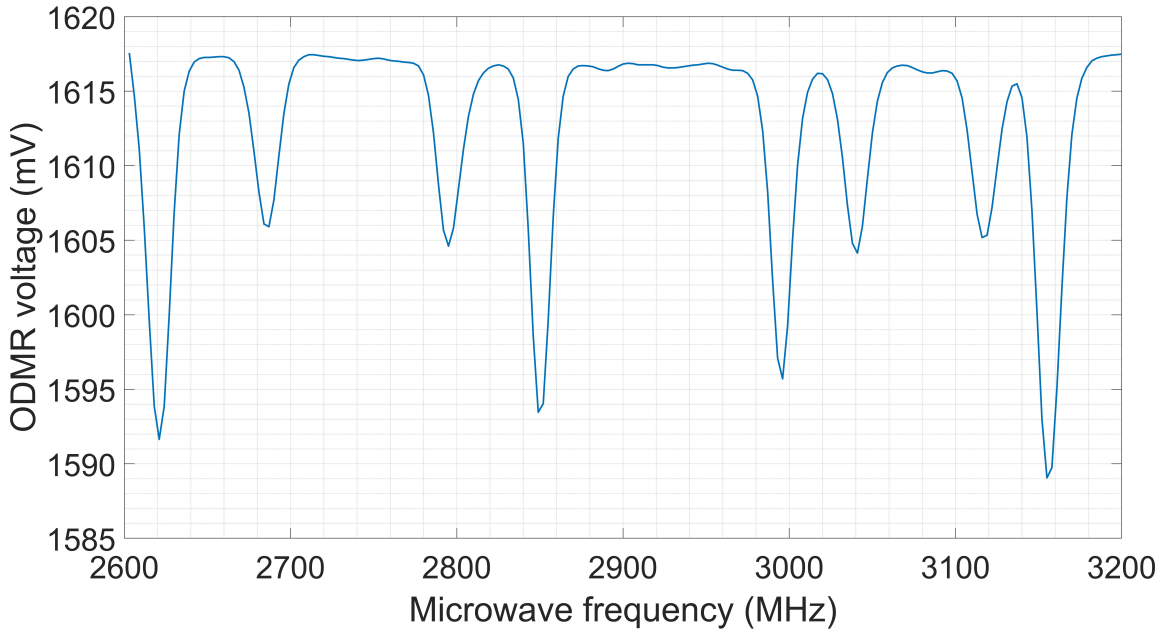

Figure B.6: ODMR Quality at R0050

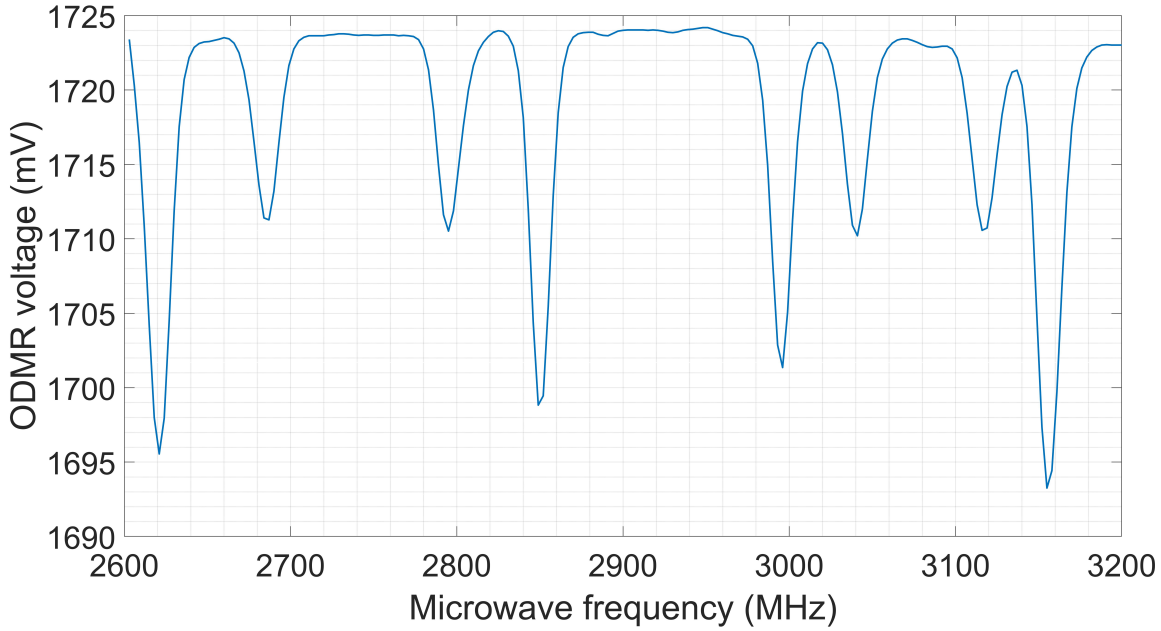

Figure B.7: ODMR Quality at R0025

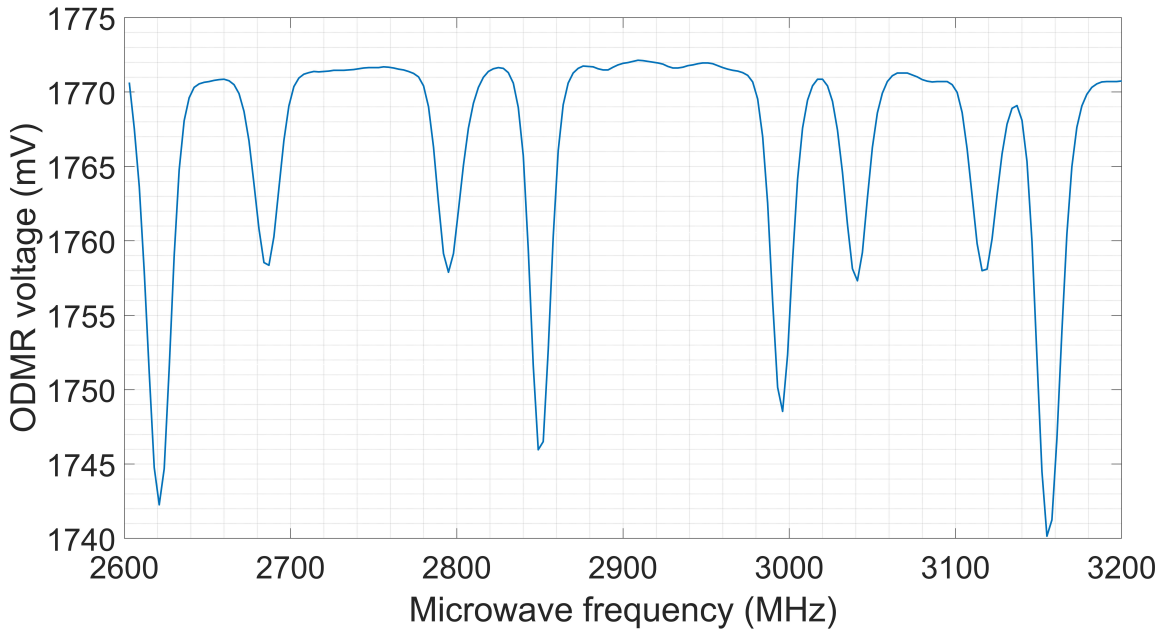

Figure B.8: ODMR Quality at R0000

Appendix C

Appendix - CW and pulsed ODMR Averaging

The graphs contained in Appendix A show the data obtained from CW ODMR and Pulsed ODMR measurements. For CW ODMR the number of photons detected can be seen on the Y-axis, on the X-axis the MW frequency can be seen. By averaging the peaks become more narrow and the tops are flattened out. After the CW ODMR graphs show the the data obtained from pulsed ODMR measurements. The first four graphs in these measurements had a set pulse width of 5000 ns or 5 μs. Without averaging the pulse is not recognizable in the data. The last three graphs are captured with a set pulse width of 1000 ns or 1 μs. In these graphs the capacitive effect is clearly visible.

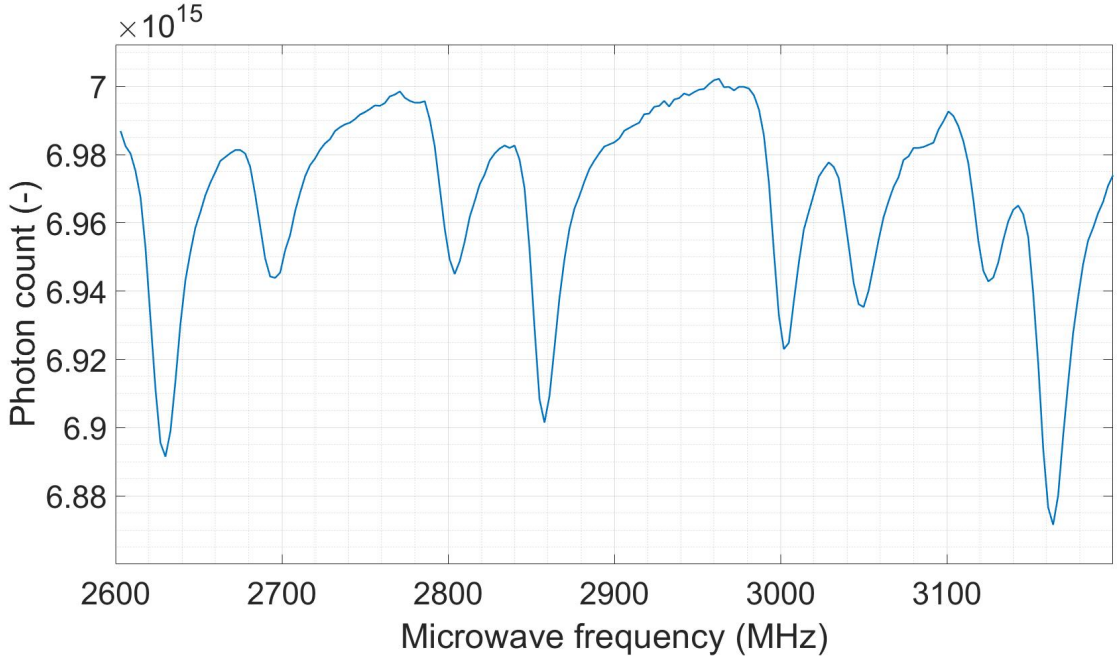

Figure C.1: ODMR signal without averaging at full power.

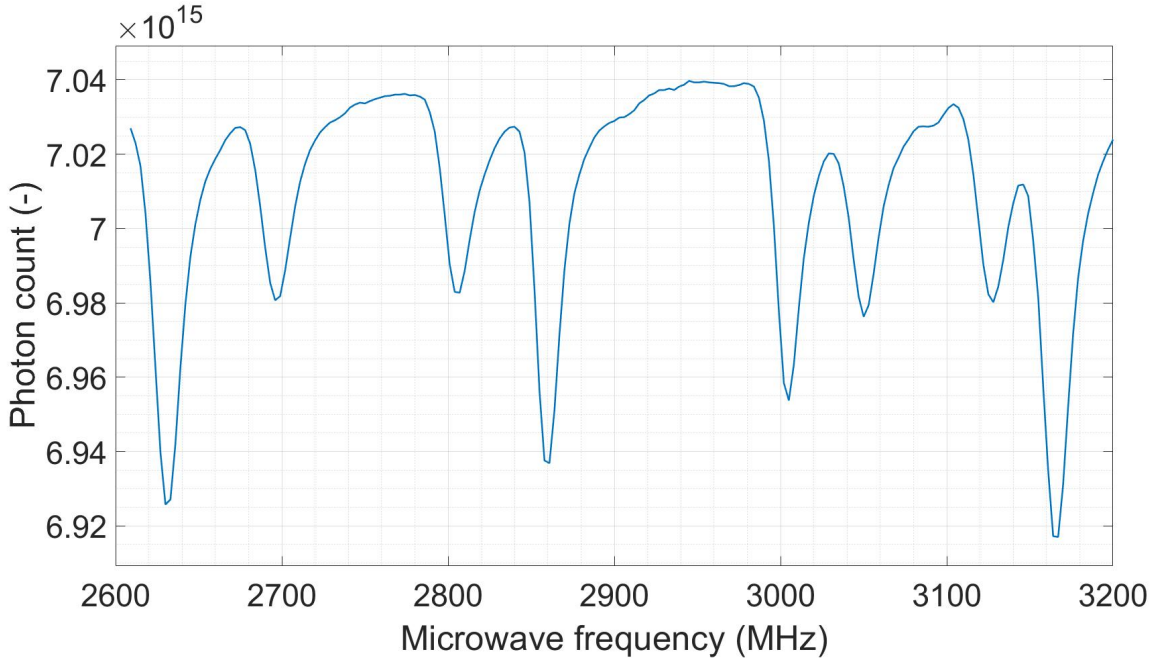

Figure C.2: ODMR signal with averaging of 10 sweeps at full power.

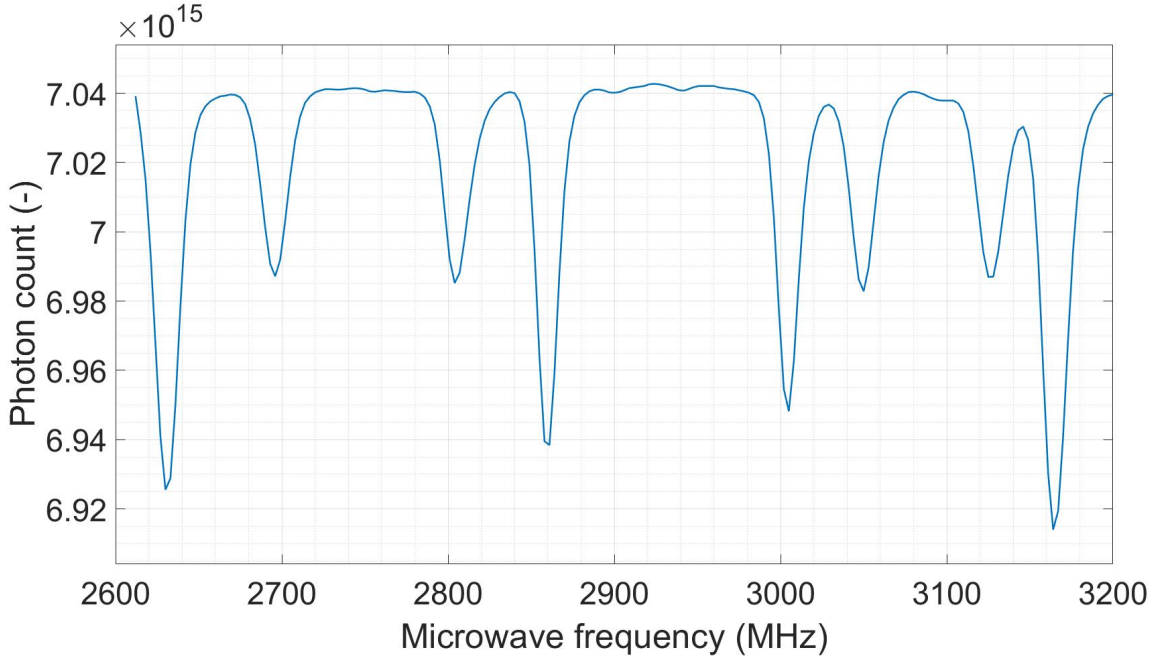

Figure C.3: ODMR signal with averaging of 100 sweeps at full power.

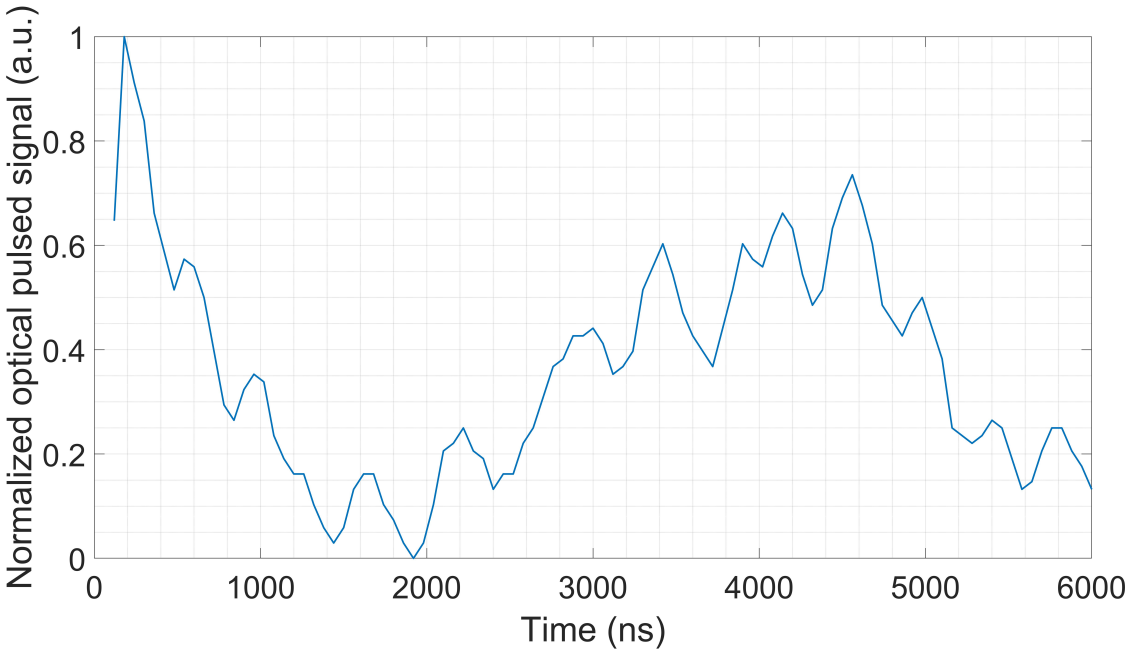

Figure C.4: 5 μs pulse ODMR signal with no averaging at full power.

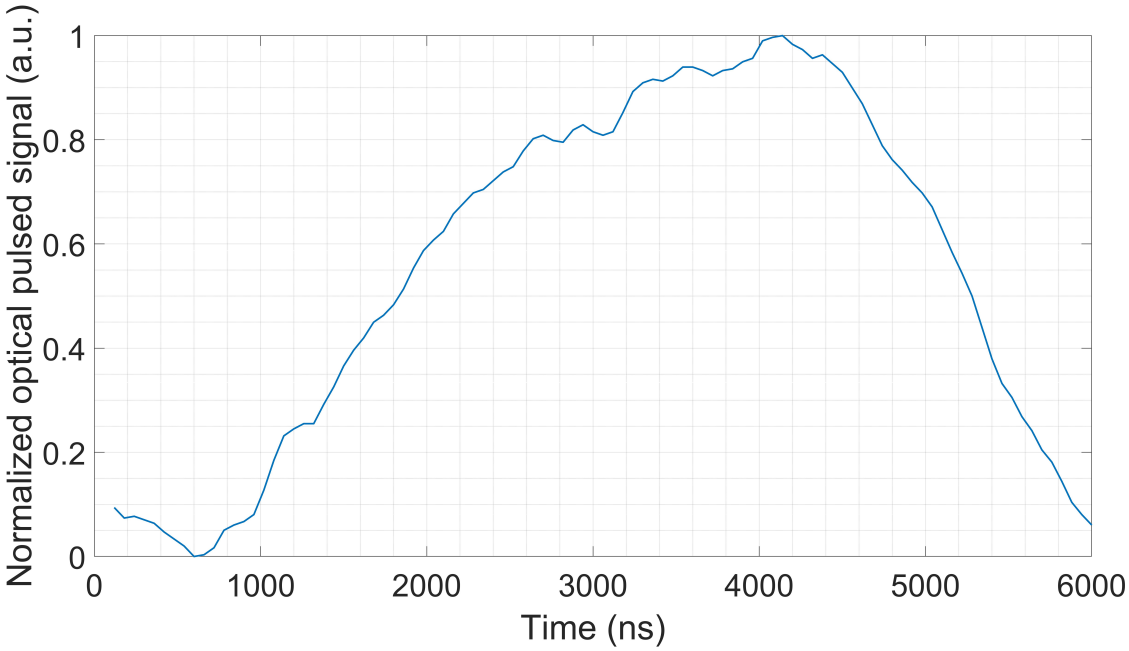

Figure C.5: 5 μs pulse ODMR signal with averaging of 10 at full power.

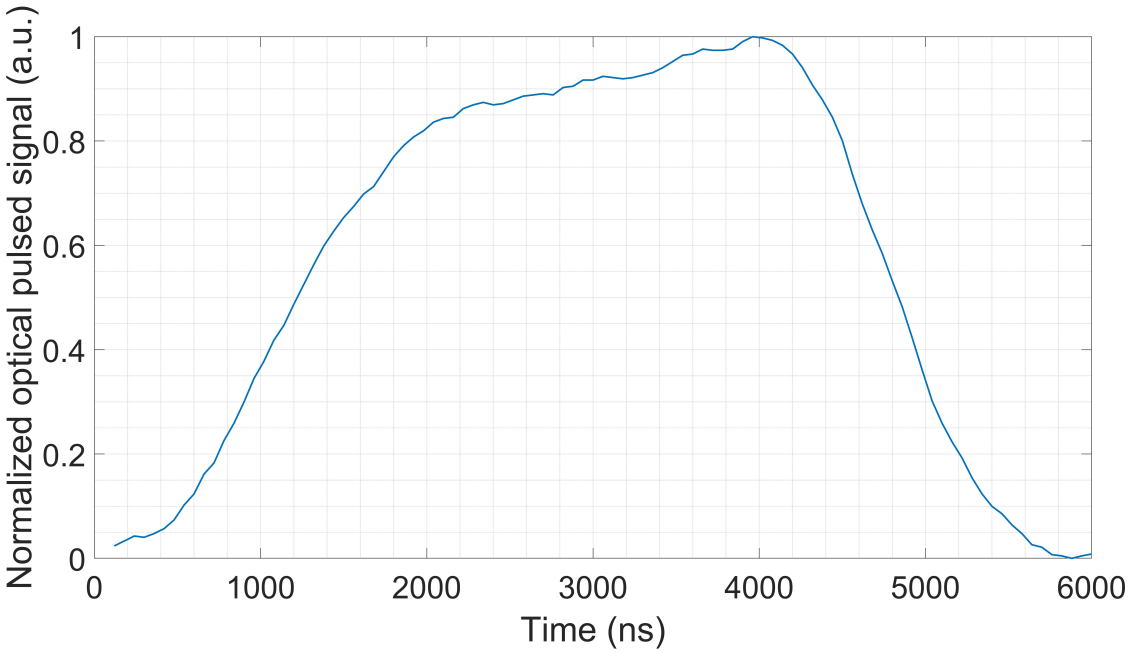

Figure C.6: 5 μs pulse ODMR signal with averaging of 100 at full power.

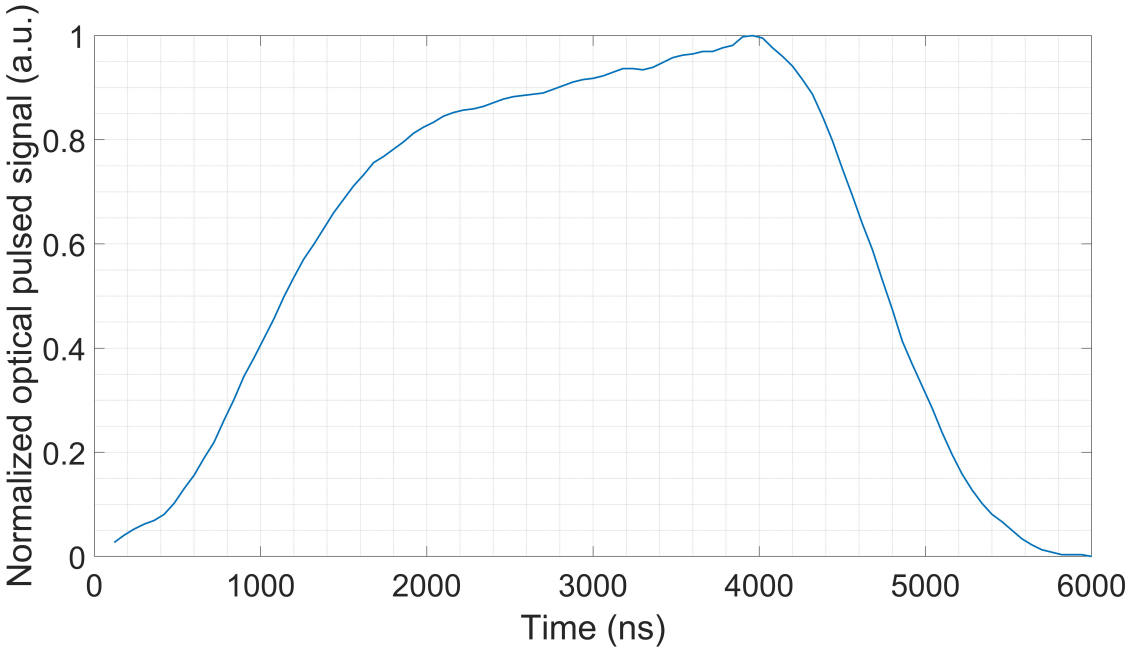

Figure C.7: 5 μs pulse ODMR signal with averaging of 400 at full power.

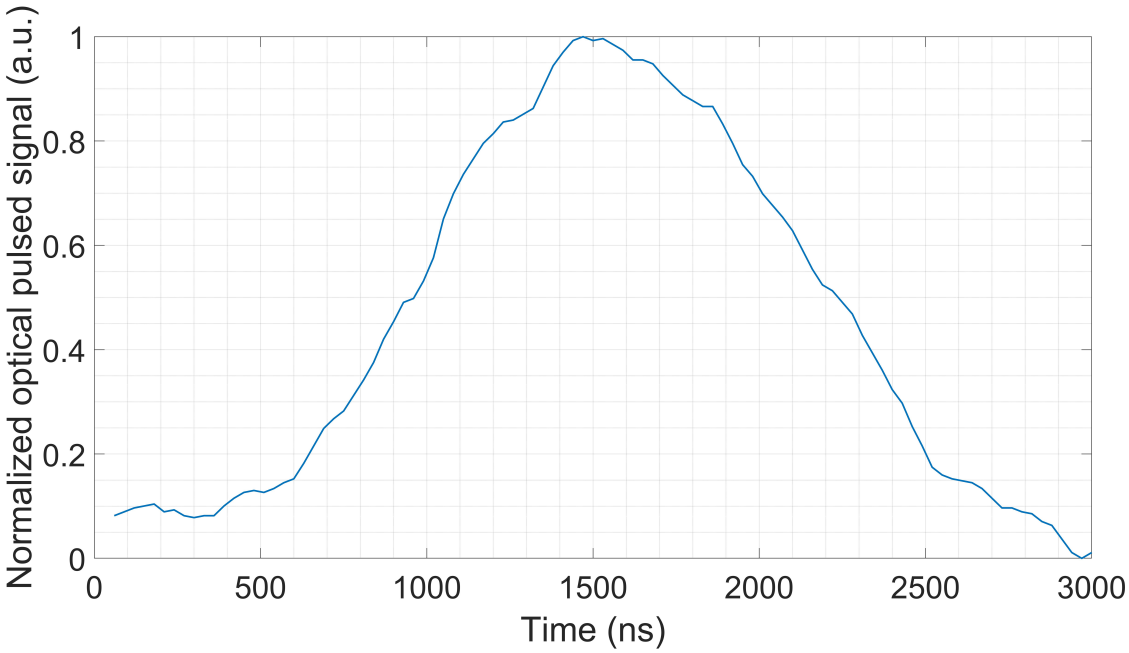

Figure C.8: 1 μs pulse ODMR signal with averaging of 10 at full power.

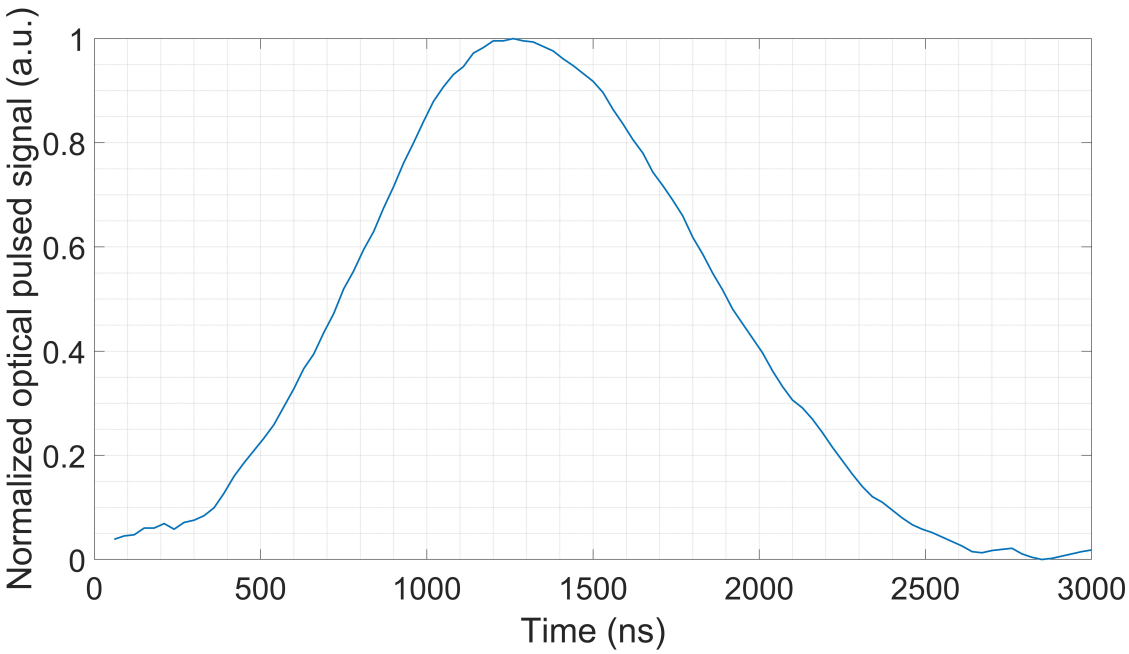

Figure C.9: 1 μs pulse ODMR signal with averaging of 100 at full power.

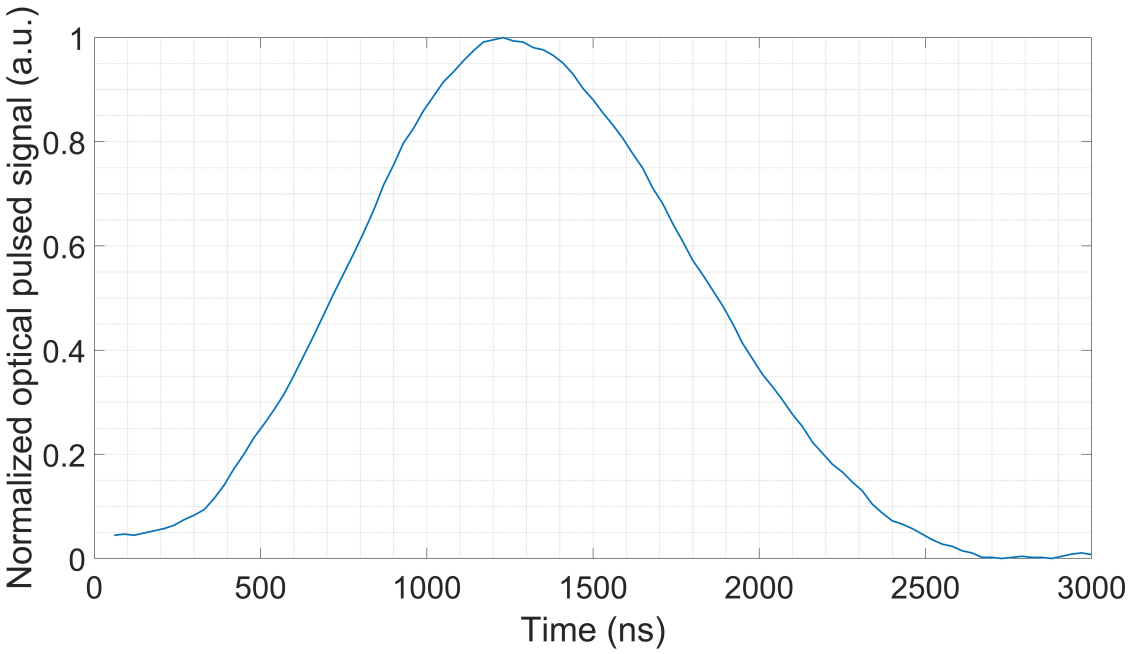

Figure C.10: 1 μs pulse ODMR signal with averaging of 400 at full power.

Appendix D

Appendix - The OSCAR-QUBE

Appendix D presents the reader with pictures of the OSCAR-QUBE. The internals, the external, and placement of the Ground and Flight model in the Space Application Services ICE CUBE Facility.

Figure D.1: OSCAR-QUBE GM and FM in the lab at IMO-IMOMEC with dimmed lighting.

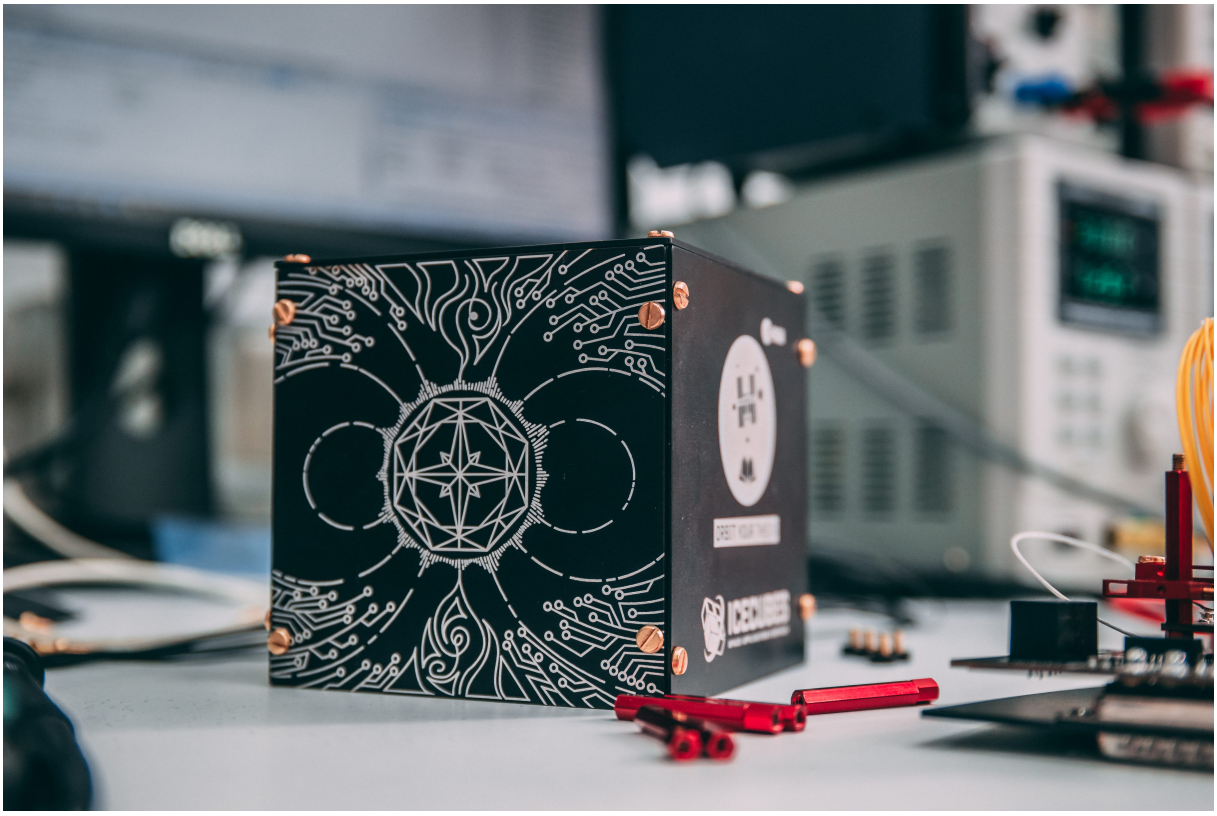

Figure D.2: OSCAR-QUBE in the lab at IMO-IMOMEC after winning design was lasered onto the side panel.

Figure D.3: OSCAR-QUBE Art design close-up.

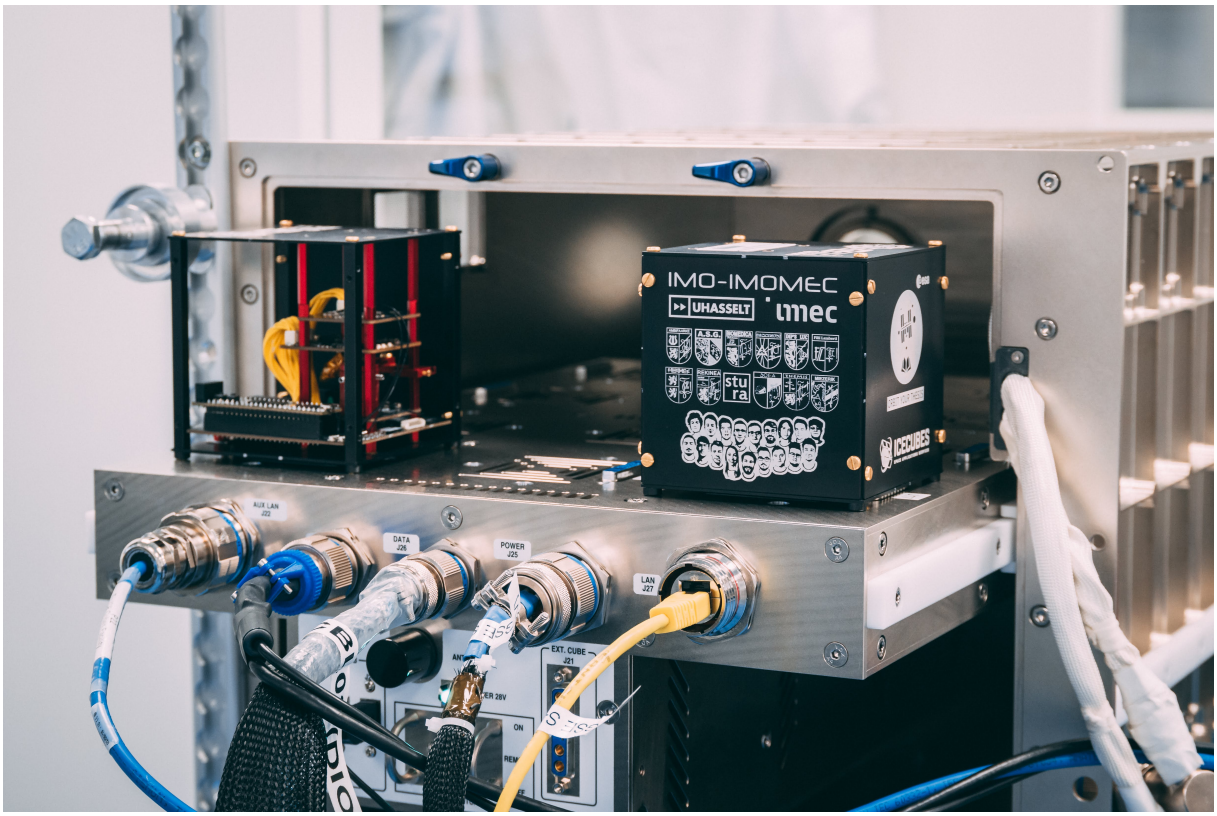

Figure D.4: OSCAR-QUBE at Space Application Services in the ICE CUBE Facility with tray opened.

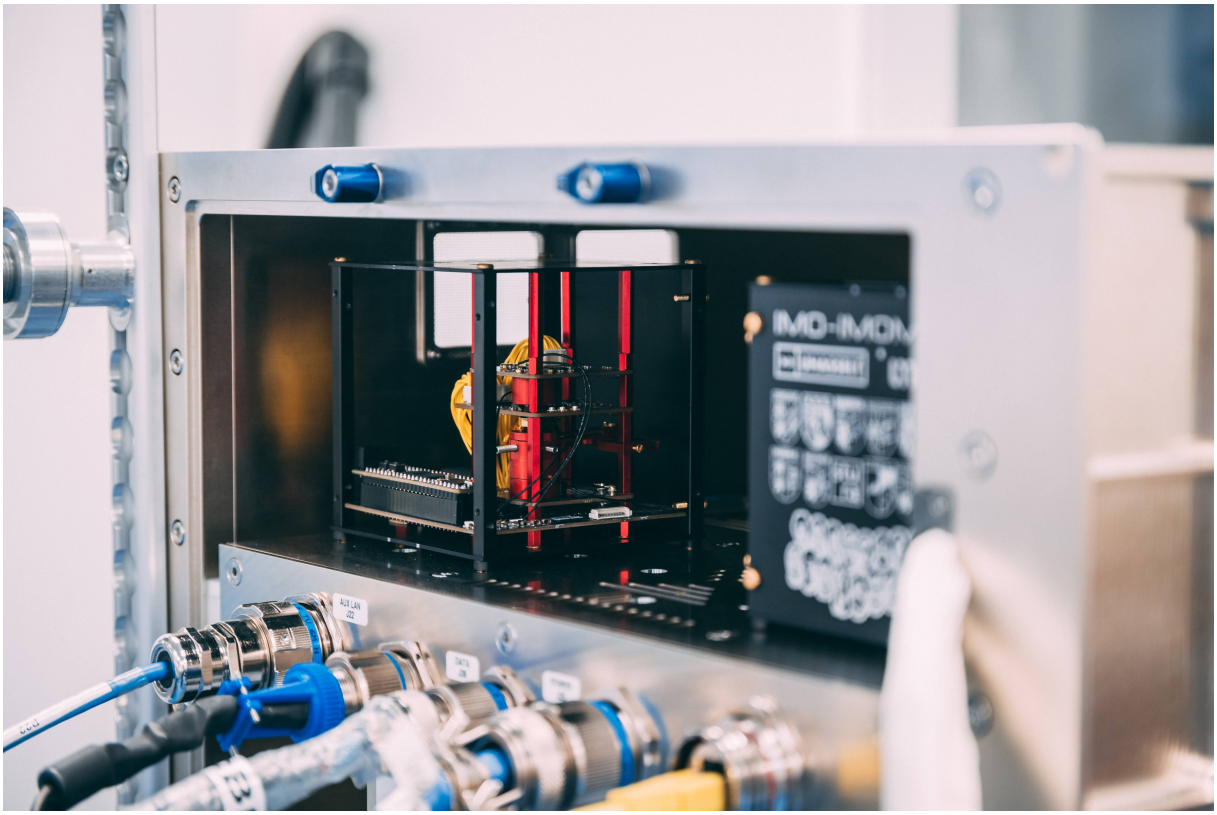

Figure D.5: OSCAR-QUBE at Space Application Services in the ICE CUBE Facility with tray closed.

Figure D.6: Close-up of the powered OSCAR-QUBE GM at Space Application Services in the ICE CUBE Facility.

Figure D.7: OSCAR-QUBE GM and FM at Space Application Services in the ICE CUBE Facility.